ADJOINT-BASED OPTIMIZATION OF SWITCHED RELUCTANCE MOTORS

ADJOINT-BASED OPTIMIZATION OF SWITCHED RELUCTANCE MOTORS

By

Ehab Sayed, B. Sc., M. Sc.

A Thesis
Submitted to the School of Graduate Studies
in Partial Fulfillment of the Requirements
for the Degree
Doctor of Philosophy

McMaster University

DOCTOR OF PHILOSOPHY (2019) MCMASTER UNIVERSITY
(Electrical and Computer Engineering) Hamilton, Ontario

TITLE: **Adjoint-based Optimization of Switched Reluctance Motors**

AUTHOR: Ehab Mohammed Mahmoud Sayed

B. Sc.
Electrical Engineering Department
(Benha University, Cairo, Egypt)

M. Sc.
Electrical Engineering Department
(Benha University, Cairo, Egypt)

SUPERVISORS: Dr. Mohamed Bakr and Dr. Ali Emadi

NUMBER OF PAGES: xxii, 128

To my Parents, Wife, and Family

Abstract

High-accuracy electromagnetic design and analysis of electric machines is enhanced by the use of various numerical methods. These methods solve Maxwell's equations to determine the distribution of the electric and magnetic fields throughout the considered machine structure. Due to the complicated architectures of the machines and the nonlinearity of the utilized magnetic materials, it is a very challenging task to obtain an analytical solution and, in most cases, only a numerical solution is possible.

The finite element method (FEM) is one of the standard numerical methods for electromagnetic field analysis. The considered machine domain is divided into finite elements to which the field equations are applied. FEM solvers are utilized to develop optimization procedures to assist in achieving a design that meets the required specifications without violating the design constraints. The design process of electric machines involves adjusting the machine parameters. This is usually done through experience, intuition, and heuristic approaches using FEM software which gives results for various parameter changes. There is no guarantee that the achieved design is the optimal one.

An alternative approach to the design of electric machines exploits robust gradient-based optimization algorithms that are guaranteed to converge to a locally-optimal model. The gradient-based approaches utilize the sensitivities of the performance characteristics with respect to the design parameters. These sensitivities are classically calculated using finite difference approximations which require repeated simulations with perturbed parameter values. The cost of evaluating these sensitivities can be significant for a slow

finite element simulation or when the number of parameters is large. The adjoint variable method (AVM) offers an alternative approach for efficiently estimating response sensitivities. Using at most one extra not-iterative simulation, the sensitivities of the response to all parameters are estimated.

Here, a MATLAB tool has been developed to automate the design process of switched reluctance motors (SRMs). The tool extracts the mesh data of an initial motor model from a commercial FEM software, JMAG. It then solves for magnetic vector potential throughout the considered SRM domain using FEM taking into consideration the nonlinearity of the magnetic material and the motor dynamic performance. The tool calculates various electromagnetic quantities such as electromagnetic torque, torque ripple, phase flux linkage, x and y components of flux density, air-region stored magnetic energy, phase voltage, and phase dynamic currents.

The tool uses a structural mapping technique to parametrize various design parameters of SRMs. These parameters are back iron thickness, teeth height, pole arc angle, and pole taper angle of both stator and rotor. Moreover, it calculates the sensitivities of various electromagnetic quantities with respect to all these geometric design parameters in addition to the number of turn per phase using the AVM method.

The tool applies interior point optimization algorithm to simultaneously optimize the motor geometry, number of turns per phase, and the drive-circuit control parameters (reference current, and turn-on and turn-off angles) to increase the motor average dynamic torque. It also applies the ON/OFF topology optimization algorithm to optimize the

geometries of the stator teeth for proper distribution of the magnetic material to reduce the RMS torque ripple.

A 6/14 SRM has been automatically designed using the developed MATLAB tool to achieve the same performance specifications as 6110E Evergreen surface-mounted PM brushless DC motor which is commercially available for an HVAC system.

Acknowledgements

First and Foremost, I would like to express my sincere thanks, gratitude, and appreciation to my supervisors Dr. Mohamed Bakr and Dr. Ali Emadi for their unlimited support, enthusiasm, motivation, guidance, and patience throughout my research work. They have always been open to talk and willing to help. It has been a great privilege to be supervised by them.

Besides my supervisors, I am also grateful to my supervisory committee members Dr. Mehdi Narimani and Dr. Jennifer Bauman for their comments and suggestions that helped me a lot in my research.

I also would like to thank Dr. Berker Bilgin for his assistance, priceless discussions, motivation, and suggestions. He has always guided me towards the right track. He provided me with many exciting and unique ideas that have made my research easier and remarkable.

In addition to my research work, I have been part of the Canada Excellence Research Chair in Hybrid Powertrain Program. I have been involved in many industry-sponsored projects where I have gained tremendous knowledge and experience. I am grateful to my colleagues in the Program. Special thanks go to Jianbin Liang, Dr. Sandra Castano, Dr. James (Weisheng) Jiang, Dr. Rong Yang, and Milan Kordic. I will always remember the stimulating discussions and the great times we have shared together.

I deeply thank my father, Mohammed Mahmoud, and my mother, Eman Mohamed Talaat, who dedicated their lifetime to help me in all my life aspects. All the love and gratitude goes to my brother, Ayman, and my sister, Esraa.

I would like to express my sincere gratitude to my wife, Sherouk Abdelaziz, for her trust, support, encouragement, and patience. Without her motivation, this achievement

would not be possible. I would also like to express my love to my lovely daughter, Jouri, for always cheering me up.

Above all, I believe that everything I have achieved so far and will achieve throughout my life is due to Allah's help and guidance.

This research was undertaken, in part, thanks to funding from the Canada Excellence Research Chairs Program, and the Natural Sciences and Engineering Research Council of Canada (NSERC). The authors also gratefully acknowledge Powersys Solutions for their support with JMAG software in this research.

Table of Contents

List of Figures

List of Tables

Nomenclature

$\boldsymbol{A}$	Magnetic vector potential vector
$A_z^{(e)}$	Magnetic vector potential of the e^{th} element
$A_{z1}^{(e)}$	Magnetic vector potential at node 1 of the e^{th} element
$A_{z2}^{(e)}$	Magnetic vector potential at node 2 of the e^{th} element
$A_{z3}^{(e)}$	Magnetic vector potential at node 3 of the e^{th} element
$A_{z,avg}^{(e)}$	Average value of the magnetic vector potential of the e^{th} element
$\hat{\boldsymbol{A}}_z$	Adjoint magnetic vector potential vector
$\overline{\boldsymbol{A}}_z$	Nominal magnetic vector potential vector
$\boldsymbol{B}$	Magnetic-flux-density vector
$\boldsymbol{B}^{(e)}$	Magnetic-flux-density vector of the e^{th} element
B	Magnitude of the magnetic-flux-density vector
C_b	Domain boundary
$\boldsymbol{C}^{(e)}$	Gradient matrix of the e^{th} element
$\boldsymbol{d}$	Vector of nodal displacements in the x and y directions
$\boldsymbol{D}^{(e)}$	Constitutive matrix of the e^{th} element
$D_{o,s}$	Stator outer diameter
$D_{i,r}$	Rotor inner diameter
E	Modulus of elasticity
f	Objective function/response
ff_c	Bare copper fill factor

$\boldsymbol{F}$	Global structural forcing vector
f_w	Weighting function
g	Poisson's ratio
$\boldsymbol{H}$	Magnetic-field-strength vector
h_s	Stator teeth height
h_r	Rotor teeth height
$\boldsymbol{I}$	Vector of state variables
$\hat{\boldsymbol{I}}$	Vector of adjoint state variables
$\overline{\boldsymbol{I}}$	Nominal state variables
i_j	Motor j^{th} phase terminal current
I_{ref}	Reference current of the drive circuit
$\boldsymbol{J}$	Electric-current-density vector
$K^{(e)}$	Local electromagnetic stiffness matrix
K	Global electromagnetic stiffness matrix
LHS	Left hand side
L_u	Motor phase inductance in the unaligned position
L_a	Motor phase inductance in the aligned position
l_j	Incremental inductance of the j^{th} phase
L	Motor axial length in the z-direction
L_g	Airgap length
$\boldsymbol{M}$	Global structural stiffness matrix
n	Domain outward normal unit vector
N_r	Number of rotor poles

N	Number of turns per phase
$N_{e,AR}$	Total number of air region elements
N_c	Number of turns per coil
N_{e,S_1}	Total number of elements in the coil winding area S_1
N_{e,S_2}	Total number of elements in the coil winding area S_2
$N_i^{(e)}$	Shape function at the i^{th} node of the e^{th} element
N_n	Total number of domain nodes
$\boldsymbol{p}$	Geometric parameters within the domain
p	Number of pole pairs
$\bar{p}_i$	Nominal value of the i^{th} design parameter
p_i	i^{th} parameter
Δp_i	i^{th} parameter perturbation
$Q^{(e)}$	Local electromagnetic forcing vector
Q	Global electromagnetic forcing vector
R	Motor resistance per phase
RHS	Right hand side
R_{Nodes}	Rotor pole shaping nodes
S_{Nodes}	Stator pole shaping nodes
$S^{(e)}$	Area of the e^{th} triangular element
T_{ripple}	Motor torque ripple
$T_{dyn,avg}$	Average value of the motor dynamic torque
T_j	Developed torque due to energizing the j^{th} phase

u_j	Motor j^{th} phase terminal voltage
$\boldsymbol{V}$	Excitation vector
v	Magnetic reluctivity
$v^{(e)}$	Reluctivity of the e^{th} element
$\overline{v}^{(e)}$	Nominal reluctivity of the e^{th} element
$W_{in,j}$	Input electrical energy of the j^{th} phase
$W_{f,j}$	Stored magnetic energy of the j^{th} phase
$W_{m,j}$	Mechanical energy of the j^{th} phase
$W_{c,j}$	Magnetic coenergy of the j^{th} phase
W_{AR}	Stored magnetic energy of the air region
x_i	x-axis coordinate of the i^{th} node of the e^{th} element
$\overline{x}$	x-axis coordinate of the triangular element centroid
y_i	y-axis coordinate of the i^{th} node of the e^{th} element
$\overline{y}$	y-axis coordinate of the triangular element centroid
y_s	Stator yoke thickness
y_r	Rotor yoke thickness
$\boldsymbol{Z}$	System matrix
ψ_j	Motor j^{th} phase flux linkage
ψ_{S_1}	Total flux linkage contributions of all elements in area S_1
ψ_{S_2}	Total flux linkage contributions of all elements in area S_2
β_s	Stator pole arc angle
β_r	Rotor pole arc angle
θ_j	Rotor position angle referred to phase j

θ_{on}	Turn-on angle of the drive circuit
θ_{off}	Turn-off angle of the drive circuit
θ_s	Stator teeth taper angle
θ_r	Rotor teeth taper angle
ω_m	Mechanical speed
Ω	Considered domain
μ	Magnetic permeability

Chapter 1

Introduction

1.1 Research Motivation

High-accuracy electromagnetic design and analysis of electric machines enhances the use of various numerical methods. These methods solve Maxwell's equations to determine the distribution of the electric and magnetic fields throughout the considered machine structure [1]. Due to the complex geometrical features of the machines and the nonlinearity of the utilized magnetic materials, it is a very challenging task to obtain an analytical solution and it will not be as accurate as a numerical solution.

The finite element method (FEM) is one of the standard numerical methods that takes into consideration the geometrical complexities, material properties, and terminal electrical conditions in electric drives [1]. The considered machine domain is divided into finite elements to which the field equations are applied. This method was proposed in the 1940s. However, it has been used to electromagnetic problems since 1968 [2]. It is currently the most popular method for solving vector field problems [1].

FEM solvers are utilized to achieve a design that meets the required specifications without violating the design constraints [3]. The design process of electric machines involves adjusting the machine parameters. This is usually done through experience, intuition, and heuristic approaches using FEM software [3]. There is no guarantee that the achieved design is the optimal one.

An alternative approach to the design of electric machines exploits robust gradient-based optimization algorithms that are guaranteed to converge to a locally-optimal model.

Gradient-based geometric or topology optimization may be applied to the machine under study to achieve an optimal design. The gradient-based approaches utilize the sensitivities of the performance characteristics with respect to the design parameters. These sensitivities are classically calculated using finite difference approximations which require repeated simulations with perturbed parameter values. The cost of evaluating these sensitivities can be significant for a slow finite element simulation or when the number of parameters is large. The adjoint variable method (AVM) offers an alternative approach for efficiently estimating response sensitivities. Using at most one extra not-iterative simulation, the sensitivities of the response to all parameters are estimated.

Permanent-split capacitor (PSC) motors utilized in household heating, ventilation, and air-conditioning (HVAC) application are currently replaced by the more-efficient brushless DC motors, also known as electronically commutated motors (ECM) [4]. This type of motors utilizes permanent magnets (PMs) in the rotor. Thus, the motor has a high power density, efficiency, and power factor. However, the market for rare-earth PMs is not stable. The prices of rare-earth materials have experienced a drastic increase in 2011 as shown in Fig. 1.1. The reason is that China, the supplier of 85% of rare-earth metals and 100% of heavy rare-earth metals [5], has threatened to ban its supply at the end of 2010 [4, 5].
As a result, extensive research is conducted to find an alternative to PM motors. Switched reluctance motors (SRMs) do not use permanent magnets or windings on the rotor. This results in a simpler and rugged construction and lower manufacturing cost. SRMs are also capable of operating at high speeds. These merits make SRM viable alternative to PM motors.

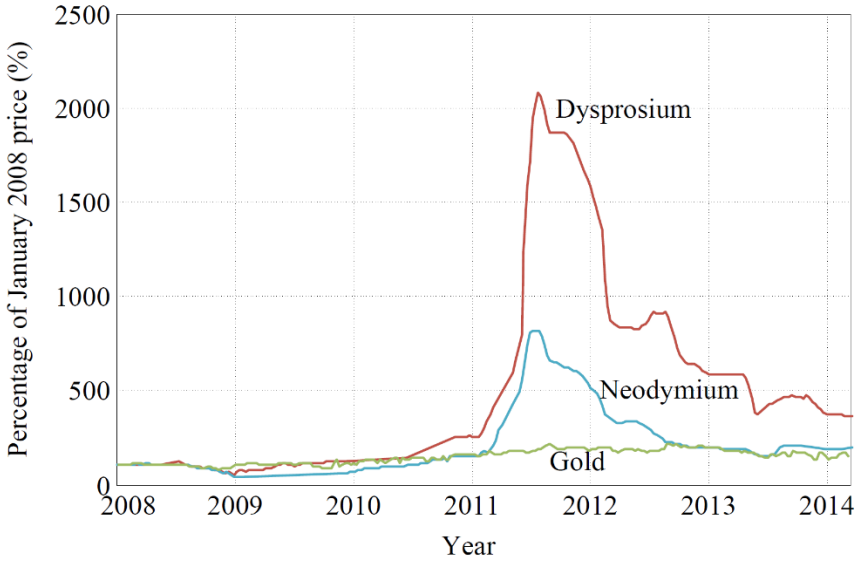

Fig. 1.1. Prices of rare-earth materials compared with gold [4, 5].

In this thesis, adjoint-based geometric and topology optimization are applied to a 6/14 SRM to achieve the same performance specifications as 6110E Evergreen surface-mounted PM brushless DC motor which is commercially available for an HVAC system [4].

1.2 Background

This section includes a literature review about switched reluctance motors, geometry, control, and topology optimization of electric motors, and the adjoint variable method.

1.2.1 Switched Reluctance Motors

The increasing prices and limited supply of permanent magnets motivated researchers to focus on the use of switched reluctance motors in many applications such as HVAC applications [6]. A 3D model of a 6/14 switched reluctance motor is shown in Fig. 1.2. The first and second numbers refer to the number of stator and rotor poles, respectively. Since there are no permanent magnets or windings used on the rotor, SRM has simple and rugged structure, high operating temperature and low manufacturing cost [7]. SRM, on the

contrary, has high torque ripple and high acoustic noise and vibrations [8].

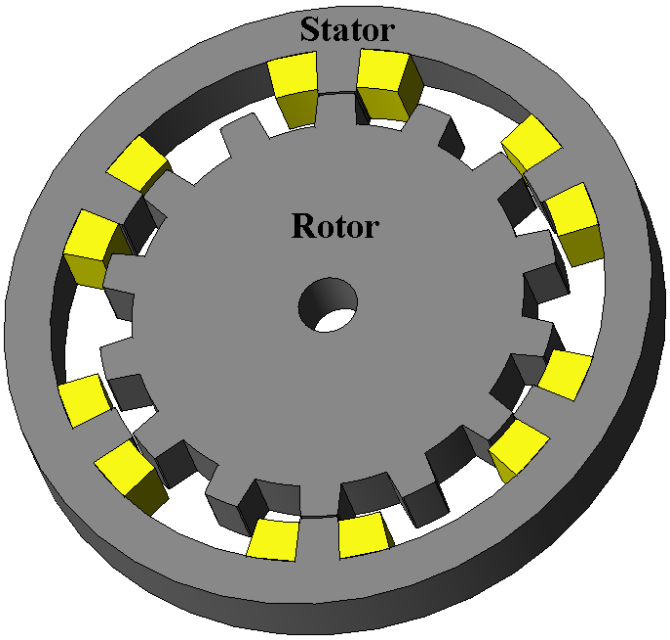

Fig. 1.2. A 3D model of a switched reluctance motor.

The first application of SRM was more than 150 years ago to drive a locomotive [9]. In 1969, a variable reluctance motor was proposed for variable speed drives [9].

SRM commonly uses a larger number of poles on stator than rotor [7]. A comparative study of three topologies of SRMs for electric vehicle propulsion with a different number of phases and various combinations of stator and rotor poles was carried out in [10]. The effect of changing the number of phases and slot/pole combination of segmented SRM on performance characteristics (efficiency, operating speed range and overload capability) was studied in [11].

In [12] various methods of designing SRMs were presented. Linear, nonlinear, and finite element methods were introduced. In [13] a comparison between tapered and straight designs of stator poles of SRMs was presented. It was found that the tapered motor is

superior in terms of the average and peak torques, and the torque ripple is almost the same for both designs. A switched reluctance motor which has an inner pancake stator with axial winding was proposed in [14]. This design provides a high slot-fill factor and can be implemented as a flat pancake-shaped stator. In [15] a detailed design of a double-rotor switched reluctance motor was presented. A double-rotor SRM was proposed for integrated hybrid transmission of a hybrid electric vehicle in [16]. An outer-rotor in-wheel SRM was proposed for electrical bus application in [17]. The proposed motor was shown to be superior in terms of the torque ripple and efficiency. In [18] a comparison between a proposed cylindrical outer shape rotor and conventional rotor of SRMs was presented. The proposed rotor was found to have significantly lower windage loss and acoustic noise. The design of segmented outer-rotor SRM for a direct-drive application was investigated in [19]. In [20] an improved planar switched reluctance motor (PSRM) with minimized force ripple was proposed. A hybrid motion SRM which can operate in rotary, linear, and rotary-linear modes with independent control for both rotary and linear motions was presented in [21]. The suitability of SRMs for electric and hybrid vehicles was investigated in [22] where the static and dynamic performance of several 8/6 and 6/4 SRM geometries were studied with different geometric changes.

The dynamic performance of a three-phase 6/10 switched reluctance motor used in traction application was investigated in [23]. A phase-shift design methodology of SRM for boosting the motor starting torque and ensuring its startup capability was proposed in [24]. A comparison between SRM drive and an inverter-fed induction motor drive for a particular traction application was presented in [25]. In [26] many performance

specifications of SRM drives such as torque per unit volume, efficiency, converter volt-ampere rating, etc. were compared with those of typical induction motor drives. A comparison between SRM, induction motor, and PM synchronous motor (PMSM) was presented in [27]. The comparison showed that SRM is competitive with the other two motor types in terms of torque/weight and power/weight ratios. In [28] a switched reluctance motor was proposed which competes the interior PMSM employed in the 2009 Toyota Prius in terms of torque, power, speed-range, and efficiency. Torque sharing function (TSF) was used in [29] to control the SRM torque at extended speed and low torque ripple.

1.2.2 Geometry, Control, and Topology Optimization of Electric Motors

Geometry optimization of SRM was applied in [30] to increase the motor power density and efficiency and reduce the acoustic noise. Two multi-objective optimization methods, Parametric Solution Selection (PSS) and Augmented Lagrangian Genetic Algorithm (ALGA), were utilized in [31] to design an 8/14 SRM with minimized torque ripple and maximized average torque. Taguchi method was used in [32] to optimize the turn-on and turn-off angles of an SRM drive circuit in addition to the motor geometry to reduce the torque ripple and increase the efficiency. In [33] a two-phase 4/2 SRM rotor was optimized using the level set method (LSM) to improve its static torque characteristics. Multi-objective design optimization of SRMs utilizing a combination of design of experiments (DOE) and particle swarm optimization (PSO) methods was investigated in [34]. A simple search technique was proposed in [35] to optimize the turn-on and turn-off angles of an

SRM drive to increase the motor efficiency and torque per ampere ratio simultaneously and reduce the torque ripple and energy consumption.

The pole shape of a brushless DC motor was optimized to reduce the cogging torque in [36]. In [37], a level set method was used to optimize the rotor shape of a synchronous reluctance motor to maximize the average torque and minimize the cogging torque. The steepest descent algorithm was utilized in [38] to optimize the rotor pole shape of spoke-type interior permanent magnet IPM motor to reduce the cogging torque and the partial magnet demagnetization. Single-phase and multi-phase level set methods were used in [39] to maximize the Lorentz force on the moving coil of a voice coil motor. A gradient ascent method was utilized in [40] to optimize the stator and rotor poles of a switched reluctance motor to maximize the average torque and minimize the torque ripple. Topology optimization of the rotors of surface permanent magnet (SPM), IPM, and synchronous reluctance motors was conducted to maximize the total torque for a specific motors cost [41]. A level set method was utilized in [42] to optimize the stator and rotor shapes of synchronous reluctance motors to maximize the torque.

The stator tooth face shape and the rotor tooth shoe of a 6/4 SRM were optimized to minimize the torque ripple in [43]. In [44], the steepest descent method was utilized to optimize the stator tooth shape of an 8/6 SRM to reduce the torque ripple and increase the average torque. The rotor tooth shape of a 4/2 SRM was optimized in [45] to reduce the torque ripple and increase the average and starting torques. The electromagnetic performance of a 16/20 in-wheel outer-rotor SRM was improved in [46] by optimizing the motor geometry.

Topology optimization based on the level set method was used to optimize the distribution of the magnetic material in the rotor teeth of an 8/6 SRM to reduce the torque ripple in [47]. The stator and rotor geometries of a 6/4 SRM were optimized using topology optimization with optimizing the electric-circuit turn-on and turn-off angles to reduce the torque ripple and the rotor mass in [48].

1.2.3 Adjoint Variable Method

The gradient-based optimization approaches utilize the sensitivities of motor performance characteristics versus design parameters. These sensitivities are classically calculated using finite difference approximations. These approximations carry out repeated simulations with perturbed parameter values [49-52]. The cost of evaluating these sensitivities can be significant for a slow finite element simulation or when the number of parameters is large [49-51].

The adjoint variable method (AVM) offers an alternative approach for efficiently estimating response sensitivities. Using at most one extra simulation, the sensitivities of the response to all parameters are estimated [49-51]. AVM may be classified into two different approaches; the first approach is the discrete approach in which desired sensitivities are obtained using derivatives of a discretized system of equations. This approach was utilized in the optimization process of voice coil motor [39], levitated rod and a cantilever electromagnet [53]. It was also used in the sensitivity analysis of anisotropic structures [54], to obtain wideband second-order sensitivities of electromagnetic structures [55], and transient sensitivity analysis of metallic waveguides [56]. The second approach is the continuum approach where closed-form design sensitivity

expression is obtained by applying a variational approach to equations governing the electromagnetic system. This approach was utilized in the optimization process of synchronous reluctance motors [37, 57], brushless DC motors [36, 58], IPM motors [59, 60], and synchronous generators [61]. The AVM approach has been applied in different fields. In addition to the low frequency structures [36, 37, 39-42], [53], [57-60] and high frequency structures [50], [51], [54-56], [62], it is also utilized in the field of structural analysis [63-66].

1.3 Research Novelty and Contributions

A MATLAB tool has been developed to automate the design process of switched reluctance motors (SRMs). The tool extracts the mesh data of an initial motor model from a commercial FEM software, JMAG. It then solves for magnetic vector potential throughout the considered SRM domain using finite element method (FEM) taking into consideration the nonlinearity of the magnetic material and the motor dynamic performance. The tool calculates various electromagnetic quantities such as electromagnetic torque, torque ripple, phase flux linkage, x and y components of flux density, air-region stored magnetic energy, phase voltage, and phase dynamic currents.

The tool uses a structural mapping technique to parametrize various design parameters of SRMs. These parameters are back iron thickness, teeth height, pole arc angle, and pole taper angle of both stator and rotor. Moreover, it calculates the sensitivities of various electromagnetic quantities with respect to all these geometric design parameters in addition to the number of turn per phase using the AVM method.

The tool applies an interior point optimization algorithm to optimize the motor geometry, number of turns per phase, and the drive-circuit control parameters (reference current, and turn-on and turn-off angles) to increase the motor average dynamic torque. It also applies an ON/OFF topology optimization algorithm to optimize the geometries of the stator teeth for proper distribution of the magnetic material to reduce the RMS torque ripple.

A 6/14 SRM for an HVAC application has been automatically designed using the developed MATLAB tool.

1.4 Thesis Outline

The thesis includes finite element analysis of switched reluctance motors when utilizing either linear or nonlinear magnetic materials. The adjoint variable method is used for the sensitivity analysis of SRMs in both linear and nonlinear cases. In the thesis, geometry, control, and topology optimization approaches are applied to a 6/14 SRM to achieve the performance specifications of a commercially available surface-mounted PM brushless DC motor of an HVAC system.

Chapter 2 presents the construction, working principle, and modeling of SRMs. The fundamentals of magnetostatic finite element analysis in case of utilizing either linear or nonlinear magnetic materials are also investigated. Various electromagnetic responses of SRMs are then calculated using the finite element method.

Chapter 3 introduces the sensitivity analysis using the adjoint variable method in case of linear and nonlinear systems of equations.

Chapter 4 studies the sensitivities of various electromagnetic responses of SRMs with respect to different geometric design parameters when utilizing either linear or nonlinear magnetic materials. The sensitivities obtained using the adjoint variable method are compared with those obtained using the more-accurate but time-intensive Central Finite Differences (CFD).

Chapter 5 investigates geometric optimization of the considered 6/14 SRM to maximize the motor static torque profile using the interior-point algorithm. Structural mapping technique is utilized to control the geometry of the considered motor. Moreover, the motor geometry and the drive-circuit control parameters are simultaneously optimized to maximize the motor steady-state dynamic torque.

Chapter 6 studies the topology optimization of the considered SRM to achieve a particular average value of the dynamic torque while minimizing the RMS torque ripple. The ON/OFF topology optimization technique is used for that purpose.

Chapter 7 summarizes the main findings of the thesis and the recommendations for future work.

This page is intentionally left blank

Chapter 2

Fundamentals and Finite Element Analysis of Switched Reluctance Motors (SRMs)

2.1 Introduction

Switched reluctance motors (SRMs) do not use permanent magnets or windings on the rotor. This results in a simpler and rugged construction and reduces manufacturing cost [67, 68]. SRMs are also capable of operating at high speeds [69]. These merits, in addition to supply shortage and increasing prices of permanent magnets, motivate researchers to focus on replacing permanent magnet (PM) motors with the lower-cost SRMs [69]. High torque ripple and acoustic noise are the main disadvantages of SRMs [70]. Preliminary research is conducted on how to reduce the torque ripple and the audible noise [70, 71].

Due to the motor complex magnetic geometry and nonlinearity of magnetic materials, the Finite Element Method (FEM) is more suitable to obtain the field distribution throughout the motor domain [1, 72]. FEM calculates the magnetic vector potential values in the whole domain [1, 72]. These values are then post-processed to compute different electromagnetic quantities [1]. Fundamentals of the finite element method and its application to SRMs will be discussed later in the chapter.

2.2 Fundamentals of Switched Reluctance Motors

A switched reluctance motor has double salient structure. It is comprised of a stator and a rotor which have salient poles. The motor configuration is determined by the number of phases and the number of stator and rotor poles. A schematic diagram of a three-phase 6/4

SRM configuration is shown in Fig. 2.1. This motor configuration has six stator poles and four rotor poles. The SRM has simple and rugged construction since there are no permanent magnets or windings mounted on the rotor. This feature enables the motor to work at high speeds and high temperatures [73, 74]. Concentrated, also known as short-pitched, coils are wound around the stator teeth. Due to the doubly-salient structure, the rotor position affects the magnetic reluctance of the flux path. When a stator coil is energized, the rotor pole tends to align itself with the stator pole to reduce the magnetic reluctance of that flux path [74]. The fundamentals, principle of operation, and modeling of SRMs will be investigated in the following subsections.

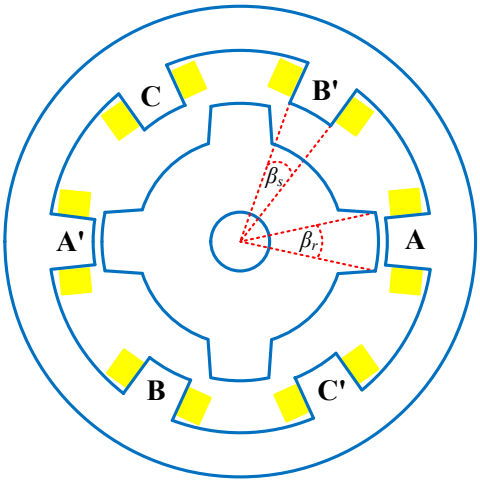

Fig. 2.1. A schematic diagram of a three-phase 6/4 SRM.

2.2.1 Operation of Switched Reluctance Motors

The inductance profile of a switched reluctance motor represents the effect of the rotor position on the phase inductance. The profile affects the motor developed torque. The main locations of the rotor pole with respect to the stator pole are presented as shown in Fig. 2.2. The presented positions and the corresponding angles depend on the stator pole arc angle

β_s and the rotor pole arc angle β_r, shown in Fig. 2.1, in addition to the number of rotor poles N_r. These angles are obtained using the following equations [75]

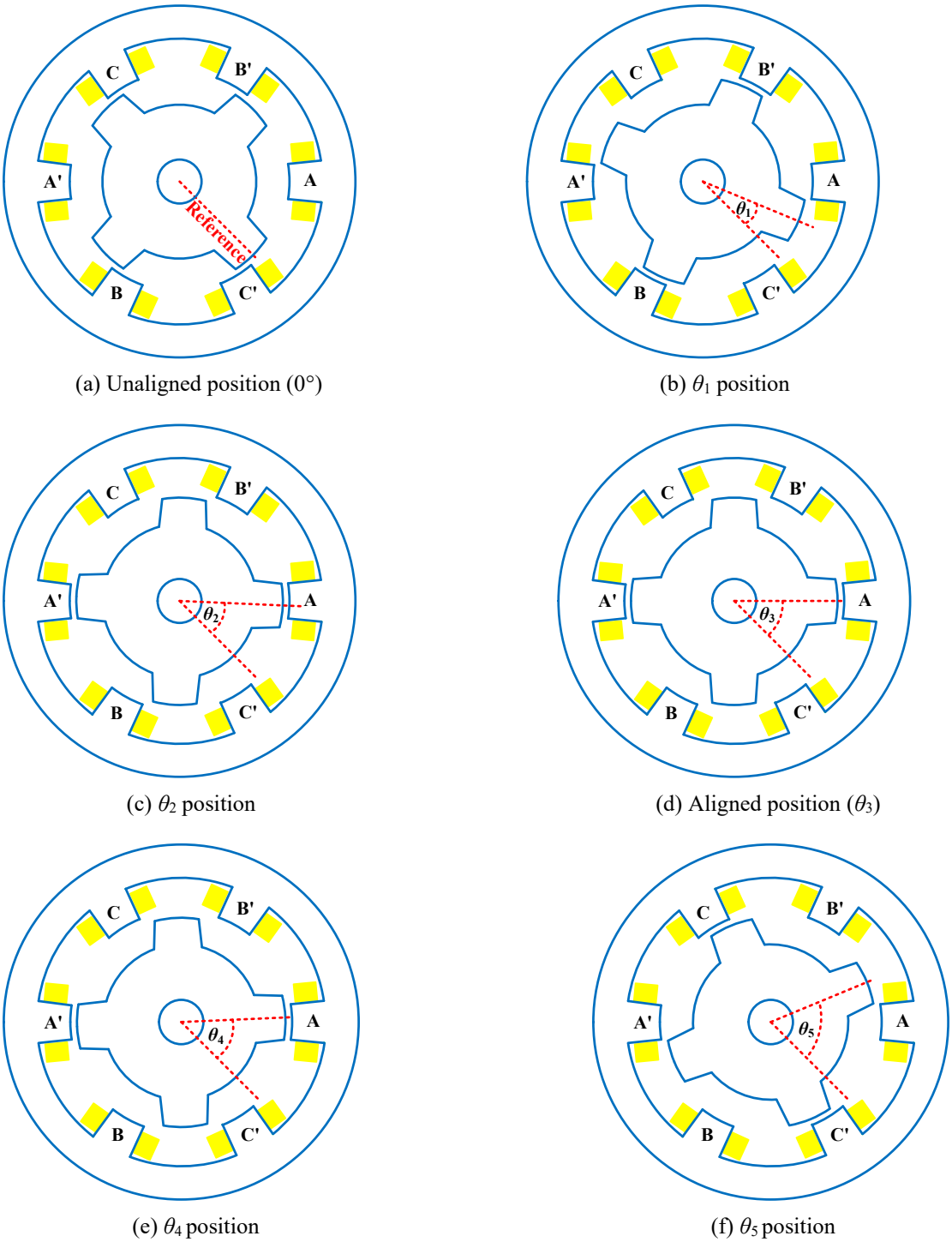

(a) Unaligned position (0°)

(b) θ_1 position

(c) θ_2 position

(d) Aligned position (θ_3)

(e) θ_4 position

(f) θ_5 position

Fig. 2.2. Different rotor positions of a three-phase 6/4 SRM.

$$\theta_1 = \frac{1}{2}\left[\frac{360^{\circ}}{N_r} - \left(\beta_s + \beta_r\right)\right] \tag{2.1}$$

$$\theta_2 = \theta_1 + \beta_s \tag{2.2}$$

$$\theta_3 = \theta_2 + \frac{\beta_r - \beta_s}{2} \tag{2.3}$$

$$\theta_4 = \theta_2 + \beta_r - \beta_s \tag{2.4}$$

$$\theta_5 = \theta_4 + \beta_s \tag{2.5}$$

The ideal inductance profile of SRMs is shown in Fig. 2.3 when the rotor rotates in a counter-clockwise direction [75, 76]. The inductance profile is further investigated as follows [75, 76].

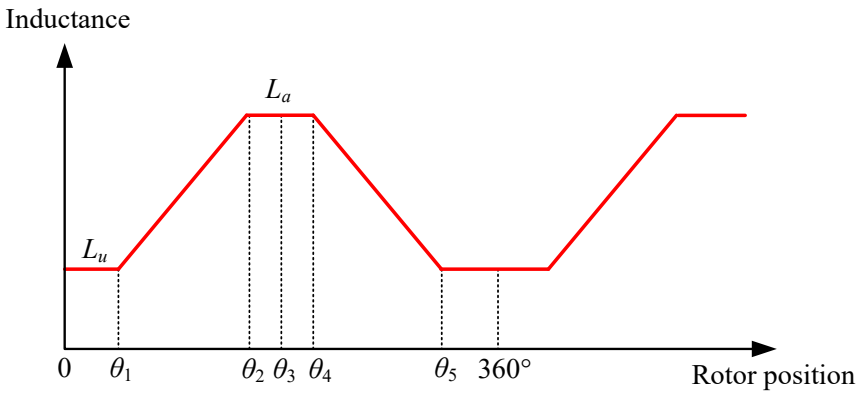

Fig. 2.3. Ideal inductance profile of SRMs.

- Position 0° is the reference position or the unaligned position of the motor. The magnetic reluctance of the flux path is maximum and the corresponding inductance, known as unaligned inductance L_u, is minimum.
- Position 0° – θ_1: There is no overlapping between the rotor and stator poles, so the inductance is constant at its minimum value. There is no developed torque at this region.

- Position $\theta_1 - \theta_2$: The overlapping between stator and rotor poles starts and increases as the rotor moves. Hence, the magnetic reluctance decreases, and the inductance increases. Due to the positive change of inductance with respect to the rotor position, a current applied in this region produces positive torque (motoring mode).
- Position $\theta_2 - \theta_4$: There is complete overlapping between stator and rotor poles starting from the position θ_2 hence the inductance, known as aligned inductance L_a, is maximum. The complete overlapping continues from θ_2 to θ_4. The inductance is constant at this region, so there is no developed torque at this region.
- Position $\theta_4 - \theta_5$: The overlapping between stator and rotor poles decreases as the rotor moves. Hence, the magnetic reluctance increases, and the corresponding inductance decreases. Due to the negative change of inductance with respect to the rotor position, a current applied in this region produces negative torque (generating mode).
- Position $\theta_5 - 360°$: This region is the same as the region from position 0° to θ_1. There is no overlapping between the rotor and stator poles, so the inductance is constant at its minimum value. There is no developed torque at this region.

The phases are energized in the corresponding positive-torque inductance region in sequence to maintain a continuous operating torque. This is shown in Fig. 2.4. The sequence is ACB for counter-clockwise rotation and ABC for clockwise rotation.

2.2.2 Modeling of Switched Reluctance Motors

The voltage equation per phase for a switched reluctance motor neglecting mutual coupling between phases is [77-79]

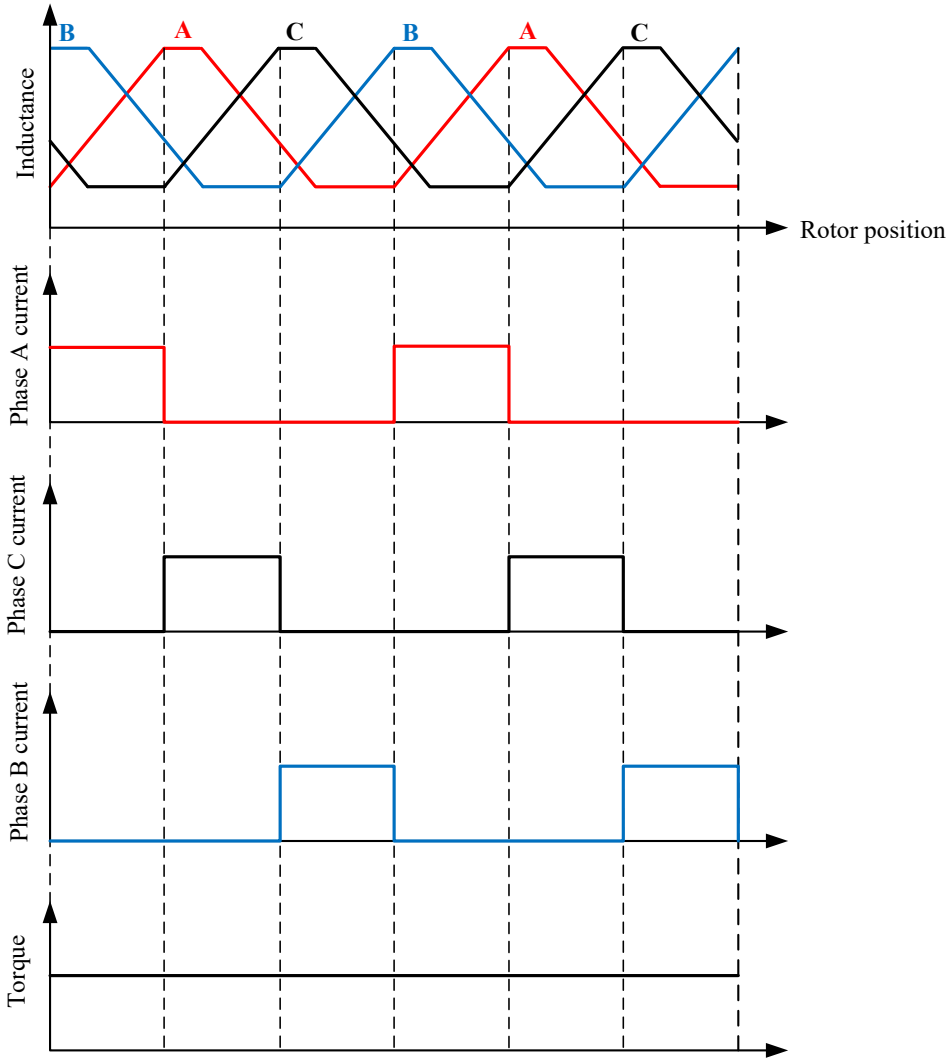

Fig. 2.4. Ideal inductance, current, and torque profiles of a 6/4 SRM.

$$u_j\left(i_j,\theta_j\right)=Ri_j\left(\theta_j\right)+\frac{d\psi_j\left(i_j,\theta_j\right)}{dt},\ \ j=1,\ 2,\ 3, \tag{2.6}$$

where u_j and i_j are the j^{th} phase terminal voltage and current, respectively. ψ_j is the j^{th} phase flux linkage, and R is the resistance per phase. θ_j is the rotor position angle referred to phase j.

The phase voltage can be rewritten as follows [78]

$$u_j\left(i_j,\theta_j\right)=Ri_j\left(\theta_j\right)+\left[\frac{\partial\psi_j\left(i_j,\theta_j\right)}{\partial i_j}\right]_{\theta_j=\text{constant}}\frac{di_j}{dt}+\left[\frac{\partial\psi_j\left(i_j,\theta_j\right)}{\partial\theta_j}\right]_{i_j=\text{constant}}\omega_m, \quad (2.7)$$

where ω_m is the mechanical speed which equals $d\theta_j/dt$. Eqn. (2.7) is rewritten in terms of the j^{th} phase incremental inductance l_j and back EMF E_j as follows [78]

$$u_j\left(i_j,\theta_j\right)=Ri_j\left(\theta_j\right)+l_j\frac{di_j}{dt}+E_j. \quad (2.8)$$

This leads to the per-phase equivalent circuit of SRMs which is shown in Fig. 2.5.

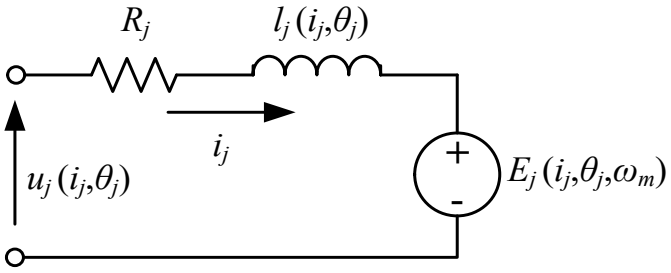

Fig. 2.5. Per-phase equivalent circuit of SRMs.

Neglecting the copper losses, the change in the input electrical energy of the j^{th} phase $W_{in,j}$ equals the sum of the changes in the stored magnetic energy $W_{f,j}$ and the mechanical energy $W_{m,j}$ [76, 78]

$$dW_{in,j}=dW_{f,j}+dW_{m,j} \quad (2.9)$$

However, from eqn. (2.7), the change in the input electrical energy equals

$$dW_{in,j}=i_ju_jdt=i_j\left[\frac{\partial\psi_j\left(i_j,\theta_j\right)}{\partial i_j}\right]_{\theta_j=\text{constant}}di_j+i_j\left[\frac{\partial\psi_j\left(i_j,\theta_j\right)}{\partial\theta_j}\right]_{i_j=\text{constant}}d\theta_j. \quad (2.10)$$

The change in the stored magnetic energy is obtained from the following equation [78]

$$dW_{f,j}\left(i_j,\theta_j\right)=\left[\frac{\partial W_{f,j}\left(i_j,\theta_j\right)}{\partial i_j}\right]_{\theta_j=\text{constant}}di_j+\left[\frac{\partial W_{f,j}\left(i_j,\theta_j\right)}{\partial\theta_j}\right]_{i_j=\text{constant}}d\theta_j, \quad (2.11)$$

and the change in the mechanical energy is obtained from

$$dW_{m,j} = T_j d\theta_j, \tag{2.12}$$

where T_j is the developed torque due to energizing the j^{th} phase.

Substituting from (2.10) to (2.12) into eqn. (2.9) results in

$$\begin{aligned} i_j \left[\frac{\partial \psi_j \left(i_j, \theta_j \right)}{\partial i_j} \right]_{\theta_j = \text{constant}} di_j + i_j \left[\frac{\partial \psi_j \left(i_j, \theta_j \right)}{\partial \theta_j} \right]_{i_j = \text{constant}} d\theta_j = \\ \left[\frac{\partial W_{f,j} \left(i_j, \theta_j \right)}{\partial i_j} \right]_{\theta_j = \text{constant}} di_j + \left[\frac{\partial W_{f,j} \left(i_j, \theta_j \right)}{\partial \theta_j} \right]_{i_j = \text{constant}} d\theta_j + T_j d\theta_j. \end{aligned} \tag{2.13}$$

By separating the $d\theta_j$ coefficents and the di_j coefficents on both sides of eqn. (2.13), it can be thus deduced that

$$W_{f,j} = \left[\int_0^{\psi_j} i_j \left(\psi_j, \theta_j \right) d\psi_j \right]_{\theta_j = \text{constant}}, \tag{2.14}$$

$$T_j = \left[\frac{\partial}{\partial \theta_j} \left(i_j \psi_j \left(i_j, \theta_j \right) - W_{f,j} \left(i_j, \theta_j \right) \right) \right]_{i_j = \text{constant}}. \tag{2.15}$$

The term $i_j \psi_j \left(i_j, \theta_j \right) - W_{f,j} \left(i_j, \theta_j \right)$ is known as the magnetic coenergy $W_{c,j}$ which can also be obtained from [77, 78]

$$W_{c,j} = \left[\int_0^{i_j} \psi_j \left(i_j, \theta_j \right) di_j \right]_{\theta_j = \text{constant}}. \tag{2.16}$$

Substituting eqn. (2.16) into eqn. (2.15), the electromagnetic torque due to energizing the j^{th} phase is obtained from

$$T_j = \left[\frac{\partial W_{c,j}}{\partial \theta_j} \right]_{i_j=\text{constant}} . \tag{2.17}$$

The phase flux linkage versus current characteristic is shown in Fig. 2.6 where the difference between the magnetic energy and coenergy is illustrated.

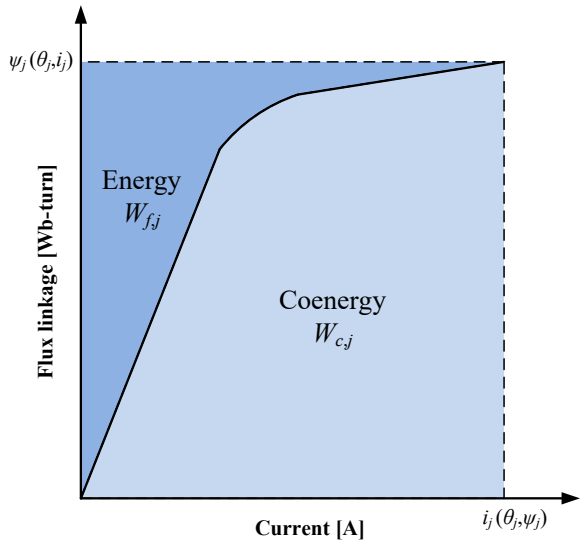

Fig. 2.6. Flux linkage versus current characteristic.

SRMs are nonlinear machines [78]. A voltage-fed model of switched reluctance motor is presented here since voltage source converters are commonly used to control the motor voltage [78].

The total torque is obtained by summing up the phases' torques [77, 78]

$$T = \sum_{j=1}^{3} T_j . \tag{2.18}$$

The voltage-fed model of SRM is shown in Fig. 2.7. The model depends on static torque in addition to flux linkage, also known as magnetization characteristics. Both characteristics are obtained at different rotor positions and different excitation currents using the finite element method. In this model, static torque data are used directly while

magnetization data are inverted such that flux linkage and rotor position angle are inputs and motor current is output.

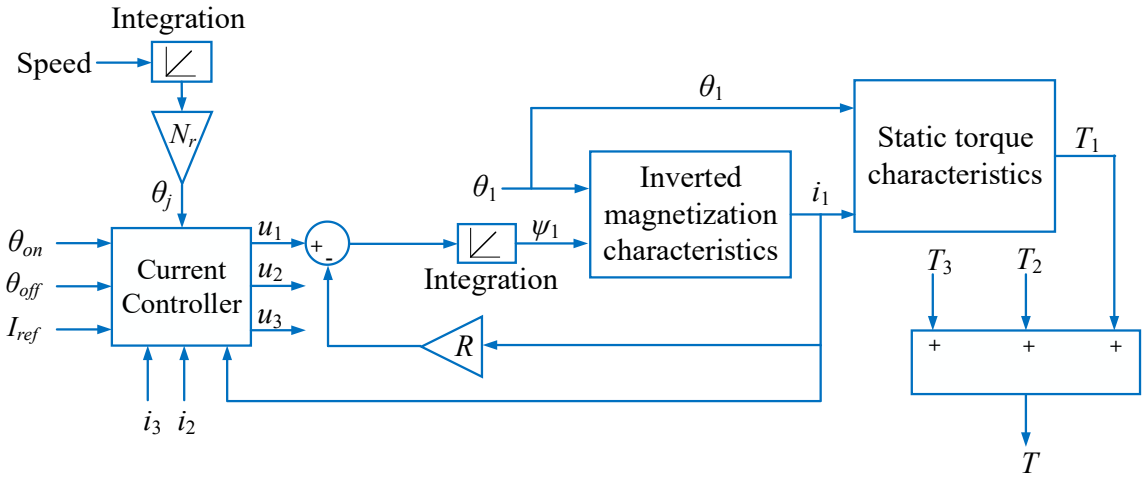

Fig. 2.7. Voltage-fed model of SRM using inverse magnetization characteristics.

The model is built to obtain the dynamic currents and torque of three-phase SRMs for different speeds at different turn-on angle θ_{on}, turn-off angle θ_{off}, and reference current I_{ref}. SRM dynamic currents at a certain speed, θ_{on}, θ_{off}, and I_{ref} are shown in Fig. 2.8.

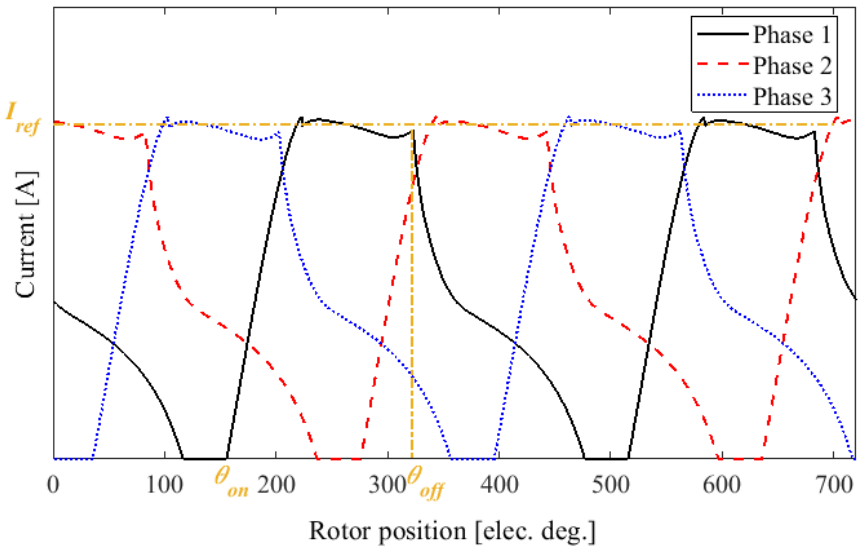

Fig. 2.8. SRM dynamic currents.

2.3 Fundamentals of Finite Element Analysis

The main approaches utilized to derive finite element equations are the variational and Galerkin approaches [72]. Many analysis cases of electric machines do not have variational expressions but can be solved using the Galerkin approach. Thus, the Galerkin approach became more common [72] and will be utilized in this analysis. Magnetostatic field analysis using this approach in case of both linear and nonlinear cases is investigated. A detailed derivation is covered here since the formulations are implemented in the MATLAB tool. This also facilitates the link between the finite element equations of the electromagnetic quantities and the corresponding sensitivities obtained in Chapter 4.

2.3.1 Magnetostatic Field Analysis (Linear Case)

For a linear magnetostatic field problem, the field can be represented using the following equations [1]

$$\nabla \cdot \boldsymbol{B} = 0, \tag{2.19}$$

$$\nabla \times \boldsymbol{H} = \boldsymbol{J}, \tag{2.20}$$

$$\boldsymbol{B} = \mu \boldsymbol{H}, \tag{2.21}$$

$$\boldsymbol{B} = \nabla \times \boldsymbol{A}, \tag{2.22}$$

where $\boldsymbol{B}$, $\boldsymbol{H}$, $\boldsymbol{J}$, $\boldsymbol{A}$ and μ are the magnetic-flux-density vector, the magnetic-field-strength vector, the electric-current-density vector, the magnetic vector potential, and the magnetic permeability, respectively.

Utilizing eqns. (2.20), (2.21), and (2.22), the field problem, eqn. (2.20), can be rewritten as [1]

$$\nabla \times \boldsymbol{H} = \nabla \times \frac{\boldsymbol{B}}{\mu} = \nabla \times \left(\frac{1}{\mu} \nabla \times \boldsymbol{A} \right) = \boldsymbol{J}. \tag{2.23}$$

In 2-D field problems with Cartesian coordinates, both $\boldsymbol{J}$ and consequently $\boldsymbol{A}$ have only a z component, so eqn. (2.23) becomes Poisson's equation [1]

$$\frac{1}{\mu} \frac{\partial^2 A_z^*}{\partial x^2} + \frac{1}{\mu} \frac{\partial^2 A_z^*}{\partial y^2} = -J_z, \tag{2.24}$$

where A_z^* is the exact solution.

The partial differential equation (2.24) relates the magnetic vector potential at every point in the domain to the electric current density at that point.

For an approximate solution A_z, the residual R becomes [72]

$$R = \frac{1}{\mu} \frac{\partial^2 A_z}{\partial x^2} + \frac{1}{\mu} \frac{\partial^2 A_z}{\partial y^2} + J_z. \tag{2.25}$$

The integral of the residual times the weighting function $\boldsymbol{f}_w$ over the considered domain Ω equals zero [72]:

$$\iint_{\Omega} \boldsymbol{f}_w R \; dxdy = \boldsymbol{0}. \tag{2.26}$$

Substituting eqn. (2.25) into eqn. (2.26)

$$\iint_{\Omega} \boldsymbol{f}_w \left(\frac{1}{\mu} \frac{\partial^2 A_z}{\partial x^2} + \frac{1}{\mu} \frac{\partial^2 A_z}{\partial y^2} + J_z \right) dxdy = \boldsymbol{0}. \tag{2.27}$$

Thus

$$\iint_{\Omega} \boldsymbol{f}_w \left(\frac{1}{\mu} \frac{\partial^2 A_z}{\partial x^2} + \frac{1}{\mu} \frac{\partial^2 A_z}{\partial y^2} \right) dxdy = -\iint_{\Omega} \boldsymbol{f}_w J_z \; dxdy. \tag{2.28}$$

Integrating LHS of eqn. (2.28) by parts leads to [72]:

$$\iint_{\Omega} \frac{1}{\mu} \left(\frac{\partial \boldsymbol{f}_w}{\partial x} \frac{\partial A_z}{\partial x} + \frac{\partial \boldsymbol{f}_w}{\partial y} \frac{\partial A_z}{\partial y} \right) dxdy - \frac{1}{\mu} \int_{C_b} \boldsymbol{f}_w \frac{\partial A_z}{\partial n} dC_b = \iint_{\Omega} \boldsymbol{f}_w J_z \; dxdy, \tag{2.29}$$

where C_b is the domain boundary and n is the normal unit vector.

The integral throughout the domain can be replaced by a summation of integrals over individual finite triangular elements [72]:

$$\sum_{M}\iint_{\Omega^{(e)}}\frac{1}{\mu^{(e)}}\left(\frac{\partial \boldsymbol{f}_w^{(e)}}{\partial x}\frac{\partial A_z^{(e)}}{\partial x}+\frac{\partial \boldsymbol{f}_w^{(e)}}{\partial y}\frac{\partial A_z^{(e)}}{\partial y}\right)dxdy-\frac{1}{\mu^{(e)}}\frac{\partial A_z^{(e)}}{\partial n}\int_{C_b}\boldsymbol{f}_w^{(e)}dC_b=\sum_{M}J_z^{(e)}\iint_{\Omega^{(e)}}\boldsymbol{f}_w^{(e)}dxdy, \qquad (2.30)$$

where M is the total number of elements within the domain. e refers to the e^{th} element.

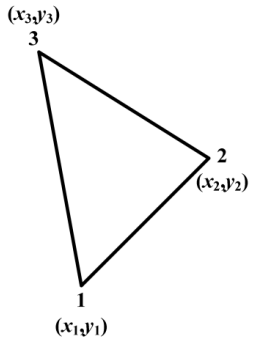

Fig. 2.9. Triangular element.

The line integral in eqn. (2.30) is determined only over the boundary elements. Applying zero homogenous Neumann boundary condition, also known as natural boundary condition, the term $\frac{\partial A_z^{(e)}}{\partial n}$ equals zero [1, 72]. This leads to:

$$\sum_{M}\iint_{\Omega^{(e)}}\frac{1}{\mu^{(e)}}\left(\frac{\partial \boldsymbol{f}_w^{(e)}}{\partial x}\frac{\partial A_z^{(e)}}{\partial x}+\frac{\partial \boldsymbol{f}_w^{(e)}}{\partial y}\frac{\partial A_z^{(e)}}{\partial y}\right)dxdy=\sum_{M}J_z^{(e)}\iint_{\Omega^{(e)}}\boldsymbol{f}_w^{(e)}dxdy \qquad (2.31)$$

In the Galerkin method, the weighting function is the finite element shape function. Thus, expressions of the e^{th} element magnetic vector potential and shape functions are needed.

The magnetic vector potential is assumed to vary linearly within a triangular element such as the one shown in Fig. 2.9. Thus the magnetic vector potential of the e^{th} element $A_z^{(e)}$ is obtained from [72]:

$$A_z^{(e)} = a + bx + cy, \tag{2.32}$$

where a, b and c are constants.

The e^{th} element magnetic vector potentials at nodes 1, 2, and 3 are obtained from [1, 72]

$$\begin{aligned} A_{z1}^{(e)} &= a + bx_1 + cy_1, \\ A_{z2}^{(e)} &= a + bx_2 + cy_2, \\ A_{z3}^{(e)} &= a + bx_3 + cy_3. \end{aligned} \tag{2.33}$$

The constants a, b, and c can be solved using Kramer's rule [72]:

$$a = \frac{\begin{vmatrix} A_{z1}^{(e)} & x_1 & y_1 \\ A_{z2}^{(e)} & x_2 & y_2 \\ A_{z3}^{(e)} & x_3 & y_3 \end{vmatrix}}{\begin{vmatrix} 1 & x_1 & y_1 \\ 1 & x_2 & y_2 \\ 1 & x_3 & y_3 \end{vmatrix}}. \tag{2.34}$$

Thus

$$a = \frac{1}{2S^{(e)}}\left[A_{z1}^{(e)}(x_2y_3 - x_3y_2) + A_{z2}^{(e)}(x_3y_1 - x_1y_3) + A_{z3}^{(e)}(x_1y_2 - x_2y_1) \right], \tag{2.35}$$

where $S^{(e)}$ is the area of the triangular element which equals

$$S^{(e)} = \frac{1}{2}\begin{vmatrix} 1 & x_1 & y_1 \\ 1 & x_2 & y_2 \\ 1 & x_3 & y_3 \end{vmatrix}. \tag{2.36}$$

Similarly

$$b = \frac{\begin{vmatrix} 1 & A_{z1}^{(e)} & y_1 \\ 1 & A_{z2}^{(e)} & y_2 \\ 1 & A_{z3}^{(e)} & y_3 \end{vmatrix}}{\begin{vmatrix} 1 & x_1 & y_1 \\ 1 & x_2 & y_2 \\ 1 & x_3 & y_3 \end{vmatrix}} = \frac{1}{2S^{(e)}}\left[A_{z1}^{(e)}(y_2 - y_3) + A_{z2}^{(e)}(y_3 - y_1) + A_{z3}^{(e)}(y_1 - y_2) \right], \tag{2.37}$$

$$c=\frac{\begin{vmatrix}1 & x_1 & A_{z1}^{(e)}\\ 1 & x_2 & A_{z2}^{(e)}\\ 1 & x_3 & A_{z3}^{(e)}\end{vmatrix}}{\begin{vmatrix}1 & x_1 & y_1\\ 1 & x_2 & y_2\\ 1 & x_3 & y_3\end{vmatrix}}=\frac{1}{2S^{(e)}}\left[A_{z1}^{(e)}(x_3-x_2)+A_{z2}^{(e)}(x_1-x_3)+A_{z3}^{(e)}(x_2-x_1)\right]. \tag{2.38}$$

Notice from (2.35)-(2.38) that the unknown coefficients are functions of the nodal values. The constants *a*, *b*, and *c* are thus rewritten as [1]:

$$\begin{aligned}a&=\frac{1}{2S^{(e)}}\left[A_{z1}^{(e)}p_1+A_{z2}^{(e)}p_2+A_{z3}^{(e)}p_3\right],\\ b&=\frac{1}{2S^{(e)}}\left[A_{z1}^{(e)}q_1+A_{z2}^{(e)}q_2+A_{z3}^{(e)}q_3\right],\\ c&=\frac{1}{2S^{(e)}}\left[A_{z1}^{(e)}r_1+A_{z2}^{(e)}r_2+A_{z3}^{(e)}r_3\right],\end{aligned} \tag{2.39}$$

where

$$\begin{aligned}p_1&=x_2y_3-x_3y_2,\\ p_2&=x_3y_1-x_1y_3,\\ p_3&=x_1y_2-x_2y_1,\end{aligned} \tag{2.40}$$

$$\begin{aligned}q_1&=y_2-y_3,\\ q_2&=y_3-y_1,\\ q_3&=y_1-y_2,\end{aligned} \tag{2.41}$$

$$\begin{aligned}r_1&=x_3-x_2,\\ r_2&=x_1-x_3,\\ r_3&=x_2-x_1.\end{aligned} \tag{2.42}$$

Substituting eqn. (2.39) into eqn. (2.32) [1, 72]:

$$A_z^{(e)}=\sum_{i=1}^{3}\frac{p_i+q_ix+r_iy}{2S^{(e)}}A_{zi}^{(e)} \tag{2.43}$$

Eqn. (2.43) is rewritten as [1, 72]

$$A_z^{(e)} = \sum_{i=1}^{3} N_i^{(e)} A_{zi}^{(e)}, \tag{2.44}$$

where $N_i^{(e)}$ represents the shape function at the i^{th} node of the e^{th} element. Eqn. (2.44) can be expressed in the matrix form:

$$A_z^{(e)} = \begin{bmatrix} N_1^{(e)} & N_2^{(e)} & N_3^{(e)} \end{bmatrix} \begin{bmatrix} A_{z1}^{(e)} \\ A_{z2}^{(e)} \\ A_{z3}^{(e)} \end{bmatrix}, \tag{2.45}$$

where

$$\begin{aligned} N_1^{(e)} &= \frac{p_1 + q_1 x + r_1 y}{2S^{(e)}}, \\ N_2^{(e)} &= \frac{p_2 + q_2 x + r_2 y}{2S^{(e)}}, \\ N_3^{(e)} &= \frac{p_3 + q_3 x + r_3 y}{2S^{(e)}}. \end{aligned} \tag{2.46}$$

Using (2.45), the derivatives of the magnetic vector potential of the e^{th} element with respect to x and y are obtained by differentiating eqn. (2.45) as follows

$$\begin{aligned} \frac{\partial A_z^{(e)}}{\partial x} &= \frac{1}{2S^{(e)}} \begin{bmatrix} q_1 & q_2 & q_3 \end{bmatrix} \begin{bmatrix} A_{z1}^{(e)} \\ A_{z2}^{(e)} \\ A_{z3}^{(e)} \end{bmatrix}, \\ \frac{\partial A_z^{(e)}}{\partial y} &= \frac{1}{2S^{(e)}} \begin{bmatrix} r_1 & r_2 & r_3 \end{bmatrix} \begin{bmatrix} A_{z1}^{(e)} \\ A_{z2}^{(e)} \\ A_{z3}^{(e)} \end{bmatrix}. \end{aligned} \tag{2.47}$$

For the Galerkin method, the e^{th} element weighting function is given by [72]:

$$\boldsymbol{f}_w^{(e)} = \begin{bmatrix} N_1^{(e)} \\ N_2^{(e)} \\ N_3^{(e)} \end{bmatrix} \tag{2.48}$$

The derivatives of the weighting function with respect to x and y are obtained by differentiating eqn. (2.48) as follows

$$\begin{aligned} \frac{\partial \boldsymbol{f}_w^{(e)}}{\partial x} &= \frac{1}{2S^{(e)}} \begin{bmatrix} q_1 \\ q_2 \\ q_3 \end{bmatrix}, \\ \frac{\partial \boldsymbol{f}_w^{(e)}}{\partial y} &= \frac{1}{2S^{(e)}} \begin{bmatrix} r_1 \\ r_2 \\ r_3 \end{bmatrix}. \end{aligned} \tag{2.49}$$

Substituting from (2.47) and (2.49) into the left-hand side of eqn. (2.31)

$$LHS = \sum_M \iint_{\Omega^{(e)}} \frac{1}{4\mu^{(e)} S^{(e)2}} \left(\begin{bmatrix} q_1 \\ q_2 \\ q_3 \end{bmatrix} \begin{bmatrix} q_1 & q_2 & q_3 \end{bmatrix} \begin{bmatrix} A_{z1}^{(e)} \\ A_{z2}^{(e)} \\ A_{z3}^{(e)} \end{bmatrix} + \begin{bmatrix} r_1 \\ r_2 \\ r_3 \end{bmatrix} \begin{bmatrix} r_1 & r_2 & r_3 \end{bmatrix} \begin{bmatrix} A_{z1}^{(e)} \\ A_{z2}^{(e)} \\ A_{z3}^{(e)} \end{bmatrix} \right) dxdy, \tag{2.50}$$

and

$$\iint_{\Omega^{(e)}} dxdy = S^{(e)} \tag{2.51}$$

Thus

$$LHS = \sum_M \frac{1}{4\mu^{(e)} S^{(e)}} \begin{pmatrix} q_1^2 + r_1^2 & q_1 q_2 + r_1 r_2 & q_1 q_3 + r_1 r_3 \\ q_2 q_1 + r_2 r_1 & q_2^2 + r_2^2 & q_2 q_3 + r_2 r_3 \\ q_3 q_1 + r_3 r_1 & q_3 q_2 + r_3 r_2 & q_3^2 + r_3^2 \end{pmatrix} \begin{bmatrix} A_{z1}^{(e)} \\ A_{z2}^{(e)} \\ A_{z3}^{(e)} \end{bmatrix}. \tag{2.52}$$

The coefficient matrix in eqn. (2.52) is the local stiffness matrix $\boldsymbol{K}^{(e)} \in \Re^{3\times 3}$ whose terms are obtained from [1]

$$K_{ij}^{(e)} = \frac{1}{4\mu^{(e)} S^{(e)}}\left(q_i q_j + r_i r_j\right), \qquad i, j = 1,2,3 \tag{2.53}$$

Substituting eqns. (2.46) and (2.48) into the right-hand side of eqn. (2.31), then

$$RHS = \sum_M J_z^{(e)} \iint_{\Omega^{(e)}} \begin{bmatrix} N_1^{(e)} \\ N_2^{(e)} \\ N_3^{(e)} \end{bmatrix} dxdy = \sum_M J_z^{(e)} \iint_{\Omega^{(e)}} \begin{bmatrix} \dfrac{p_1 + q_1 x + r_1 y}{2S^{(e)}} \\ \dfrac{p_2 + q_2 x + r_2 y}{2S^{(e)}} \\ \dfrac{p_3 + q_3 x + r_3 y}{2S^{(e)}} \end{bmatrix} dxdy = \sum_M J_z^{(e)} \begin{bmatrix} \dfrac{p_1 + q_1 \bar{x} + r_1 \bar{y}}{2} \\ \dfrac{p_2 + q_2 \bar{x} + r_2 \bar{y}}{2} \\ \dfrac{p_3 + q_3 \bar{x} + r_3 \bar{y}}{2} \end{bmatrix} \tag{2.54}$$

where $\bar{x}$ and $\bar{y}$ represent the coordinates of the triangular element centroid which are obtained from [72]

$$\begin{aligned} \bar{x} &= \frac{1}{3}\left(x_1 + x_2 + x_3\right), \\ \bar{y} &= \frac{1}{3}\left(y_1 + y_2 + y_3\right). \end{aligned} \tag{2.55}$$

Substituting eqns. (2.40), (2.41), (2.42), and (2.55) into eqn. (2.54), then

$$RHS = \frac{S^{(e)}}{3} \begin{bmatrix} J_z^{(e)} \\ J_z^{(e)} \\ J_z^{(e)} \end{bmatrix}. \tag{2.56}$$

This right-hand side term is known as the local forcing vector $\boldsymbol{Q}^{(e)} \in \Re^{3\times 1}$.

After obtaining the stiffness matrix and forcing vector for all domain elements, these local matrices and vectors are then assembled to get the global stiffness matrix $\boldsymbol{K} \in \Re^{N_n \times N_n}$ and forcing vector $\boldsymbol{Q} \in \Re^{N_n \times 1}$, respectively where N_n is the total number of domain nodes.

After the assembly process, the boundary conditions are imposed to the global system of equations. There are two common types of boundary conditions in magnetostatic field analysis. Neumann's boundary condition which has been assigned while deriving the system of equations. Dirichlet boundary condition which is applied by assigning zeros to the magnetic vector potential of the boundary nodes. This is obtained by assigning zeros to the terms of the k^{th} row of the global stiffness matrix, assuming the k^{th} node lies on the Dirichlet boundary, while the principal diagonal term is assigned to unity. Zero is also allocated to the k^{th} row of the global forcing vector [1].

The magnetic vector potential $\boldsymbol{A}_z \in \Re^{N_n \times 1}$ of the whole nodes within the domain is obtained by solving the following system of equations [1, 72]

$$\boldsymbol{K}\boldsymbol{A}_z = \boldsymbol{Q}. \tag{2.57}$$

2.3.2 Magnetostatic Field Analysis (Nonlinear Case)

For a nonlinear magnetostatic problem, the field distribution throughout the domain is obtained by solving Poisson's equation [80]:

$$\frac{\partial}{\partial x}\left(v(B) \cdot \frac{\partial A_z}{\partial x} \right) + \frac{\partial}{\partial y}\left(v(B) \cdot \frac{\partial A_z}{\partial y} \right) = -J_z, \tag{2.58}$$

where v is the magnetic reluctivity and B is the magnitude of the magnetic flux density.

By discretizing the domain into small triangular elements, equation (2.58) is rewritten in the form of the system of equations in (2.59) [1]:

$$\boldsymbol{K}(\boldsymbol{v}, \boldsymbol{p})\boldsymbol{A}_z = \boldsymbol{Q}, \tag{2.59}$$

where $\boldsymbol{v}$ is the vector of element reluctivity of the nonlinear magnetic material and $\boldsymbol{p}$ represents the geometric parameters within the domain. In solving (2.59), a mathematical

model of the nonlinear magnetic properties of the material is required. The local reluctivity of the e^{th} element $\nu^{(e)}$ is commonly expressed as a function of $B^{(e)}$, which is the magnitude of the 2D local flux density $\boldsymbol{B}^{(e)} = \left(B_x^{(e)}, B_y^{(e)}\right)$.

Iterative methods such as Newton-Raphson method may be used to solve this system of equations. This method will be explained as follows; from eqns. (2.52), (2.53), and (2.56), the following system of equations is obtained for the e^{th} element

$$\frac{\nu^{(e)}}{4S^{(e)}}\begin{pmatrix} M_{11}^{(e)} & M_{12}^{(e)} & M_{13}^{(e)} \\ M_{21}^{(e)} & M_{22}^{(e)} & M_{23}^{(e)} \\ M_{31}^{(e)} & M_{32}^{(e)} & M_{33}^{(e)} \end{pmatrix}\begin{bmatrix} A_{z1}^{(e)} \\ A_{z2}^{(e)} \\ A_{z3}^{(e)} \end{bmatrix} = \frac{S^{(e)}}{3}\begin{bmatrix} J_z^{(e)} \\ J_z^{(e)} \\ J_z^{(e)} \end{bmatrix}, \tag{2.60}$$

where

$$M_{ij}^{(e)} = q_i q_j + r_i r_j, \qquad i, j = 1, 2, 3 \tag{2.61}$$

The matrix equation (2.60) is decomposed into three equations that represent the rows [72]

$$E_1 = \frac{\nu^{(e)}}{4S^{(e)}}\begin{bmatrix} M_{11}^{(e)} & M_{12}^{(e)} & M_{13}^{(e)} \end{bmatrix}\begin{bmatrix} A_{z1}^{(e)} \\ A_{z2}^{(e)} \\ A_{z3}^{(e)} \end{bmatrix} - \frac{S^{(e)} J_z^{(e)}}{3}, \tag{2.62}$$

$$E_2 = \frac{\nu^{(e)}}{4S^{(e)}}\begin{bmatrix} M_{21}^{(e)} & M_{22}^{(e)} & M_{23}^{(e)} \end{bmatrix}\begin{bmatrix} A_{z1}^{(e)} \\ A_{z2}^{(e)} \\ A_{z3}^{(e)} \end{bmatrix} - \frac{S^{(e)} J_z^{(e)}}{3}, \tag{2.63}$$

$$E_3 = \frac{\nu^{(e)}}{4S^{(e)}}\begin{bmatrix} M_{31}^{(e)} & M_{32}^{(e)} & M_{33}^{(e)} \end{bmatrix}\begin{bmatrix} A_{z1}^{(e)} \\ A_{z2}^{(e)} \\ A_{z3}^{(e)} \end{bmatrix} - \frac{S^{(e)} J_z^{(e)}}{3}. \tag{2.64}$$

The derivatives of the first equation with respect to the e^{th} element magnetic vector potentials are as follows

$$\frac{\partial E_1}{\partial A_{z1}^{(e)}} = \frac{v^{(e)}}{4S^{(e)}} M_{11}^{(e)} + \frac{1}{4S^{(e)}} \left[M_{11}^{(e)} A_{z1}^{(e)} + M_{12}^{(e)} A_{z2}^{(e)} + M_{13}^{(e)} A_{z3}^{(e)} \right] \frac{\partial v^{(e)}}{\partial A_{z1}^{(e)}}, \tag{2.65}$$

$$\frac{\partial E_1}{\partial A_{z2}^{(e)}} = \frac{v^{(e)}}{4S^{(e)}} M_{12}^{(e)} + \frac{1}{4S^{(e)}} \left[M_{11}^{(e)} A_{z1}^{(e)} + M_{12}^{(e)} A_{z2}^{(e)} + M_{13}^{(e)} A_{z3}^{(e)} \right] \frac{\partial v^{(e)}}{\partial A_{z2}^{(e)}}, \tag{2.66}$$

$$\frac{\partial E_1}{\partial A_{z3}^{(e)}} = \frac{v^{(e)}}{4S^{(e)}} M_{13}^{(e)} + \frac{1}{4S^{(e)}} \left[M_{11}^{(e)} A_{z1}^{(e)} + M_{12}^{(e)} A_{z2}^{(e)} + M_{13}^{(e)} A_{z3}^{(e)} \right] \frac{\partial v^{(e)}}{\partial A_{z3}^{(e)}}. \tag{2.67}$$

Applying the Newton-Raphson approach to the first equation, then

$$\frac{\partial E_1}{\partial A_{z1}^{(e)}} \Delta A_{z1}^{(e)} + \frac{\partial E_1}{\partial A_{z2}^{(e)}} \Delta A_{z2}^{(e)} + \frac{\partial E_1}{\partial A_{z3}^{(e)}} \Delta A_{z3}^{(e)} = -E_1 \tag{2.68}$$

Substituting eqns. (2.65) – (2.67) into eqn. (2.68), then

$$\begin{aligned}
&\frac{v^{(e)}}{4S^{(e)}} \begin{bmatrix} M_{11}^{(e)} & M_{12}^{(e)} & M_{13}^{(e)} \end{bmatrix} \begin{bmatrix} \Delta A_{z1}^{(e)} \\ \Delta A_{z2}^{(e)} \\ \Delta A_{z3}^{(e)} \end{bmatrix} \\
&+ \frac{1}{4S^{(e)}} \begin{bmatrix} \sum_{n=1}^{3} M_{1n}^{(e)} A_{zn}^{(e)} \frac{\partial v^{(e)}}{\partial A_{z1}^{(e)}} & \sum_{n=1}^{3} M_{1n}^{(e)} A_{zn}^{(e)} \frac{\partial v^{(e)}}{\partial A_{z2}^{(e)}} & \sum_{n=1}^{3} M_{1n}^{(e)} A_{zn}^{(e)} \frac{\partial v^{(e)}}{\partial A_{z3}^{(e)}} \end{bmatrix} \begin{bmatrix} \Delta A_{z1}^{(e)} \\ \Delta A_{z2}^{(e)} \\ \Delta A_{z3}^{(e)} \end{bmatrix} \\
&= \frac{-v^{(e)}}{4S^{(e)}} \begin{bmatrix} M_{11}^{(e)} & M_{12}^{(e)} & M_{13}^{(e)} \end{bmatrix} \begin{bmatrix} A_{z1}^{(e)} \\ A_{z2}^{(e)} \\ A_{z3}^{(e)} \end{bmatrix} + \frac{J_z^{(e)} S^{(e)}}{3}
\end{aligned} \tag{2.69}$$

A similar procedure is followed for the other two equations, then combining the three equations result in

$$
\begin{aligned}
&\frac{\nu^{(e)}}{4S^{(e)}}\begin{bmatrix} M_{11}^{(e)} & M_{12}^{(e)} & M_{13}^{(e)} \\ M_{21}^{(e)} & M_{22}^{(e)} & M_{23}^{(e)} \\ M_{31}^{(e)} & M_{32}^{(e)} & M_{33}^{(e)} \end{bmatrix}\begin{bmatrix} \Delta A_{z1}^{(e)} \\ \Delta A_{z2}^{(e)} \\ \Delta A_{z3}^{(e)} \end{bmatrix} \\
&+\frac{1}{4S^{(e)}}\begin{bmatrix} \sum_{n=1}^{3} M_{1n}^{(e)} A_{zn}^{(e)} \dfrac{\partial \nu^{(e)}}{\partial A_{z1}^{(e)}} & \sum_{n=1}^{3} M_{1n}^{(e)} A_{zn}^{(e)} \dfrac{\partial \nu^{(e)}}{\partial A_{z2}^{(e)}} & \sum_{n=1}^{3} M_{1n}^{(e)} A_{zn}^{(e)} \dfrac{\partial \nu^{(e)}}{\partial A_{z3}^{(e)}} \\ \sum_{n=1}^{3} M_{2n}^{(e)} A_{zn}^{(e)} \dfrac{\partial \nu^{(e)}}{\partial A_{z1}^{(e)}} & \sum_{n=1}^{3} M_{2n}^{(e)} A_{zn}^{(e)} \dfrac{\partial \nu^{(e)}}{\partial A_{z2}^{(e)}} & \sum_{n=1}^{3} M_{2n}^{(e)} A_{zn}^{(e)} \dfrac{\partial \nu^{(e)}}{\partial A_{z3}^{(e)}} \\ \sum_{n=1}^{3} M_{3n}^{(e)} A_{zn}^{(e)} \dfrac{\partial \nu^{(e)}}{\partial A_{z1}^{(e)}} & \sum_{n=1}^{3} M_{3n}^{(e)} A_{zn}^{(e)} \dfrac{\partial \nu^{(e)}}{\partial A_{z2}^{(e)}} & \sum_{n=1}^{3} M_{3n}^{(e)} A_{zn}^{(e)} \dfrac{\partial \nu^{(e)}}{\partial A_{z3}^{(e)}} \end{bmatrix}\begin{bmatrix} \Delta A_{z1}^{(e)} \\ \Delta A_{z2}^{(e)} \\ \Delta A_{z3}^{(e)} \end{bmatrix} \\
&=\frac{-\nu^{(e)}}{4S^{(e)}}\begin{bmatrix} M_{11}^{(e)} & M_{12}^{(e)} & M_{13}^{(e)} \\ M_{21}^{(e)} & M_{22}^{(e)} & M_{23}^{(e)} \\ M_{31}^{(e)} & M_{32}^{(e)} & M_{33}^{(e)} \end{bmatrix}\begin{bmatrix} A_{z1}^{(e)} \\ A_{z2}^{(e)} \\ A_{z3}^{(e)} \end{bmatrix}+\frac{J_z^{(e)} S^{(e)}}{3}\begin{bmatrix} 1 \\ 1 \\ 1 \end{bmatrix}
\end{aligned}
\tag{2.70}
$$

First, the magnetic vector potentials at all domain nodes are assumed to be zeros. The matrices of eqn. (2.70) are then calculated. The local matrices and vectors are assembled, and Dirichlet boundary conditions are applied. The global equation is then solved for $\Delta \boldsymbol{A}_z \in \Re^{3\times 1}$. $\boldsymbol{A}_z$ is then obtained by adding $\Delta \boldsymbol{A}_z$ to the previous value of $\boldsymbol{A}_z$. This process continues until a stopping criterion is met.

2.4 Calculation of SRM responses Using Finite Element Method

The switched reluctance motor is discretized into small triangular elements. A possible discretization of part of the motor domain is shown in Fig. 2.10.

The systems (2.57) or (2.59) for linear or nonlinear materials are solved for the magnetic vector potential throughout the motor domain. The obtained magnetic vector potential $\boldsymbol{A}_z$ is then post-processed to estimate different SRM electromagnetic quantities.

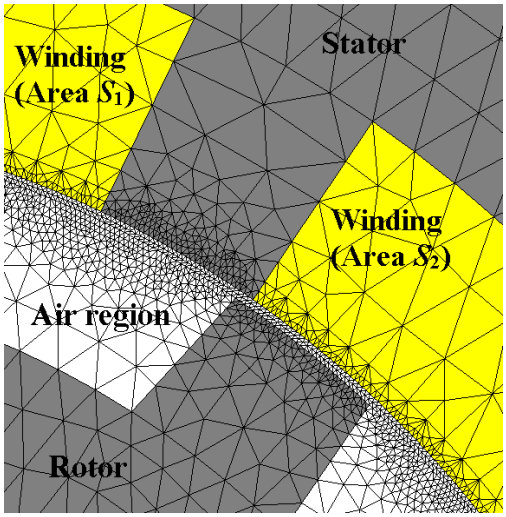

Fig. 2.10. A discretization of a part of an SRM.

2.4.1 Flux Density

The magnetic vector potential varies linearly over the triangular element. The flux density, which is the derivative of the magnetic vector potential, is constant throughout the element.

The e^{th} element flux-density vector is obtained from

$$\boldsymbol{B}^{(e)} = \nabla \times A_z^{(e)} = \frac{\partial A_z^{(e)}}{\partial y}\boldsymbol{a}_x - \frac{\partial A_z^{(e)}}{\partial x}\boldsymbol{a}_y, \tag{2.71}$$

where $\boldsymbol{a}_x$ and $\boldsymbol{a}_y$ are the unit vectors in the x and y directions, respectively.

Substituting eqn. (2.32) into eqn. (2.71) then [1]

$$\boldsymbol{B}^{(e)} = c\boldsymbol{a}_x - b\boldsymbol{a}_y. \tag{2.72}$$

Thus the x and y components of local flux density, $B_x^{(e)}$ and $B_y^{(e)}$, are obtained from [81]:

$$B_x^{(e)} = \frac{1}{2S^{(e)}}\begin{bmatrix} r_1 & r_2 & r_3 \end{bmatrix}\boldsymbol{A}_z^{(e)}, \tag{2.73}$$

$$B_y^{(e)} = \frac{-1}{2S^{(e)}}\begin{bmatrix} q_1 & q_2 & q_3 \end{bmatrix}\boldsymbol{A}_z^{(e)}. \tag{2.74}$$

2.4.2 Air-region Energy

Air region energy W_{AR} is obtained by summing the magnetic energies of all air region finite elements

$$W_{AR} = \sum_{e=1}^{e=N_{e,AR}} W^{(e)}, \tag{2.75}$$

where e is element number and $N_{e,AR}$ is the total number of air region elements. The magnetic energy for each air region element $W^{(e)}$ is obtained from [72]

$$W^{(e)} = \frac{L}{2} \iint_{e} \boldsymbol{B} \cdot \boldsymbol{H} \; dxdy, \tag{2.76}$$

where $\boldsymbol{B}$ and $\boldsymbol{H}$ are the magnetic flux density and the magnetic field strength vectors, respectively. L is the axial length in the z-direction.

For an air region, where the medium is linear, eqn. (2.76) becomes

$$W^{(e)} = \frac{L}{2\mu^{(e)}} B^{(e)2} S^{(e)}, \tag{2.77}$$

where $B^{(e)}$ is the e^{th} element magnitude of the local flux density vector $\boldsymbol{B}^{(e)}$

$$B^{(e)} = \sqrt{\frac{1}{4S^{(e)2}} \left(\left(A_{z1}^{(e)} q_1 + A_{z2}^{(e)} q_2 + A_{z3}^{(e)} q_3 \right)^2 + \left(A_{z1}^{(e)} r_1 + A_{z2}^{(e)} r_2 + A_{z3}^{(e)} r_3 \right)^2 \right)}. \tag{2.78}$$

Substituting (2.78) into (2.77) results in [81]

$$W^{(e)} = \frac{L}{8\mu^{(e)} S^{(e)}} \left(\left(A_{z1}^{(e)} q_1 + A_{z2}^{(e)} q_2 + A_{z3}^{(e)} q_3 \right)^2 + \left(A_{z1}^{(e)} r_1 + A_{z2}^{(e)} r_2 + A_{z3}^{(e)} r_3 \right)^2 \right). \tag{2.79}$$

According to eqn. (2.53), the magnetic energy could be cast in the form [81]:

$$W^{(e)} = \frac{L}{2} \boldsymbol{A}_z^{(e)T} \boldsymbol{K}^{(e)} \boldsymbol{A}_z^{(e)}. \tag{2.80}$$

2.4.3 Electromagnetic Torque

The electromagnetic torque is calculated by summing up torque contributions of the first layer of elements surrounding the moving part [81, 82] (shown as white elements in Fig. 2.11.

Each element contribution to the torque is obtained by differentiating the magnetic energy within each element with respect to a virtual angle of rotation θ at constant flux linkage [82]

$$T^{(e)} = -\frac{\partial W^{(e)}}{\partial \theta} \text{ at constant flux linkage.} \tag{2.81}$$

Substituting eqn. (2.80) into eqn. (2.81) then [82, 83]

$$T^{(e)} = -\frac{\partial}{\partial \theta}\left(\frac{L}{2} \boldsymbol{A}_z^{(e)T} \boldsymbol{K}^{(e)} \boldsymbol{A}_z^{(e)}\right). \tag{2.82}$$

The magnetic vector potential is constant since the torque is calculated at constant flux linkage. Thus eqn. (2.82) is rewritten as [72, 82]

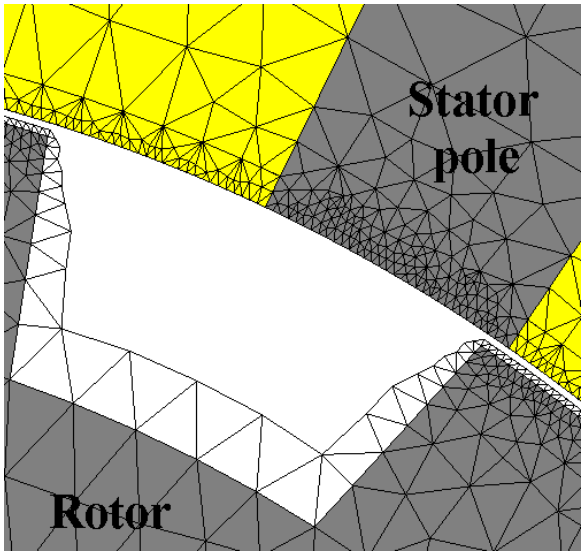

Fig. 2.11. The first layer of elements of the air region (white elements) around the rotor.

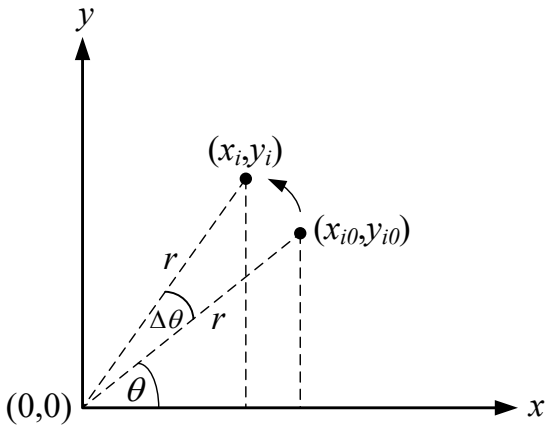

Fig. 2.12. The rotation of moving nodes coordinates by an infinitesimal angle of $\Delta\theta$.

$$T^{(e)} = -\frac{L}{2} \boldsymbol{A}_z^{(e)T} \frac{\partial \boldsymbol{K}^{(e)}}{\partial \theta} \boldsymbol{A}_z^{(e)}. \tag{2.83}$$

Using eqn. (2.53), the term $\partial \boldsymbol{K}^{(e)} / \partial \theta$ is calculated as follows

$$\frac{\partial K_{ij}^{(e)}}{\partial \theta} = \frac{S^{(e)} \left(\frac{\partial q_i}{\partial \theta} q_j + q_i \frac{\partial q_j}{\partial \theta} + \frac{\partial r_i}{\partial \theta} r_j + r_i \frac{\partial r_j}{\partial \theta} \right) - \left(q_i q_j + r_i r_j \right) \frac{\partial S^{(e)}}{\partial \theta}}{4 \mu^{(e)} S^{(e)2}}, \; i, j = 1, 2, 3 \tag{2.84}$$

The derivatives of the coordinates of the e^{th} element moving nodes with respect to the virtual angle θ can be obtained using the homogeneous-coordinates technique [82, 84].

Referring to Fig. 2.12, the initial coordinates before rotation, x_{i0} and y_{i0}, of the moving nodes are obtained from

$$x_{i0} = r \cos \theta, \tag{2.85}$$

$$y_{i0} = r \sin \theta, \tag{2.86}$$

where i is the node index of e^{th} element i.e. i=1, 2, 3. The coordinates of the moving nodes after rotation by an infinitesimal angle of $\Delta\theta$ (x_i and y_i), around the z-axis are obtained from

$$x_i = r\cos\left(\theta + \Delta\theta\right) = r\cos\theta\cos\Delta\theta - r\sin\theta\sin\Delta\theta, \tag{2.87}$$

$$y_i = r\sin\left(\theta + \Delta\theta\right) = r\sin\theta\cos\Delta\theta + r\cos\theta\sin\Delta\theta. \tag{2.88}$$

Differentiating (2.87) and (2.88) with respect to θ and taking the limit as $\Delta\theta \to 0$, it can be shown that [82]

$$\frac{\partial x_i}{\partial\theta} = -y_{i0}, \ \frac{\partial y_i}{\partial\theta} = x_{i0}. \tag{2.89}$$

2.4.2 Flux linkage

The flux linkage per phase ψ, with one current path of the stator winding, is obtained from [81, 85]

$$\psi = 2p\left[\frac{N_c L}{S_1}\sum_{e=1}^{N_{e,S_1}} A_{z,avg}^{(e)} S^{(e)} - \frac{N_c L}{S_2}\sum_{e=1}^{N_{e,S_2}} A_{z,avg}^{(e)} S^{(e)}\right] = 2p\left[\psi_{S_1} - \psi_{S_2}\right], \tag{2.90}$$

where $2p$ is the number of poles per phase. N_c is the number of turns per coil. N_{e,S_1} and N_{e,S_2} are the total number of elements in the coil winding areas S_1 and S_2 as shown in Fig. 2.10, respectively. Area S_1 is the coil winding area in which current is positive, i.e., in the same direction of the z-axis, and area S_2 is the coil winding area in which current is negative. $A_{z,avg}^{(e)}$ is the average value of the magnetic vector potential over the e^{th} element [85]. ψ_{S_1} and ψ_{S_2} are the total flux linkage contributions of all elements in areas S_1 and S_2, respectively.

This page is intentionally left blank

Chapter 3

Adjoint Sensitivity Analysis

3.1 Introduction

The sensitivities of any objective function/response f with respect to all parameters $\boldsymbol{p}$, including physical and shape parameters, can be classically estimated using finite difference approximations [86-89]. The accurate Central Finite Difference (CFD) approximation requires two extra simulations per parameter [49, 87, 90, 91]. It effectively averages the forward and backward sensitivities as shown in Fig. 3.1. The forward and backward sensitivities are obtained from (3.1) and (3.2), respectively [49]:

$$\frac{\partial f}{\partial p_i} \approx \frac{f(p_i + \Delta p_i) - f(p_i)}{\Delta p_i}, \; i = 1, \; 2, \ldots\ldots, n, \tag{3.1}$$

$$\frac{\partial f}{\partial p_i} \approx \frac{f(p_i) - f(p_i - \Delta p_i)}{\Delta p_i}, \; i = 1, \; 2, \ldots\ldots, n, \tag{3.2}$$

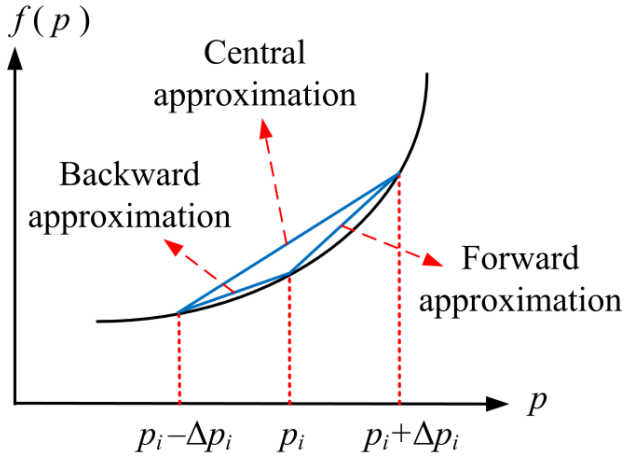

Fig. 3.1. Forward, backward, and central finite differences.

where p_i is the i^{th} parameter and Δp_i is the i^{th} parameter perturbation. The CFD sensitivity estimates are calculated by summing (3.1) and (3.2) and dividing by 2 [49, 91]:

$$\frac{\partial f}{\partial p_i} \approx \frac{f(p_i + \Delta p_i) - f(p_i - \Delta p_i)}{2\Delta p_i},\ i = 1,\ 2,.....,n \tag{3.3}$$

This approximation is more accurate than forward and backward differences but is more computationally expensive.

Another approach of estimating sensitivities is the Adjoint Variable Method (AVM). AVM requires only one extra simulation to evaluate the sensitivities of an objective function/response *f* with respect to all parameters regardless of their number [49, 87, 90].

3.2 Sensitivity Analysis

In this Section, we show how the AVM method can be applied to SRMs. We derive the governing equations and the quantities required to calculate the sensitivities of the desired response with respect to all parameters.

3.2.1 Adjoint Variable Method (Linear Case)

For the following linear system of equations [49]:

$$\boldsymbol{Z}(\boldsymbol{p})\boldsymbol{I} = \boldsymbol{V}, \tag{3.4}$$

the elements of the system matrix $\boldsymbol{Z}$ are functions of the parameters $\boldsymbol{p}$. The column vector $\boldsymbol{I}$ represents the state variables (electric field, magnetic field, or magnetic vector potential) and $\boldsymbol{V}$ is the excitation vector [49, 92].

Differentiating (3.4) with respect to the i^{th} parameter p_i gives [49]

$$\boldsymbol{Z}\frac{\partial \boldsymbol{I}}{\partial p_i} + \frac{\partial \boldsymbol{Z}}{\partial p_i}\boldsymbol{I} = \frac{\partial \boldsymbol{V}}{\partial p_i}, \tag{3.5}$$

which gives the derivatives of the state variables:

$$\frac{\partial \boldsymbol{I}}{\partial p_i} = \boldsymbol{Z}^{-1}\left(\frac{\partial \boldsymbol{V}}{\partial p_i} - \frac{\partial \boldsymbol{Z}}{\partial p_i}\boldsymbol{I}\right). \tag{3.6}$$

The gradient of any objective function or response $f(\boldsymbol{p},\boldsymbol{I})$ with respect to the i^{th} parameter p_i is obtained from [49]

$$\frac{\partial f}{\partial p_i} = \left(\frac{\partial f}{\partial p_i}\right)_{explicit} + \left(\frac{\partial f}{\partial \boldsymbol{I}}\right)^T \frac{\partial \boldsymbol{I}}{\partial p_i}, \ \forall i. \tag{3.7}$$

The first term on the right-hand side represents the explicit dependence of the objective function on the i^{th} parameter p_i . The second term is the implicit dependence of f on p_i through the state variables $\boldsymbol{I}$.

Substituting from (3.6) into (3.7), the sensitivity of f with respect to the i^{th} parameter can be written as [49, 92]:

$$\frac{\partial f}{\partial p_i} = \left(\frac{\partial f}{\partial p_i}\right)_{explicit} + \hat{\boldsymbol{I}}^T\left(\frac{\partial \boldsymbol{V}}{\partial p_i} - \frac{\partial \boldsymbol{Z}}{\partial p_i}\boldsymbol{I}\right), \ \forall i, \tag{3.8}$$

where $\hat{\boldsymbol{I}}$ is the vector of adjoint state variables. This vector is obtained by solving the adjoint system [49, 92]:

$$\boldsymbol{Z}^T\hat{\boldsymbol{I}} = \left(\frac{\partial f}{\partial \boldsymbol{I}}\right). \tag{3.9}$$

The terms $\partial \boldsymbol{V}/\partial p_i$ and $\partial \boldsymbol{Z}/\partial p_i$ are the derivatives of the excitation vector and the system matrix with respect to p_i, respectively. These derivatives can be obtained analytically or numerically. Here, they are obtained numerically by applying finite differences to the matrices and excitation of the original system [49].

3.2.2 Adjoint Variable Method (Nonlinear Case)

Considering a system of nonlinear equations:

$$\boldsymbol{Z}\left(\boldsymbol{p},\boldsymbol{I}\right)\boldsymbol{I}=\boldsymbol{V}, \tag{3.10}$$

where the elements of the system matrix $\boldsymbol{Z}$ are functions of parameters $\boldsymbol{p}$ and state variables $\boldsymbol{I}$.

The residual vector $\boldsymbol{R}$ of this system is given by [93, 94]

$$\boldsymbol{R}=\boldsymbol{Z}\left(\boldsymbol{p},\boldsymbol{I}\right)\boldsymbol{I}-\boldsymbol{V}=\boldsymbol{0}. \tag{3.11}$$

Differentiating $\boldsymbol{R}$ with respect to design parameter p_i [94]

$$\frac{\partial \boldsymbol{R}}{\partial p_i}=\left.\frac{\partial \boldsymbol{R}}{\partial p_i}\right|_{\boldsymbol{I}=\bar{\boldsymbol{I}}}+\left.\frac{\partial \boldsymbol{R}}{\partial \boldsymbol{I}^T}\right|_{p_i=\bar{p}_i}\frac{\partial \boldsymbol{I}}{\partial p_i}, \tag{3.12}$$

where $\bar{\boldsymbol{I}}$ and $\bar{p}_i$ are the nominal state variables and nominal value of the i^{th} design parameter respectively. Applying (3.12) to (3.11), we have

$$\left.\frac{\partial \boldsymbol{Z}}{\partial p_i}\right|_{\boldsymbol{I}=\bar{\boldsymbol{I}}}\bar{\boldsymbol{I}}-\left.\frac{\partial \boldsymbol{V}}{\partial p_i}\right|_{\boldsymbol{I}=\bar{\boldsymbol{I}}}+\left[\boldsymbol{Z}+\left.\frac{\partial\left(\boldsymbol{Z}\bar{\boldsymbol{I}}\right)}{\partial \boldsymbol{I}^T}\right|_{p_i=\bar{p}_i}\right]\frac{\partial \boldsymbol{I}}{\partial p_i}=\boldsymbol{0}. \tag{3.13}$$

Solving for derivatives of the state variables, one obtains:

$$\frac{\partial \boldsymbol{I}}{\partial p_i}=\left[\boldsymbol{Z}+\left.\frac{\partial\left(\boldsymbol{Z}\bar{\boldsymbol{I}}\right)}{\partial \boldsymbol{I}^T}\right|_{p_i=\bar{p}_i}\right]^{-1}\left[\left.\frac{\partial \boldsymbol{V}}{\partial p_i}\right|_{\boldsymbol{I}=\bar{\boldsymbol{I}}}-\left.\frac{\partial \boldsymbol{Z}}{\partial p_i}\right|_{\boldsymbol{I}=\bar{\boldsymbol{I}}}\bar{\boldsymbol{I}}\right]. \tag{3.14}$$

Using AVM, the gradient of any objective function $f\left(\boldsymbol{p},\boldsymbol{I}\right)$ with respect to parameters $\boldsymbol{p}$ is obtained using [49, 93, 94]

$$\frac{\partial f}{\partial p_i} = \left(\frac{\partial f}{\partial p_i} \right)_{explicit} + \left(\frac{\partial f}{\partial \boldsymbol{I}} \right)^T \frac{\partial \boldsymbol{I}}{\partial p_i}, \ \forall i. \tag{3.15}$$

The first term on the right-hand side represents the explicit dependence of the objective function on the i^{th} parameter p_i. The second term is the implicit dependence of f on p_i through the state variables. Substituting from (3.14) into (3.15) then

$$\frac{\partial f}{\partial p_i} = \left(\frac{\partial f}{\partial p_i} \right)_{explicit} + \hat{\boldsymbol{I}}^T \left[\left. \frac{\partial \boldsymbol{V}}{\partial p_i} \right|_{\boldsymbol{I}=\bar{\boldsymbol{I}}} - \left. \frac{\partial \boldsymbol{Z}}{\partial p_i} \right|_{\boldsymbol{I}=\bar{\boldsymbol{I}}} \bar{\boldsymbol{I}} \right], \forall i, \tag{3.16}$$

where the vector of adjoint state variables $\hat{\boldsymbol{I}}$ is defined such that [93-95]

$$\left[\boldsymbol{Z} + \left. \frac{\partial \left(\boldsymbol{Z}\bar{\boldsymbol{I}} \right)}{\partial \boldsymbol{I}^T} \right|_{p_i = \bar{p}_i} \right]^T \hat{\boldsymbol{I}} = \left(\frac{\partial f}{\partial \boldsymbol{I}} \right). \tag{3.17}$$

The terms $\partial \boldsymbol{V} / \partial p_i$ and $\partial \boldsymbol{Z} / \partial p_i$ are the derivatives of the excitation vector and system matrix with respect to the i^{th} parameter p_i respectively. $\partial \boldsymbol{V} / \partial p_i$ can be obtained analytically or numerically by applying finite differences to the excitation of the original system [49, 96]. $\partial \boldsymbol{Z} / \partial p_i$ should be obtained analytically since calculating it numerically using finite differences require extra simulation due to the existing nonlinearity where $\boldsymbol{Z}$ is a function of the state variables $\boldsymbol{I}$.

This page is intentionally left blank

Chapter 4

Adjoint Sensitivity Analysis of Switched Reluctance Motors

The adjoint variable method has been introduced in case of linear and nonlinear systems of equations in the previous chapter. Here, the AVM method is applied to switched reluctance motors while utilizing either linear or nonlinear magnetic materials.

4.1 Application of Adjoint Variable Method to SRMs (Linear Case)

Applying AVM on the linear system of equations obtained from the finite element method, eqn. (2.57), the sensitivity of any SRM electromagnetic response *f* with respect to all design parameters can be obtained from

$$\frac{\partial f}{\partial p_i} = \left(\frac{\partial f}{\partial p_i} \right)_{explicit} + \hat{\boldsymbol{A}}_z^T \left(\frac{\partial \boldsymbol{Q}}{\partial p_i} - \frac{\partial \boldsymbol{K}}{\partial p_i} \boldsymbol{A}_z \right), \tag{4.1}$$

where $\partial \boldsymbol{Q} / \partial p_i$ and $\partial \boldsymbol{K} / \partial p_i$ are approximated numerically using:

$$\frac{\partial \boldsymbol{Q}}{\partial p_i} \approx \frac{\boldsymbol{Q}\left(p_i + \Delta p_i\right) - \boldsymbol{Q}\left(p_i\right)}{\Delta p_i}, \tag{4.2}$$

$$\frac{\partial \boldsymbol{K}}{\partial p_i} \approx \frac{\boldsymbol{K}\left(p_i + \Delta p_i\right) - \boldsymbol{K}\left(p_i\right)}{\Delta p_i}. \tag{4.3}$$

It should be noted that if the perturbed design parameter does not have any influence on the excitation region, the term $\partial \boldsymbol{Q} / \partial p_i$ vanishes. $\boldsymbol{A}_z$ is obtained by solving (2.57), and the adjoint magnetic vector potential $\hat{\boldsymbol{A}}_z$ is estimated, according to (3.9), by solving the adjoint system

$$\boldsymbol{K}^T \hat{\boldsymbol{A}}_z = \frac{\partial f}{\partial \boldsymbol{A}_z}. \tag{4.4}$$

4.2 Application of Adjoint Variable Method to SRMs (Nonlinear Case)

The finite element analysis system of equations (2.59) has the same form as (3.10). The components of the stiffness matrix in (2.59) are dependent on different material properties, geometric dimensions, and the magnetic vector potential response. According to (3.16), the sensitivities of any response *f* of a nonlinear SRM with respect to the design parameters are obtained from [97, 98]

$$\frac{\partial f}{\partial p_i} = \left(\frac{\partial f}{\partial p_i} \right)_{explicit} + \hat{\boldsymbol{A}}_z^{\,T} \left[\left. \frac{\partial \boldsymbol{Q}}{\partial p_i} \right|_{\boldsymbol{A}_z = \bar{\boldsymbol{A}}_z} - \left. \frac{\partial \boldsymbol{K}}{\partial p_i} \right|_{\boldsymbol{A}_z = \bar{\boldsymbol{A}}_z} \bar{\boldsymbol{A}}_z \right], \ \forall i, \tag{4.5}$$

where $\bar{\boldsymbol{A}}_z$ is the nominal magnetic vector potential vector. The derivative $\partial \boldsymbol{Q} / \partial p_i$ is obtained numerically using finite differences:

$$\frac{\partial \boldsymbol{Q}}{\partial p_i} \approx \frac{\boldsymbol{Q}(p_i + \Delta p_i) - \boldsymbol{Q}(p_i)}{\Delta p_i}, \forall i. \tag{4.6}$$

Evaluating (4.6) does not require any extra simulations since the excitation vector $\boldsymbol{Q}$ does not depend on $\boldsymbol{A}_z$. If the perturbed design parameter does not affect the excitation region, the corresponding $\partial \boldsymbol{Q} / \partial p_i$ term vanishes [96].

The derivative $\partial \boldsymbol{K} / \partial p_i$ can be obtained by assembling the derivatives $\partial \boldsymbol{K}^{(e)} / \partial p_i$. These matrix derivatives are derived from [99]:

$$\left. \frac{\partial \boldsymbol{K}^{(e)}}{\partial p_i} \right|_{\boldsymbol{A}_z^{(e)} = \bar{\boldsymbol{A}}_z^{(e)}} = \left. \frac{\partial \boldsymbol{K}^{(e)}}{\partial p_i} \right|_{\boldsymbol{A}_z^{(e)} = \bar{\boldsymbol{A}}_z^{(e)}, \nu^{(e)} = \bar{\nu}^{(e)}} + \left. \frac{\partial \boldsymbol{K}^{(e)}}{\partial \nu^{(e)}} \right|_{\boldsymbol{A}_z^{(e)} = \bar{\boldsymbol{A}}_z^{(e)}, p_i = \bar{p}_i} \frac{\partial \nu^{(e)}}{\partial B^{(e)}} \frac{\partial B^{(e)}}{\partial p_i}, \tag{4.7}$$

where $\bar{\nu}^{(e)}$ is the e^{th} element nominal reluctivity.

According to (3.17), the adjoint magnetic vector potential is obtained using [97-99]:

$$\left[\boldsymbol{K}+\frac{\partial\left(\boldsymbol{K}\bar{\boldsymbol{A}}_z\right)}{\partial \boldsymbol{A}_z^T}\right]^T \hat{\boldsymbol{A}}_z=\frac{\partial f}{\partial \boldsymbol{A}_z}, \tag{4.8}$$

where $\partial\left(\boldsymbol{K}\bar{\boldsymbol{A}}_z\right)/\partial \boldsymbol{A}_z^T$ is obtained by assembling $\partial\left(\boldsymbol{K}^{(e)}\bar{\boldsymbol{A}}_z^{(e)}\right)/\partial \boldsymbol{A}_z^{(e)T}$ for all elements. The matrix $\partial\left(\boldsymbol{K}^{(e)}\bar{\boldsymbol{A}}_z^{(e)}\right)/\partial \boldsymbol{A}_z^{(e)T}$ is obtained using [97]

$$\frac{\partial\left(\boldsymbol{K}^{(e)}\bar{\boldsymbol{A}}_z^{(e)}\right)}{\partial \boldsymbol{A}_z^{(e)T}}=\frac{\partial\left(\boldsymbol{K}^{(e)}\bar{\boldsymbol{A}}_z^{(e)}\right)}{\partial \nu^{(e)}}\frac{\partial \nu^{(e)}}{\partial B^{(e)}}\frac{\partial B^{(e)}}{\partial \boldsymbol{A}_z^{(e)T}}, \forall e. \tag{4.9}$$

Eqns. (4.5) to (4.9) are used to obtain the adjoint sensitivity of any objective function with respect to all design parameters in case of a nonlinear system of equations.

4.3 Adjoint Sensitivities of SRM Responses

Adjoint sensitivities of various electromagnetic responses of SRMs will be investigated in the following subsections. The responses include magnetic vector potential, flux density, air-region energy, electromagnetic torque, and flux density.

4.3.1 Magnetic Vector Potential

The sensitivities of the magnetic vector potential at the m^{th} node $f = A_{z,m}$ with respect to p_i can be obtained from eqn. (4.1) or eqn. (4.5) for the linear and nonlinear cases, respectively. The corresponding adjoint magnetic vector potentials are obtained using eqn. (4.4) or (4.8), respectively. The adjoint excitation vector $\partial A_{z,m}/\partial \boldsymbol{A}_z$ has zeros at all nodes except the considered node at which the adjoint excitation is unity as shown in Fig. 4.1.

$$\frac{\partial A_{z,m}}{\partial \boldsymbol{A}_z} = [\mathbf{0}^T \quad 1 \quad \mathbf{0}^T]^T \tag{4.10}$$

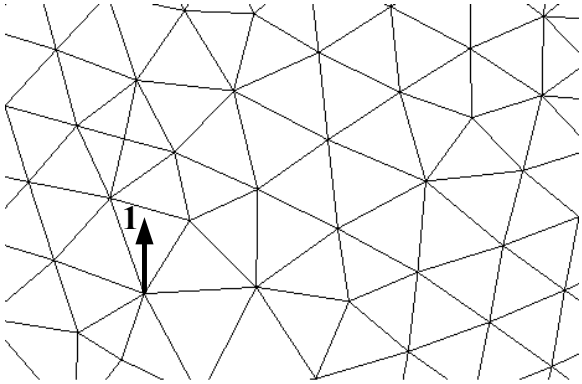

Fig. 4.1. The adjoint excitation for calculating the sensitivity of the magnetic vector potential at a specific node.

4.3.2 Flux Density

The sensitivities of the *x* and y components of magnetic flux density for each element with respect to different design parameters are obtained in a similar way. The explicit derivatives of $B_x^{(e)}$ and $B_y^{(e)}$ are obtained by differentiating (2.73) and (2.74) with respect to design parameter p_i. The explicit parts of the sensitivities are given by:

$$\left(\frac{\partial B_x^{(e)}}{\partial p_i}\right)_{explicit} = \frac{1}{2}\frac{\partial\left(\frac{1}{S^{(e)}}[r_1 \quad r_2 \quad r_3]\right)}{\partial p_i}\boldsymbol{A}_z^{(e)}, \tag{4.11}$$

$$\left(\frac{\partial B_y^{(e)}}{\partial p_i}\right)_{explicit} = \frac{-1}{2}\frac{\partial\left(\frac{1}{S^{(e)}}[q_1 \quad q_2 \quad q_3]\right)}{\partial p_i}\boldsymbol{A}_z^{(e)}. \tag{4.12}$$

The excitation vectors for both cases $\partial B_x^{(e)} / \partial \boldsymbol{A}_z$ and $\partial B_y^{(e)} / \partial \boldsymbol{A}_z$ have zeros at all nodes except the three nodes of the e^{th} element. The adjoint excitations at these nodes are obtained by differentiating (2.73) and (2.74) with respect to $\boldsymbol{A}_z^{(e)}$ respectively.

$$\frac{\partial B_x^{(e)}}{\partial \boldsymbol{A}_z^{(e)}} = \frac{1}{2S^{(e)}}\begin{bmatrix} r_1 & r_2 & r_3 \end{bmatrix}^T, \tag{4.13}$$

$$\frac{\partial B_y^{(e)}}{\partial \boldsymbol{A}_z^{(e)}} = \frac{-1}{2S^{(e)}}\begin{bmatrix} q_1 & q_2 & q_3 \end{bmatrix}^T. \tag{4.14}$$

4.3.3 Air-region Energy

Following a similar approach, the sensitivities of the air region magnetic energy $f = W_{AR}$ with respect to different design parameters are obtained. The explicit derivative of the air region energy with respect to the i^{th} design parameter is obtained by summing up the explicit derivatives of all air region elements' energies as follows:

$$\left(\frac{\partial W_{AR}}{\partial p_i}\right)_{explicit} = \sum_{e=1}^{e=N_{e,AR}} \left(\frac{\partial W^{(e)}}{\partial p_i}\right)_{explicit}. \tag{4.15}$$

From eqn. (2.80), the explicit derivative $\left(\partial W^{(e)} / \partial p_i\right)_{explicit}$ is derived from

$$\left(\frac{\partial W^{(e)}}{\partial p_i}\right)_{explicit} = \frac{L}{2}\boldsymbol{A}_z^{(e)T}\frac{\partial \boldsymbol{K}^{(e)}}{\partial p_i}\boldsymbol{A}_z^{(e)}. \tag{4.16}$$

To evaluate the implicit derivative part, the vector $\partial W_{AR} / \partial \boldsymbol{A}_z$ is obtained by assembling $\partial W^{(e)} / \partial \boldsymbol{A}_z^{(e)}$ for the nodes shared by the air region elements. The elemental energy derivatives $\partial W^{(e)} / \partial \boldsymbol{A}_z^{(e)}$ are obtained by differentiating (2.80) with respect to $\boldsymbol{A}_z^{(e)}$ to get:

$$\frac{\partial W^{(e)}}{\partial \boldsymbol{A}_z^{(e)}} = \frac{L}{2}\left(\boldsymbol{K}^{(e)} + \boldsymbol{K}^{(e)T}\right)\boldsymbol{A}_z^{(e)}. \tag{4.17}$$

4.3.4 Electromagnetic Torque

The sensitivities of the electromagnetic torque $f = T$ with respect to all design

parameters are obtained using eqn. (4.1) or eqn. (4.5). The explicit derivative of torque versus a design parameter is obtained by summing explicit derivatives of torque contributions of the first layer of elements around the moving part, $\left(\partial T^{(e)} / \partial p_i\right)_{explicit}$. This is estimated by differentiating (2.83) with respect to p_i which results in:

$$\left(\frac{\partial T^{(e)}}{\partial p_i}\right)_{explicit} = -\frac{L}{2} \boldsymbol{A}_z^{(e)T} \frac{\partial}{\partial p_i}\left(\frac{\partial \boldsymbol{K}^{(e)}}{\partial \theta}\right) \boldsymbol{A}_z^{(e)}. \tag{4.18}$$

The term $\frac{\partial}{\partial p_i}\left(\frac{\partial \boldsymbol{K}^{(e)}}{\partial \theta}\right)$ is obtained using finite differences at the nominal magnetic vector potential $\bar{\boldsymbol{A}}_z$, so there is no need to repeat the simulation.

$$\frac{\partial}{\partial p_i}\left(\frac{\partial \boldsymbol{K}^{(e)}}{\partial \theta}\right) = \left.\frac{\boldsymbol{K}_\theta^{(e)}\left(p_i + \Delta p_i\right) - \boldsymbol{K}_\theta^{(e)}\left(p_i\right)}{\Delta p_i}\right|_{\boldsymbol{A}_z = \bar{\boldsymbol{A}}_z}, \tag{4.19}$$

where $\boldsymbol{K}_\theta^{(e)} = \frac{\partial \boldsymbol{K}^{(e)}}{\partial \theta}$.

The derivative $\partial \boldsymbol{K}^{(e)} / \partial \theta$ is obtained when the derivatives $\partial x_i / \partial \theta$ and $\partial y_i / \partial \theta$ are calculated for the i^{th} node of the e^{th} element as presented earlier in Chapter 2.

The vector $\partial T / \partial \boldsymbol{A}_z$ is obtained by assembling $\partial T^{(e)} / \partial \boldsymbol{A}_z^{(e)}$ at the nodes shared by the first layer of elements around the moving part (shown as white elements in Fig. 2.11). $\partial T^{(e)} / \partial \boldsymbol{A}_z^{(e)}$ is obtained by differentiating (2.83) with respect to $\boldsymbol{A}_z^{(e)}$.

$$\frac{\partial T^{(e)}}{\partial \boldsymbol{A}_z^{(e)}} = -\frac{L}{2}\left(\frac{\partial \boldsymbol{K}^{(e)}}{\partial \theta} + \left(\frac{\partial \boldsymbol{K}^{(e)}}{\partial \theta}\right)^T\right) \boldsymbol{A}_z^{(e)}. \tag{4.20}$$

While we focused in this work on the sensitivities of the torque, the sensitivities of other torque-related quantities can be estimated as a byproduct. For example, the torque ripple T_{ripple} may be obtained using [100]

$$T_{ripple} = \sqrt{\frac{1}{M}\sum_{k=1}^{M}\left(T_k - T_{avg}\right)^2}, \tag{4.21}$$

where T_k is the torque value at the rotor angle θ_k for k=1,……., M. M is the total number of simulated rotor positions and T_{avg} is the average torque. The sensitivities of the torque ripple with respect to different design parameters can thus be obtained utilizing the electromagnetic torque values and sensitivities at the corresponding rotor positions with the corresponding dynamic currents.

4.3.5 Flux Linkage

A similar approach applies to the flux linkage ψ. The explicit derivative of flux linkage with respect to design parameter p_i is obtained using finite differences at the nominal magnetic vector potential as follows

$$\left(\frac{\partial \psi}{\partial p_i}\right)_{explicit} = \left.\frac{\psi\left(p_i + \Delta p_i\right) - \psi\left(p_i\right)}{\Delta p_i}\right|_{\boldsymbol{A}_z = \bar{\boldsymbol{A}}_z}. \tag{4.22}$$

The flux-linkage excitation vector is obtained from

$$\frac{\partial \psi}{\partial \boldsymbol{A}_z} = 2p\left[\frac{\partial \psi_{S_1}}{\partial \boldsymbol{A}_z} - \frac{\partial \psi_{S_2}}{\partial \boldsymbol{A}_z}\right], \tag{4.23}$$

where $\partial\psi_{S_1} / \partial \boldsymbol{A}_z$ and $\partial\psi_{S_2} / \partial \boldsymbol{A}_z$ are obtained by assembling $\partial\psi^{(e)} / \partial \boldsymbol{A}_z^{(e)}$ at the nodes shared by elements of the winding areas S_1 and S_2, shown in Fig. (2.10), respectively. The flux linkage contribution of the e^{th} element $\psi^{(e)}$ is obtained from

$$\psi^{(e)} = \frac{N_c L}{S} A_{z,avg}^{(e)} S^{(e)}, \tag{4.24}$$

where $S = S_1 = S_2$. The derivative $\partial\psi^{(e)} / \partial \boldsymbol{A}_z^{(e)}$ is obtained by differentiating (4.24) with respect to $\boldsymbol{A}_z^{(e)}$ to yield:

$$\frac{\partial \psi^{(e)}}{\partial \boldsymbol{A}_z^{(e)}} = \frac{N_c L}{S} \begin{bmatrix} \frac{S^{(e)}}{3} \\ \frac{S^{(e)}}{3} \\ \frac{S^{(e)}}{3} \end{bmatrix}. \tag{4.25}$$

4.4 Practical Implementation

A built-in MATLAB toolbox is used to calculate different responses of the SRM and their sensitivities with respect to the various geometric and physical design parameters. The stiffness matrix and the forcing vector required for adjoint sensitivity calculations have been calculated in our toolbox. The mesh exported from JMAG software [101] is utilized to build these matrices. The toolbox extracts the mesh data from JMAG. The mesh data includes the indices of the whole elements within the motor domain and the corresponding nodes in addition to the x and y coordinates of all domain nodes. Moreover, the data defines the elements of the motor different subdomains. This facilitates setting the materials inside the elements.

The mesh data and the material properties of the different parts of the motor are then used to recreate the stiffness matrix and the forcing vector for all elements within the domain. These local matrices and vectors are then assembled to obtain the global stiffness

matrix and forcing vector, respectively. The toolbox applies Dirichlet boundary conditions to the matrices. These matrices may have large dimensions for practical structures. This is addressed by using a compressed sparse column format. The toolbox then calculates the magnetic vector potential values at all domain nodes. Post processing is then applied to calculate different electromagnetic quantities of SRMs.

This procedure is applied at each rotor rotation step for a complete electrical cycle. The rotor is rotated keeping the same mesh as follows.

The airgap is divided by a center arc, named sliding arc, into two sections as shown in Fig. 4.2. One section is adjacent to the stator whereas the other one is adjacent to the rotor. The nodes on the sliding arc are called sliding nodes, and the angle between two consecutive nodes is the sliding angle. The sliding elements are the elements on the rotor side which have sliding nodes.

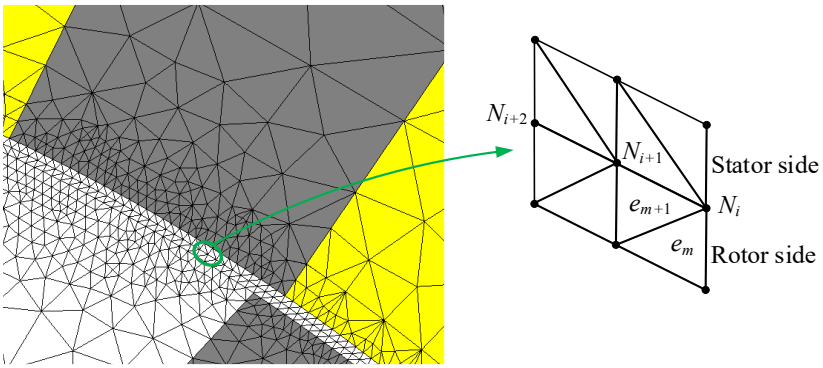

Fig. 4.2. Rotor rotation.

The rotor is rotated by rotating the azimuthal positions of all the nodes on the rotor side keeping their radial positions the same. The sliding nodes are kept fixed. For each sliding element, its sliding nodes' indices will be shifted by I_{shift} which equals

$$I_{shift} = \frac{\text{Rotation angle}}{\text{Sliding angle}} \tag{4.26}$$

The rotation angle equals either the sliding angle or its multiples.

As an example, if the rotor is to be rotated by one sliding angle, then beside rotating all the nodes on the rotor side, the sliding node of the sliding element e_m, shown in Fig. 4.2, will be changed from N_i to N_{i+1} whereas the sliding nodes of the element e_{m+1} will be changed from N_i and N_{i+1} to N_{i+1} and N_{i+2} and so on.

The toolbox calculates the sensitivities of the x and y components of the flux density at any location within the domain with respect to all parameters. It also calculates the sensitivities of the air-region energy, phase flux linkage, and electromagnetic torque of the SRM. This is achieved using the previously presented procedures in Subsections 4.1, 4.2, and 4.3 for linear and nonlinear cases. It should be noted that it is not necessary to rebuild the forcing vector after perturbing the design parameters to estimate the derivative. Alternatively, this vector derivative is zero at all nodes except the perturbed nodes. The same applies in calculating the stiffness matrix derivative which can be obtained by assembling only the perturbed elements. The sensitivities of any objective function may be estimated using this procedure.

4.5 Results

To illustrate the application of adjoint sensitivity analysis to SRMs, we estimate adjoint sensitivities of different electromagnetic quantities of an SRM and compare our AVM sensitivities to those calculated using the accurate but time-intensive CFD.

First, the motor static characteristics in case of linear and nonlinear materials are investigated.

Then, the dynamic characteristics are studied in the case of utilizing nonlinear magnetic materials. The parameters of the considered SRM are presented in Table 4.1.

Table 4.1
Parameters of the considered SRM.

Parameter	Symbol	Value
Stack length [mm]	L	74.00
Stator outer diameter [mm]	$D_{o,s}$	139.21
Stator teeth height [mm]	h_s	10
Stator teeth arc angle [°]	β_s	9.5
Stator teeth taper angle [°]	θ_s	4
Rotor teeth height [mm]	h_r	7.08
Rotor teeth arc angle [°]	β_r	9.3
Rotor teeth taper angle [°]	θ_r	4
Stator yoke thickness [mm]	y_s	10
Rotor yoke thickness [mm]	y_r	35.78
Rotor inner diameter [mm]	$D_{i,r}$	12.70
Airgap length [mm]	L_g	0.40
Number of turns per phase [turn]	N	230

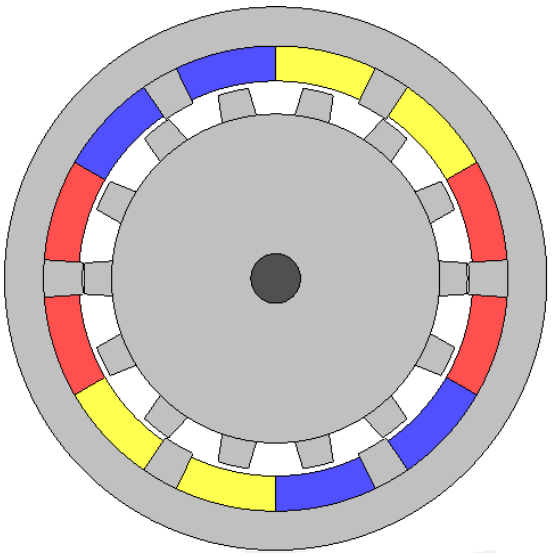

Fig. 4.3 JMAG 2D model of the considered motor.

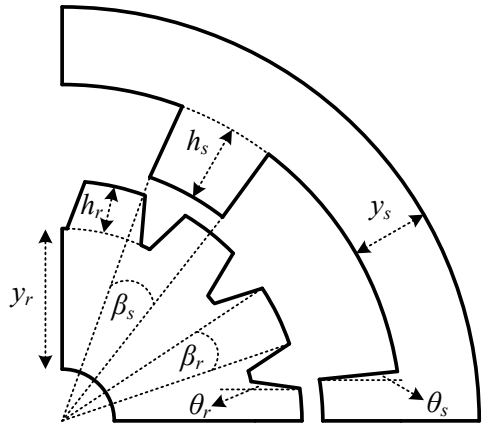

Fig. 4.4 Geometric design parameters of the considered motor.

The considered SRM has a 6/14 configuration. The JMAG model of the motor is shown in Fig. 4.3. Fig. 4.4 shows one-quarter section of the considered motor including the geometric design parameters.

The design parameters are the stator teeth height h_s, the rotor teeth height h_r, the stator yoke thickness y_s, the rotor yoke thickness y_r, the stator pole arc angle β_s, the rotor pole arc angle β_r, the stator taper angle θ_s, and the rotor taper angle θ_r. Table 4.2 presents the utilized materials in different motor parts.

Table 4.2
Materials utilized in the JMAG model

Part	Material
Stator	NO30-1600 (Nonlinear)
Rotor	NO30-1600 (Nonlinear)
Winding	Copper
Shaft	S45C

4.5.1 Static Characteristics of SRMs

The motor electromagnetic characteristics are calculated when only phase A is energized. Linear and nonlinear materials of stator and rotor will be taken into

consideration.

4.5.1.1 Linear Case

We consider estimating the sensitivities of the air region magnetic energy and electromagnetic torque versus the parameters $\boldsymbol{p} = [D_{o,s} \quad L_g \quad D_{i,r} \quad N]^T$. These sensitivities are estimated at different rotor positions as shown in Fig. 4.5, and at different phase excitation currents.

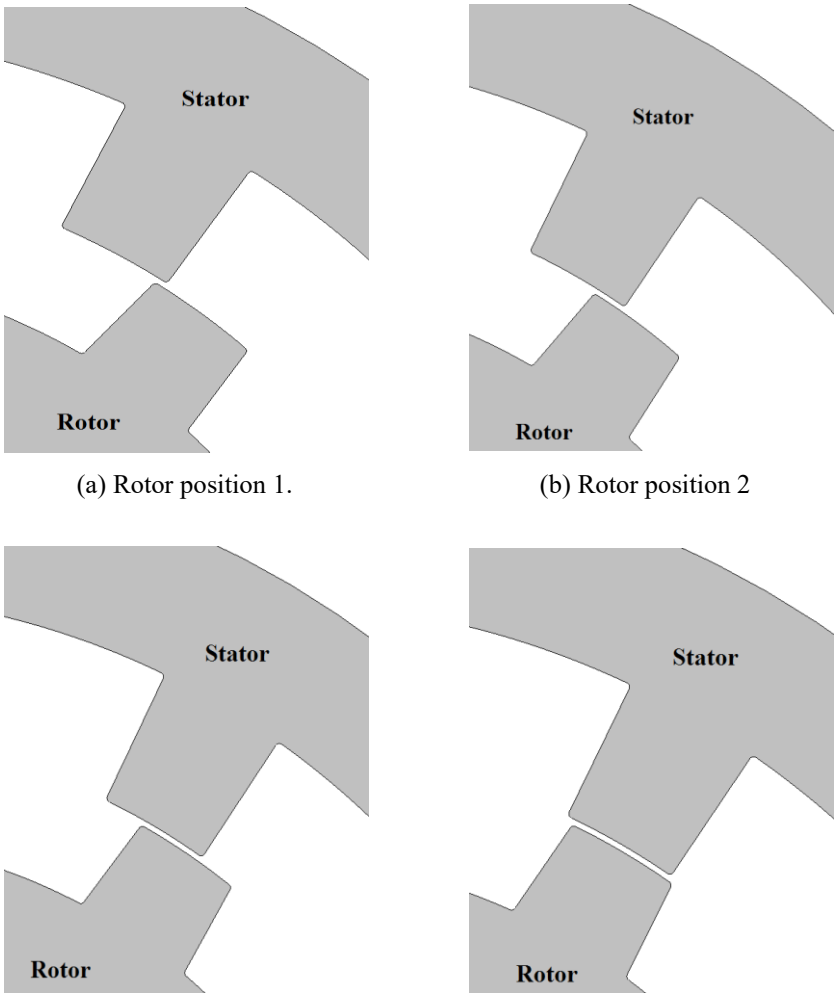

(a) Rotor position 1. (b) Rotor position 2

(c) Rotor position 3. (d) Rotor position 4.

Fig. 4.5. The different rotor positions at which sensitivity analysis is investigated.

Since linear magnetic materials are used, there is only one original simulation at each rotor position, and the solution is scaled for different currents at this position. At each rotor position, there are four design parameters. The CFD requires eight extra simulations. The AVM, however, does not depend on the number of design parameters. It requires only two extra simulations since there are two objective functions. For the four rotor positions, the CFD requires 36 simulations while AVM uses only 12 simulations. The results are shown in Figs. 4.6 to 4.9. All results show an excellent match between AVM sensitivities and those obtained using CFD. The absolute relative errors between various AVM and CFD sensitivities are presented in Table 4.3. The Table shows that the maximum relative error is below 0.8%.

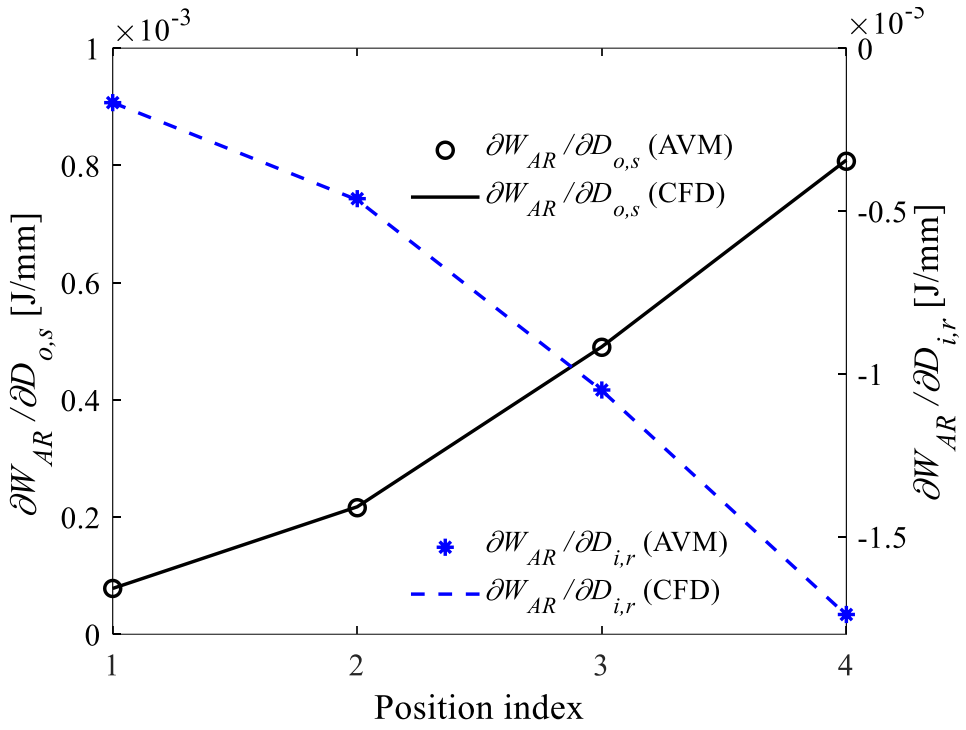

Fig. 4.6. The sensitivities of air region magnetic energy W_{AR} with respect to stator outer diameter $D_{o,s}$ and rotor inner diameter $D_{i,r}$ at a 3A excitation current for different rotor positions.

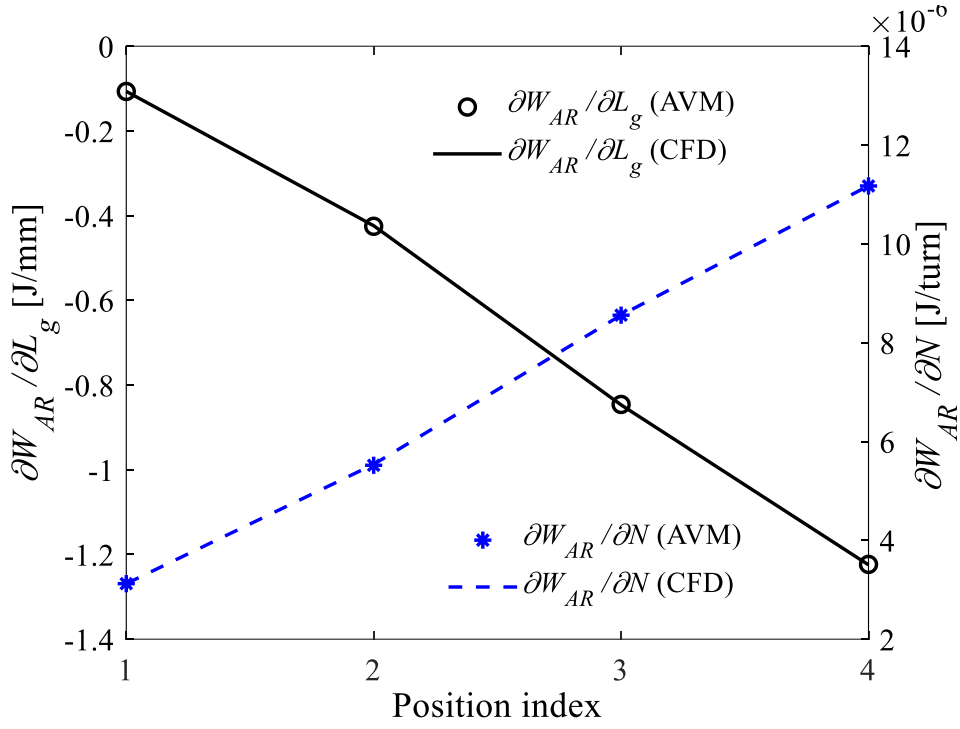

Fig. 4.7. The sensitivities of air region magnetic energy W_{AR} with respect to airgap length L_g and number of phase turns N at a 5A excitation current for different rotor positions.

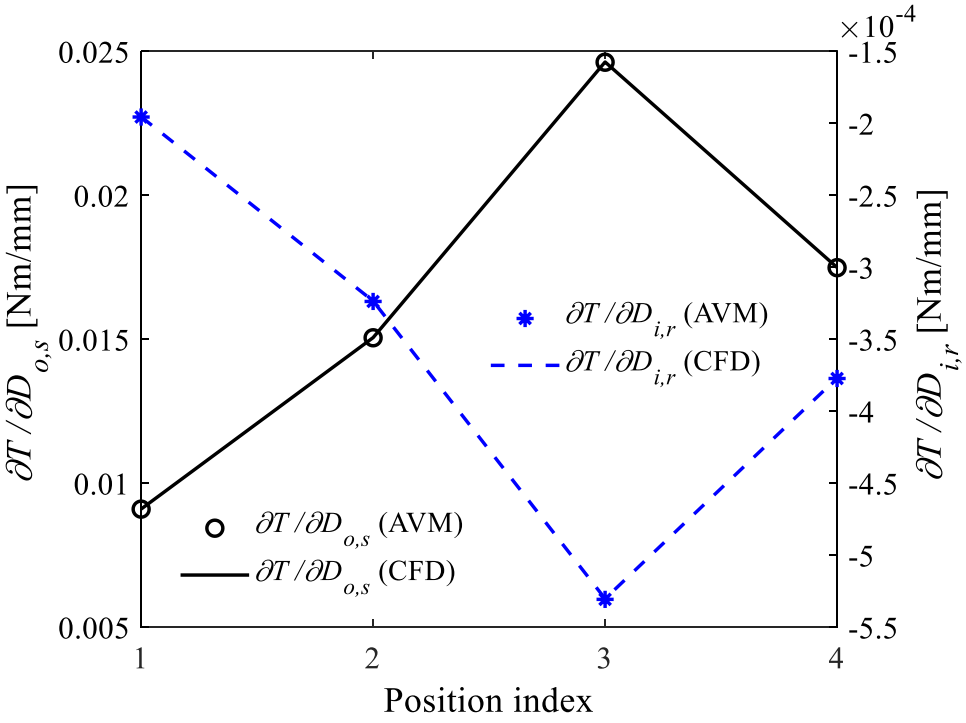

Fig. 4.8. The sensitivities of the electromagnetic torque T with respect to stator outer diameter $D_{o,s}$ and rotor inner diameter $D_{i,r}$ at an 8A excitation current for different rotor positions.

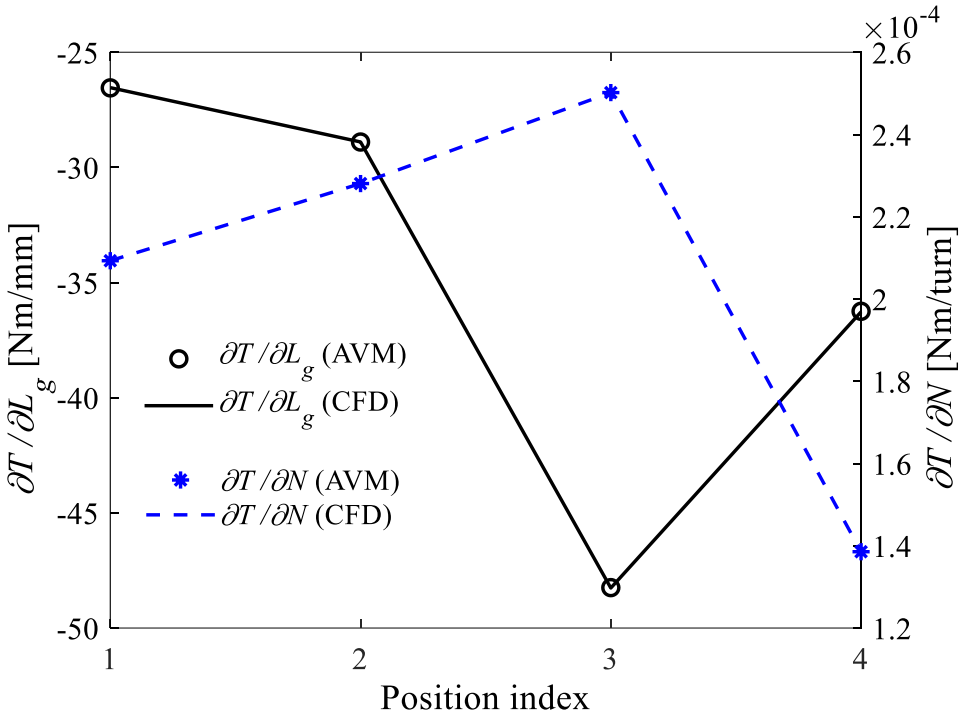

Fig. 4.9. The sensitivities of the electromagnetic torque T with respect to airgap length L_g and number of phase turns N at a 10A excitation current for different rotor positions.

Table 4.3
The absolute relative error between AVM and CFD sensitivities (gradients).

Gradient / Position	$\frac{\partial W_{AR}}{\partial D_{o,s}}$ at 3A	$\frac{\partial W_{AR}}{\partial D_{i,r}}$ at 3A	$\frac{\partial T}{\partial L_g}$ at 10A	$\frac{\partial T}{\partial N}$ at 10A
1	0.03 %	0.09 %	0.04 %	0.00 %
2	0.74 %	0.78 %	0.01 %	0.00 %
3	0.18 %	0.16 %	0.04 %	0.00 %
4	0.24 %	0.10 %	0.06 %	0.00 %

4.5.1.2 Nonlinear Case

Adjoint sensitivity analysis of electromagnetic quantities of the considered SRM, with nonlinear magnetic material, is investigated using AVM and CFD. Sensitivities of the x and y components of the flux density at a stator tooth tip, phase flux linkage, and electromagnetic torque of the SRM with respect to different design parameters are calculated throughout a complete electrical cycle at a current of 10A. The design

parameters are the stator teeth height h_s, the rotor teeth height h_r, the stator yoke thickness y_s, the rotor yoke thickness y_r, the stator pole arc angle β_s, the rotor pole arc angle β_r, the stator taper angle θ_s, and the rotor taper angle θ_r. The results are shown in Figs. 4.10 to 4.17. All results show an excellent match between AVM sensitivities and those obtained using CFD.

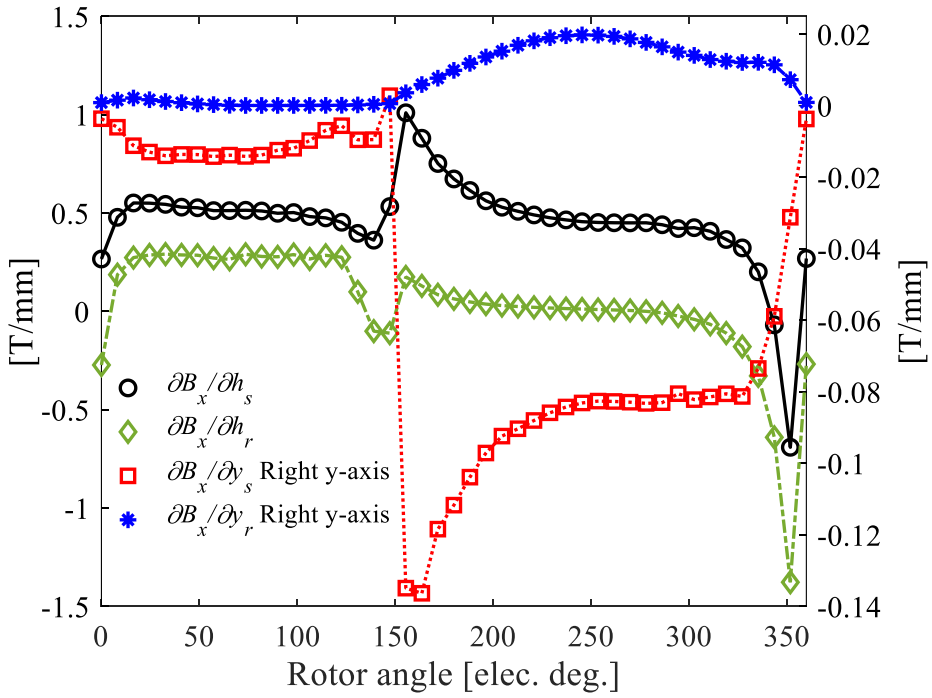

Fig. 4.10. The sensitivity of B_x at a stator tooth tip with respect to h_s, h_r, y_s, and y_r for a complete electrical cycle. The marker shows the AVM derivative while the line shows the corresponding CFD sensitivity.

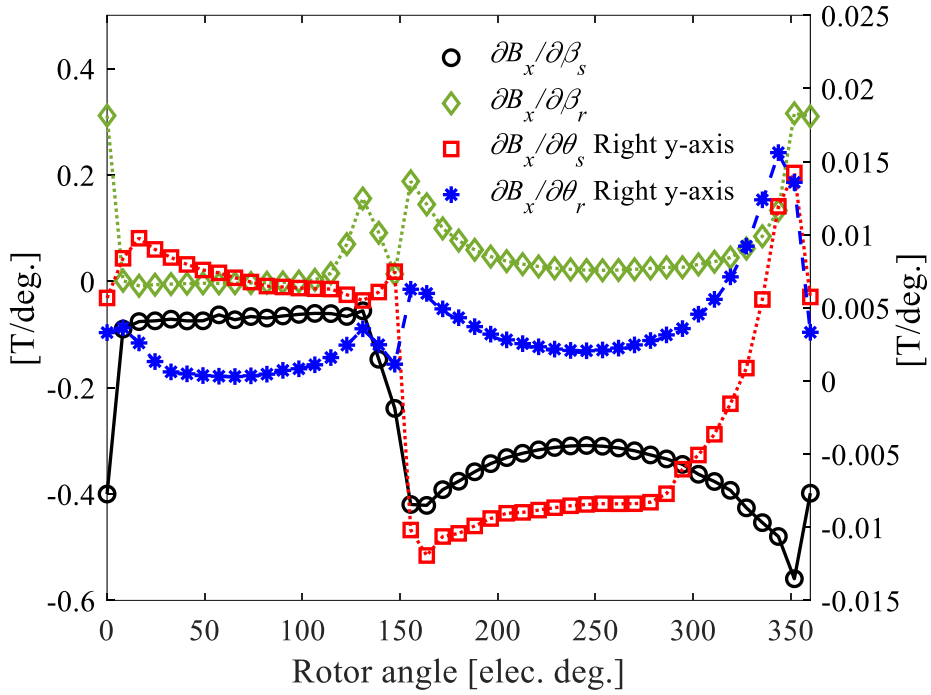

Fig. 4.11. The sensitivity of B_x at a stator tooth tip with respect to β_s, β_r, θ_s, and θ_r for a complete electrical cycle. The marker shows the AVM derivative while the line shows the corresponding CFD sensitivity.

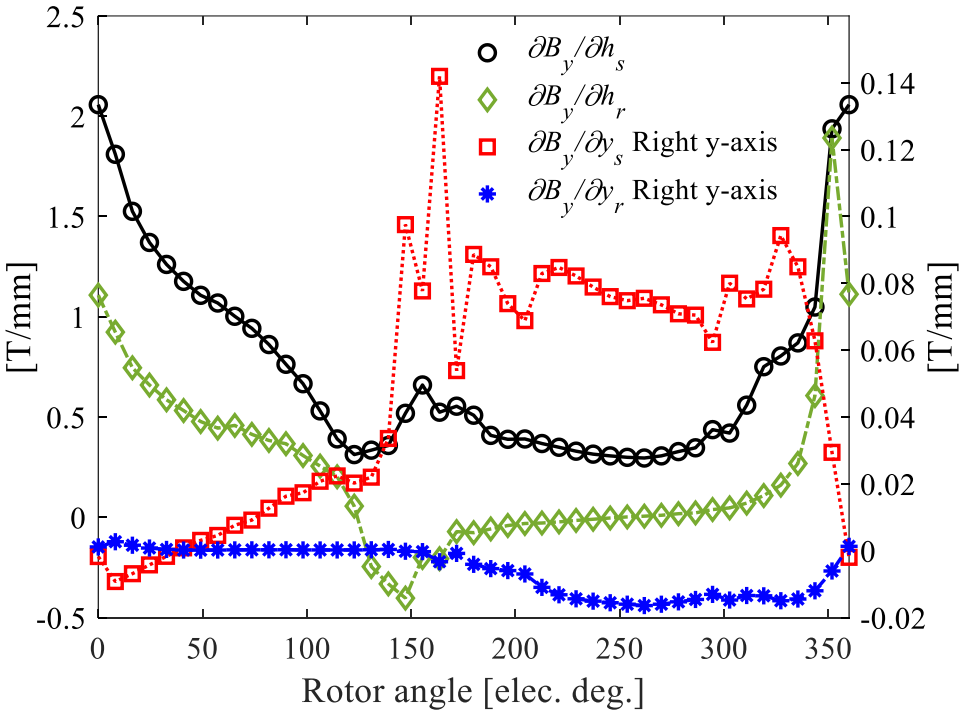

Fig. 4.12. The sensitivity of B_y at a stator tooth tip with respect to h_s, h_r, y_s, and y_r for a complete electrical cycle. The marker shows the AVM derivative while the line shows the corresponding CFD sensitivity.

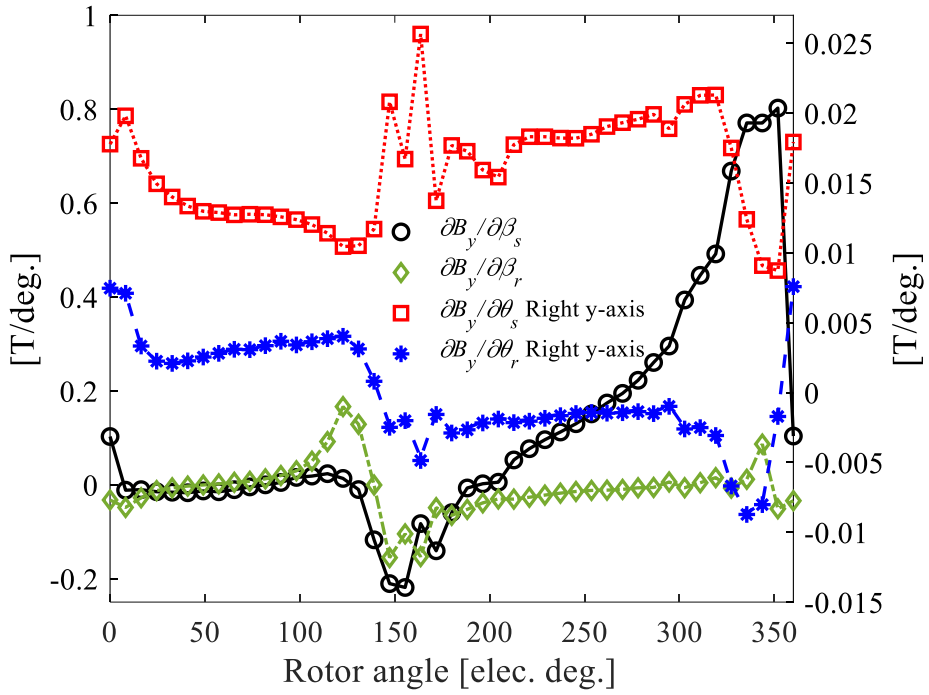

Fig. 4.13. The sensitivity of B_y at a stator tooth tip with respect to β_s, β_r, θ_s, and θ_r for a complete electrical cycle. The marker shows the AVM derivative while the line shows the corresponding CFD sensitivity.

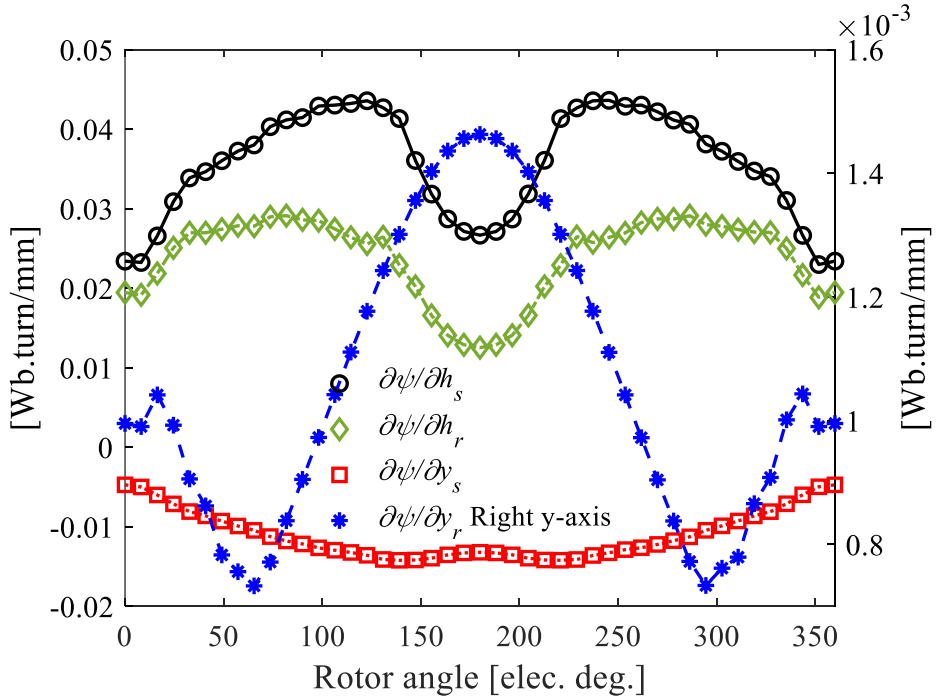

Fig. 4.14. The sensitivity of ψ with respect to h_s, h_r, y_s, and y_r for a complete electrical cycle. The marker shows the AVM derivative while the line shows the corresponding CFD sensitivity.

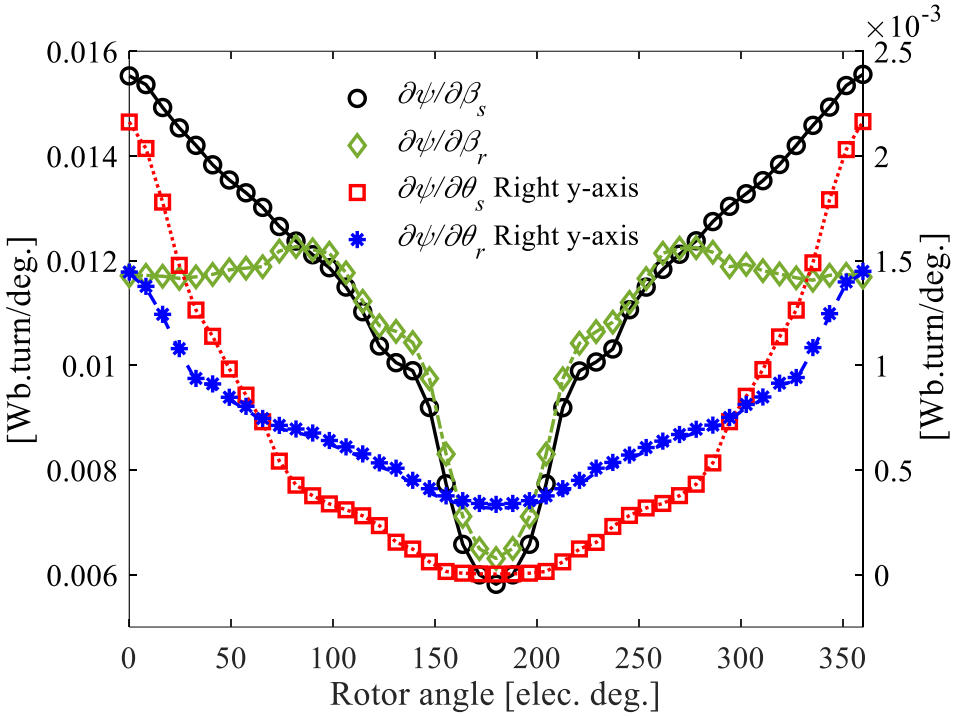

Fig. 4.15. The sensitivity of ψ with respect to β_s, β_r, θ_s, and θ_r for a complete electrical cycle. The marker shows the AVM derivative while the line shows the corresponding CFD sensitivity.

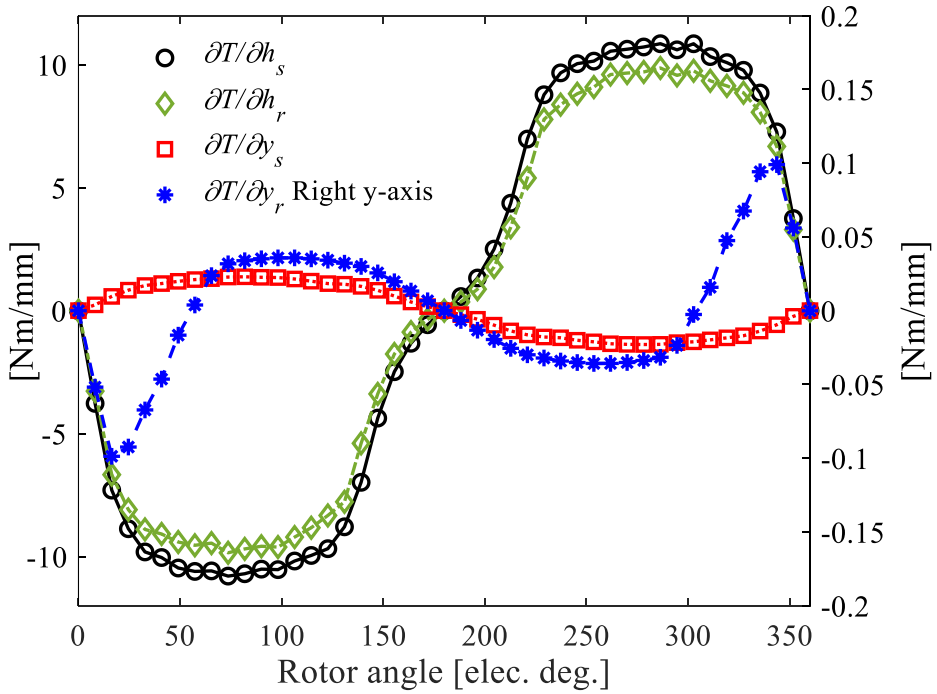

Fig. 4.16. The sensitivity of the electromagnetic torque T with respect to h_s, h_r, y_s, and y_r for a complete electrical cycle. The marker shows the AVM derivative while the line shows the corresponding CFD sensitivity.

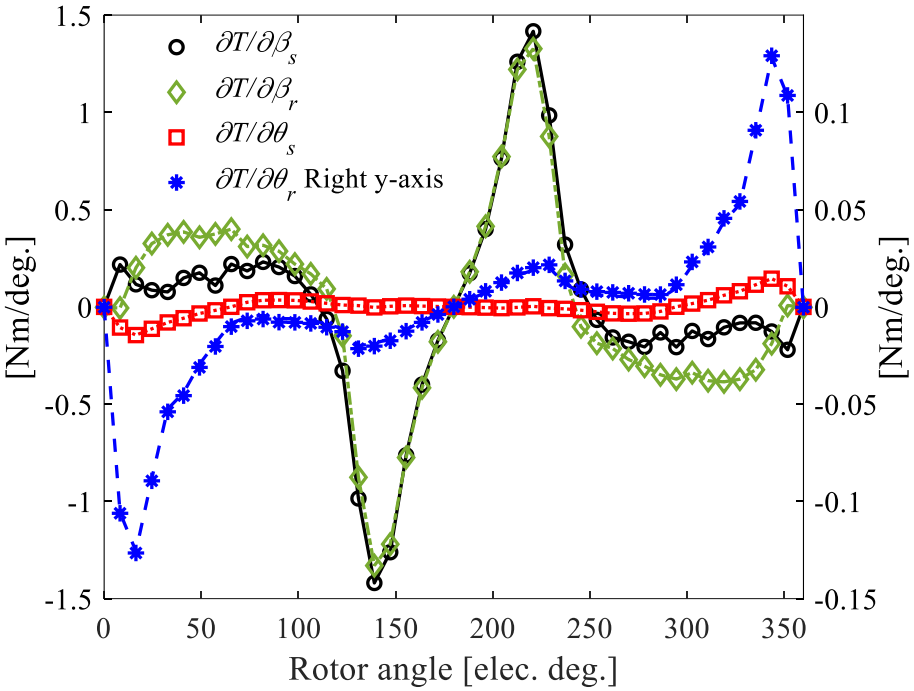

Fig. 4.17. The sensitivity of the electromagnetic torque T with respect β_s, β_r, θ_s, and θ_r for a complete electrical cycle. The marker shows the AVM derivative while the line shows the corresponding CFD sensitivity.

4.5.2 Dynamic Characteristics of SRMs

Sensitivities of the x and y components of flux density, phase flux linkage, and electromagnetic torque of the SRM with respect to different design parameters are calculated at four different rotor positions, 1.74, 8.7, 11 and 16.81 mech. deg., with the corresponding excitation dynamic currents. The dynamic currents are obtained using the nonlinear dynamic model presented in Section 2.2.2.

The design parameters are airgap length, stator pole shaping, rotor pole shaping, stator yoke thickness, and the number of turns per phase. Stator and rotor pole shaping are obtained by perturbing five nodes at the interface between each of them and the airgap. These nodes are shown in Figs. 4.18 (a) and (b), respectively.

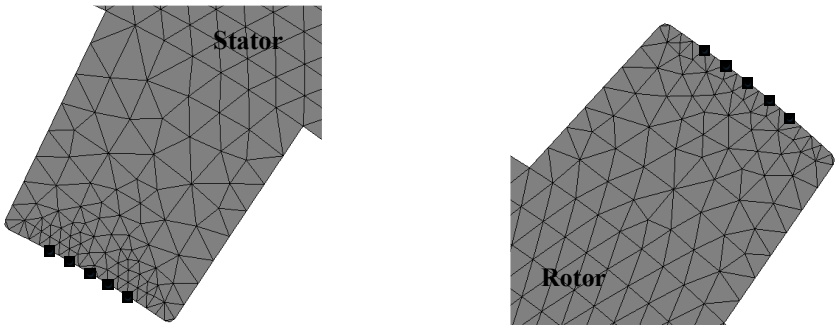

(a) The perturbed nodes of the stator pole. (b) The perturbed nodes of the rotor pole.

Fig. 4.18. The perturbed nodes of the stator and rotor poles.

At each rotor position, there are five design parameters, so CFD needs ten extra iterative simulations. On the other hand, AVM does not depend on the number of design parameters, and it requires only one extra direct (not-iterative [99]) simulation for each objective function. For the four rotor positions, CFD needs 44 iterative simulations while AVM uses only four iterative and four direct simulations. The results are shown in Figs. 4.19 to 4.25. All results show an excellent match between AVM and CFD sensitivities.

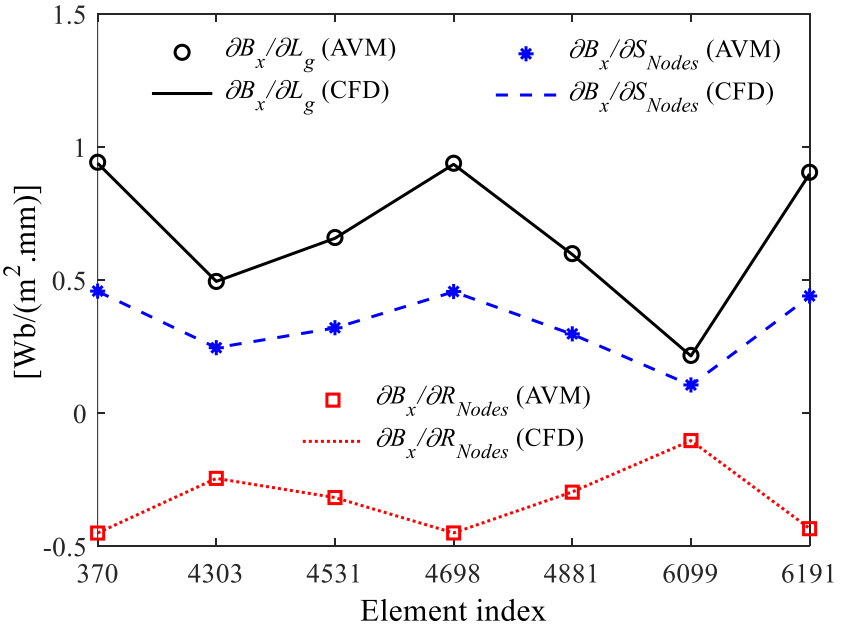

Fig. 4.19. The sensitivity of the x component of the flux density B_x at different elements with respect to the airgap length L_g, the stator pole shaping nodes S_{Nodes}, and the rotor pole shaping nodes R_{Nodes} at rotor position 1.

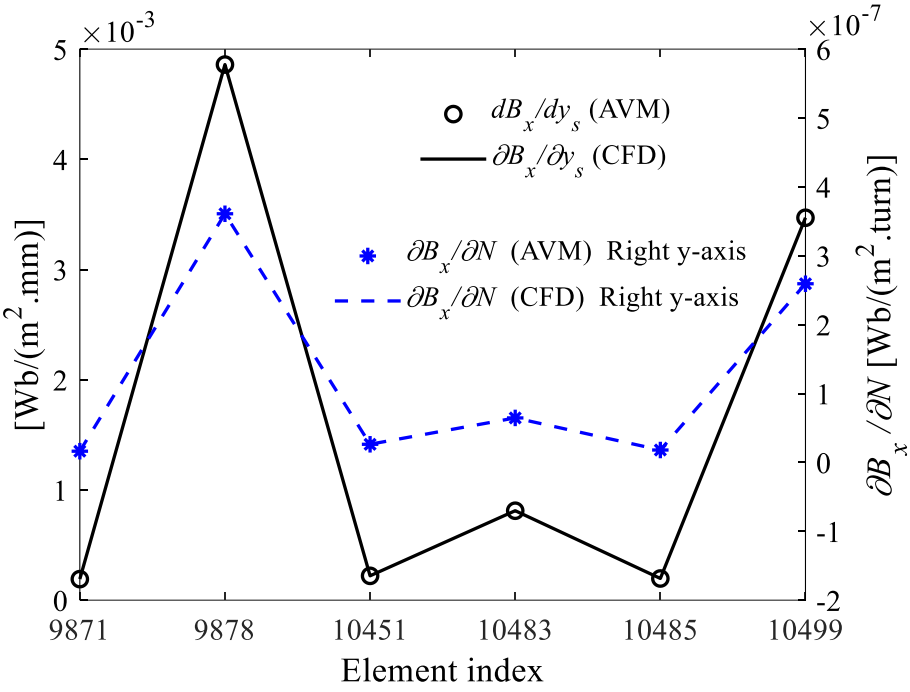

Fig. 4.20. The sensitivity of the x component of the flux density B_x at different elements with respect to the stator yoke thickness y_s and the number of turns per phase N at rotor position 2.

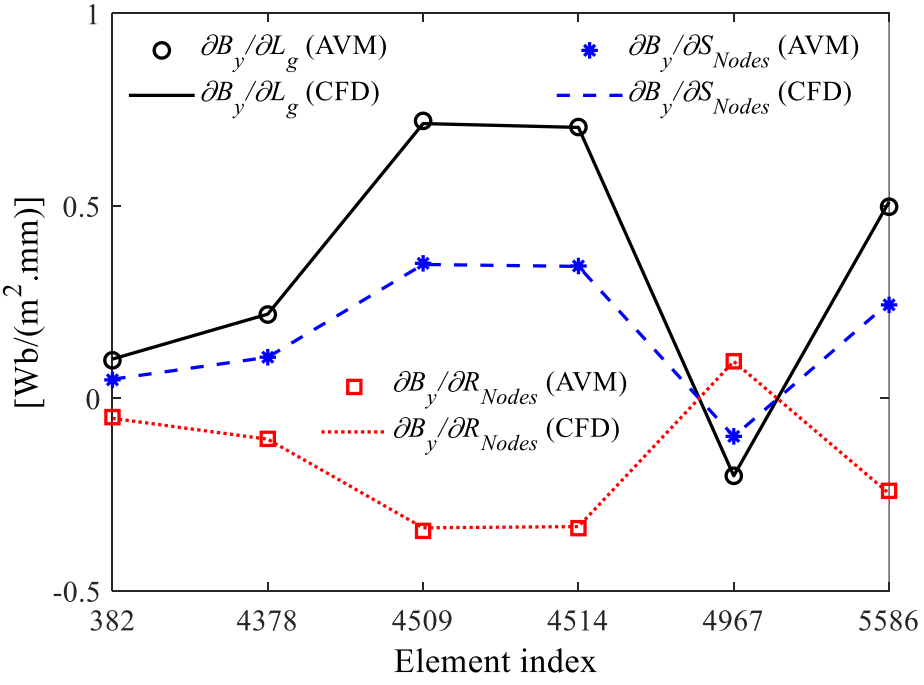

Fig. 4.21. The sensitivity of the y component of the flux density B_y at different elements with respect to the airgap length L_g, the stator pole shaping nodes S_{Nodes}, and the rotor pole shaping nodes R_{Nodes} at rotor position 3.

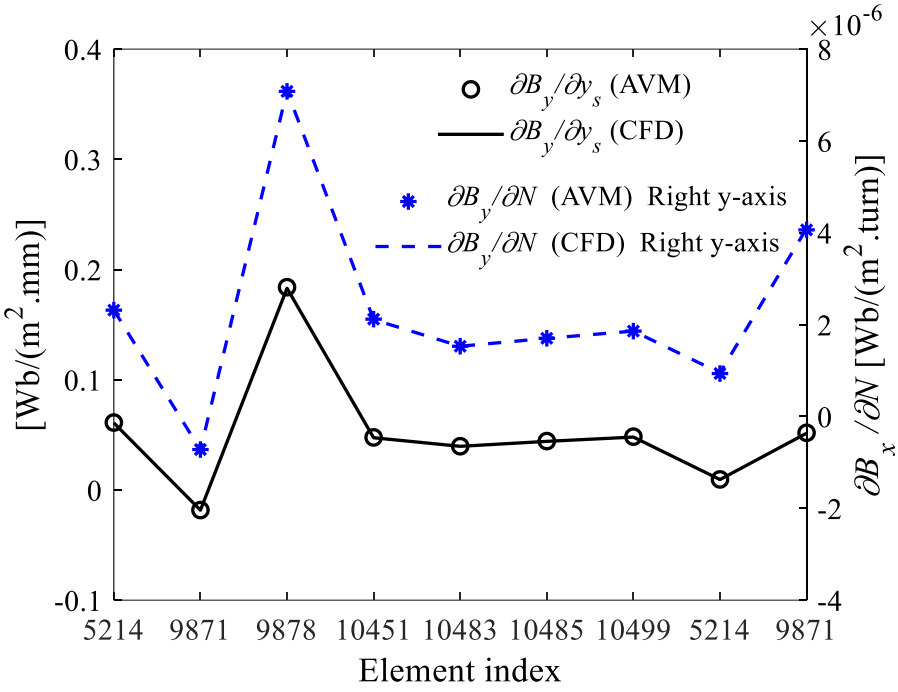

Fig. 4.22. The sensitivity of the y component of the flux density B_y at different elements with respect to the stator yoke thickness y_s and the number of turns per phase N at rotor position 4.

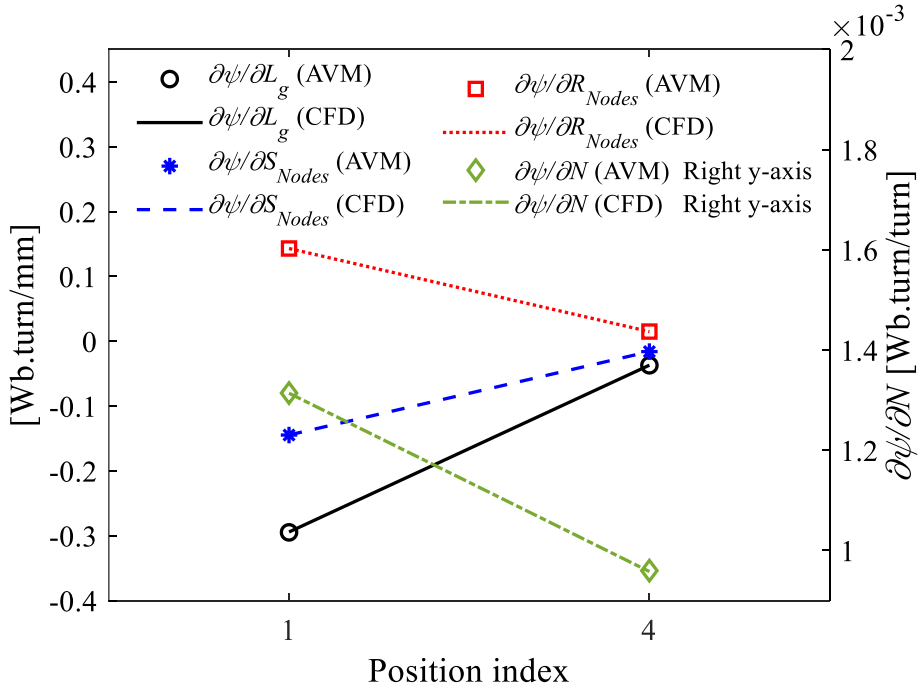

Fig. 4.23. The sensitivity of the phase flux linkage ψ with respect to the airgap length L_g, the stator pole shaping nodes S_{Nodes}, the rotor pole shaping nodes R_{Nodes}, and the number of phase turns N at rotor positions 1 and 4.

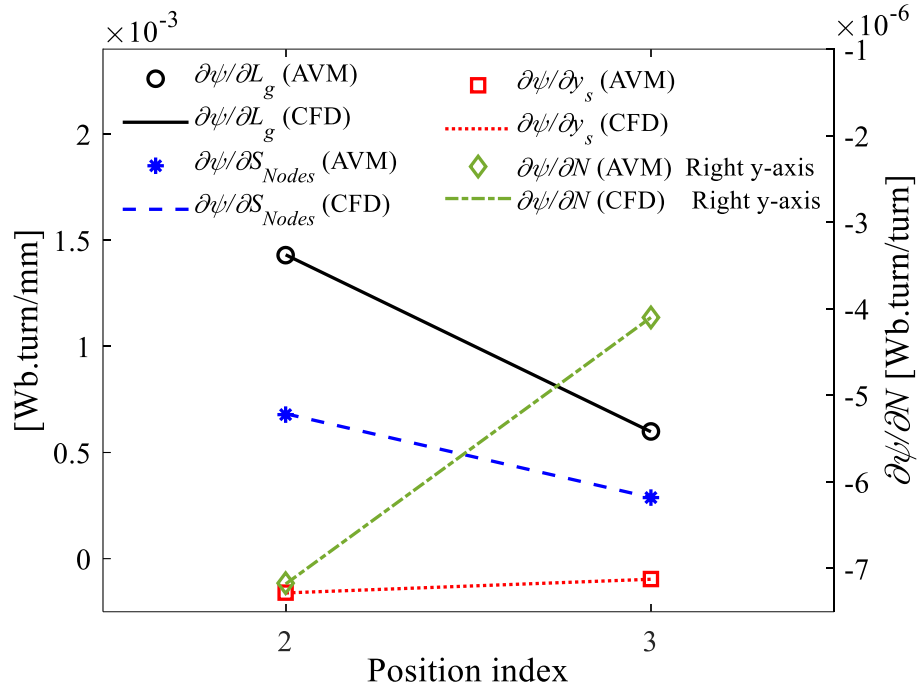

Fig. 4.24. The sensitivity of phase flux linkage ψ with respect to the airgap length L_g, the stator pole shaping nodes S_{Nodes}, the stator yoke thickness y_s, and the phase turns N at rotor positions 2 and 3.

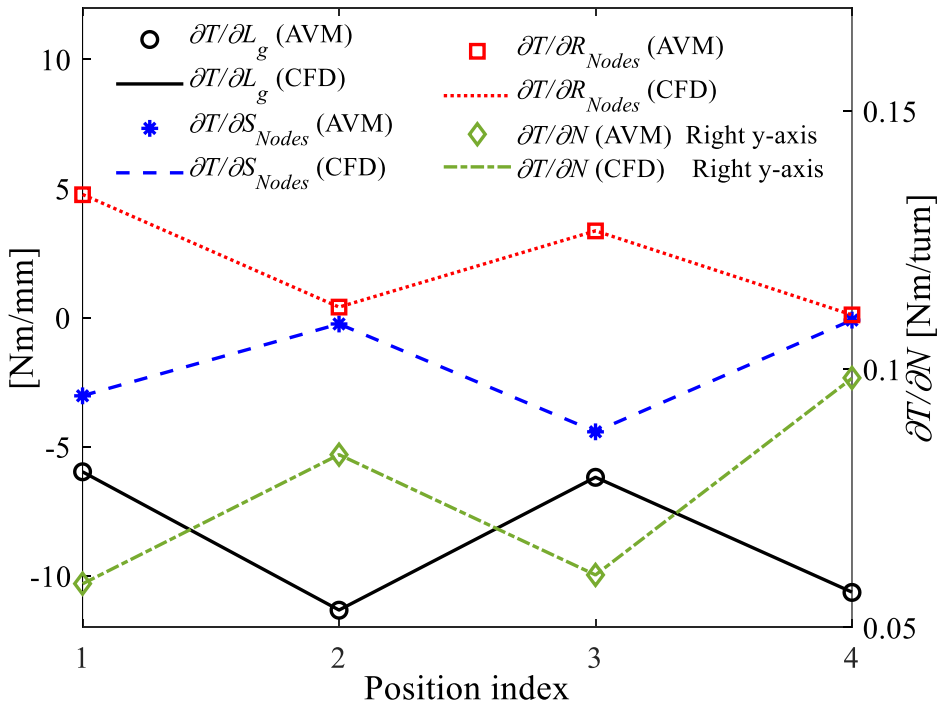

Fig. 4.25. The sensitivity of electromagnetic torque with respect to the airgap length L_g, the stator pole shaping nodes S_{Nodes}, the rotor pole shaping nodes R_{Nodes}, and the number of phase turns N at the four rotor positions.

This page is intentionally left blank

Chapter 5

Adjoint-based Geometric Optimization of Nonlinear SRMs

5.1 Introduction

As presented in Chapter 4, we utilize the AVM method to calculate the sensitivities of different static or dynamic electromagnetic quantities of SRMs with respect to different geometric design parameters such as teeth height, yoke thickness, pole arc angle, and taper angle of both stator and rotor. These sensitivities may be utilized in deterministic optimization of the motor geometry to achieve different objective functions. In this chapter, two optimization cases are considered. An interior-point optimization method is used to optimize the geometry of a nonlinear SRM using the obtained torque sensitivities to maximize the motor static torque profile. Moreover, the dynamic torque sensitivities are utilized to maximize the motor dynamic torque. The initial designs are different in both cases. A structural mapping technique is used to parametrize the motor geometry through the optimization process.

5.2 Structural Mapping

Structural mapping is used to parameterize the considered SRM geometry. An initial geometry is modified using the structural laws of elasticity [102-104]. The motor shape is modified by deforming, expanding and compressing, the motor mesh elements [102, 103]. This method guarantees to generate smooth shape boundaries depending on the applied forces or the nodal displacements and the material structural characteristics of stiffness and Poisson's ratio [102, 103].

A 2D plane stress analysis of the motor domain is performed using constant strain finite element due to its compatibility with the first order triangular element used for the electromagnetic field analysis [103]. Thus, the same motor mesh can be used for both structural and electromagnetic studies. The structural analysis is performed to control the geometric design parameters of the motor. In structural analysis, finite element equation is as follows [102-104]

$$\boldsymbol{M}\boldsymbol{d} = \boldsymbol{F}, \tag{5.1}$$

where $\boldsymbol{M}$ is the global structural stiffness matrix determined by the domain geometry in addition to the material properties such as modulus of elasticity E and Poisson's ratio g [102-104]. $\boldsymbol{d}$ is the vector of nodal displacements in the x and y directions, and $\boldsymbol{F}$ is the global structural forcing vector which represents the nodal forces in the two directions [102-104].

The structural model may be perturbed either by applying forces $\boldsymbol{F}$ as loads or by specifying nodal displacement components in the vector $\boldsymbol{d}$ [103].

The global stiffness matrix is obtained by assembling the local stiffness matrices of all domain elements. The element stiffness matrix $\boldsymbol{M}^{(e)} \in R^{dof \times dof}$, where dof is the number of degrees of freedom per element, is obtained using the following equation [105]

$$\boldsymbol{M}^{(e)} = S^{(e)}\boldsymbol{C}^{(e)T}\boldsymbol{D}^{(e)}\boldsymbol{C}^{(e)}, \tag{5.2}$$

where $\boldsymbol{C}^{(e)}$ is the e^{th} element gradient matrix which is obtained from [105]

$$\boldsymbol{C}^{(e)} = \frac{1}{2S^{(e)}}\begin{bmatrix} q_1 & 0 & q_2 & 0 & q_3 & 0 \\ 0 & r_1 & 0 & r_2 & 0 & r_3 \\ r_1 & q_1 & r_2 & q_2 & r_3 & q_3 \end{bmatrix}. \tag{5.3}$$

$\boldsymbol{D}^{(e)}$ is the constitutive matrix which is obtained, for plane-stress analysis, as follows [105]

$$\boldsymbol{D}^{(e)} = \frac{E}{\left(1-g^2\right)}\begin{bmatrix} 1 & g & 0 \\ g & 1 & 0 \\ 0 & 0 & (1-g)/2 \end{bmatrix} \tag{5.4}$$

After the assembly process, without applying any forces and with specific nodal displacements, eqn. (5.1) is used to calculate the movements of all remaining nodes within the domain [1-3]. Eqn. (5.1) is rewritten as follows in a partitioned form [102-104]

$$\begin{bmatrix} \boldsymbol{M}_{uu} & \boldsymbol{M}_{us} \\ \boldsymbol{M}_{su} & \boldsymbol{M}_{ss} \end{bmatrix}\begin{bmatrix} \boldsymbol{d}_u \\ \boldsymbol{d}_s \end{bmatrix} = \boldsymbol{0}, \tag{5.5}$$

where subscripts u and s refer to unknown and specified, respectively. d_u and d_s represent the unknown and specified nodal displacements, respectively.

The unknown displacements d_u are obtained by solving the first row of eqn. (5.5) as follows [102, 103]

$$\boldsymbol{M}_{uu}\boldsymbol{d}_u = -\boldsymbol{M}_{us}\boldsymbol{d}_s. \tag{5.6}$$

Each design parameter is controlled by predefined interface boundary nodes. The stator outer diameter is kept constant during the optimization process, so the x and y displacements of its control nodes, shown in red in Fig. 5.1, are assigned to zero. The same applies to any fixed non-optimizable parameter.

The stator yoke thickness, as an example of the optimizable parameters, is controlled by the green control nodes shown in Fig. 5.1. These control nodes move towards either the positive or the negative radial direction to decrease or increase the yoke thickness, respectively.

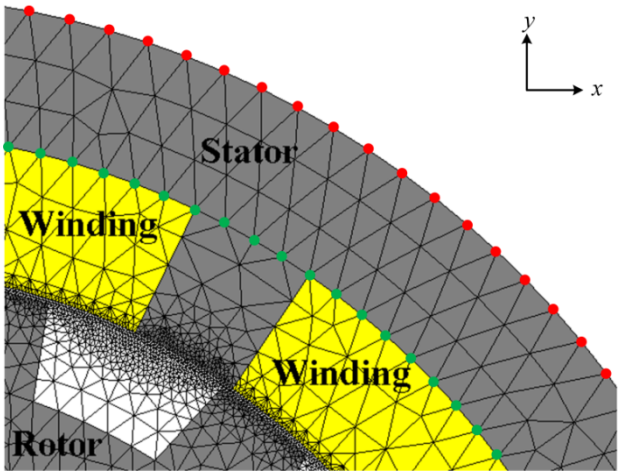

Fig. 5.1. A part of the considered SRM mesh.

Based on the values of the initial and modified yoke thicknesses, the value of the radial movement is obtained. Keeping the control nodes' azimuthal angles constant, the *x* and *y* displacements of these nodes are calculated. A similar procedure is followed to calculate the displacements of the control nodes of the rotor yoke thickness, stator teeth height, and rotor teeth height.

Any changes applied to the airgap mesh may introduce numerical errors and affect the solution accuracy, so the airgap mesh, shown in Fig. 4.2, moves as one part with relative fixation of all the included nodes.

Structural mapping approach is also applied to control the arc and taper angles of stator and rotor teeth. To reduce the deformation of elements while changing these angles, the material property of the mesh elements is changed as well. For instance, if the stator pole arc angle is required to be wider, the material property of some of the nearby elements in the surrounding winding areas, shown in Fig. 5.1, is changed from copper to stator electrical steel material. These elements are chosen according to the required stator pole arc angle and taper angle. The interface boundary between the modified pole and the

winding area is then smoothed using structural mapping. Keeping the radial positions of these boundary nodes constant, the nodes' azimuthal angles are changed to achieve the modified arc and taper angles. Based on the radial positions and the azimuthal angles' changes of the boundary nodes, the x and y displacements are calculated.

The specified displacements of the control nodes of the geometric design parameters are assigned to the vector $\boldsymbol{d}_s$ of Eqn. 5.6, and then utilized to obtain the unknown displacements $\boldsymbol{d}_u$ of the remaining nodes within the motor domain which move such that the mesh deformation is reduced.

Fig. 5.2 to Fig. 5.4 show examples of using structural mapping in the geometric parameterization of different parameters of the considered SRM. Fig. 5.2 shows the change in the stator yoke thickness of the considered SRM whereas Fig. 5.3 shows controlling the stator and rotor teeth height, and Fig. 5.4 shows changing pole arc angles and taper angles of stator and rotor teeth.

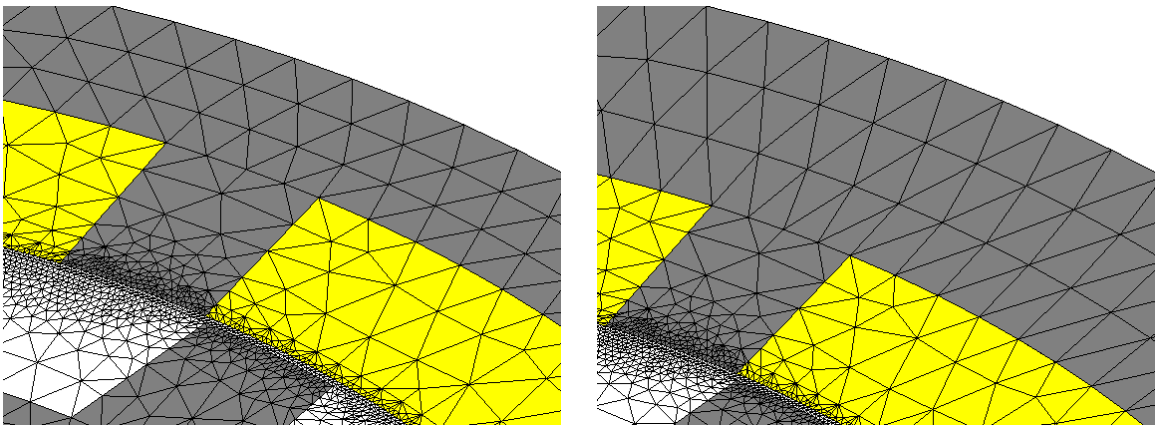

Fig. 5.2. Changing stator yoke thickness.

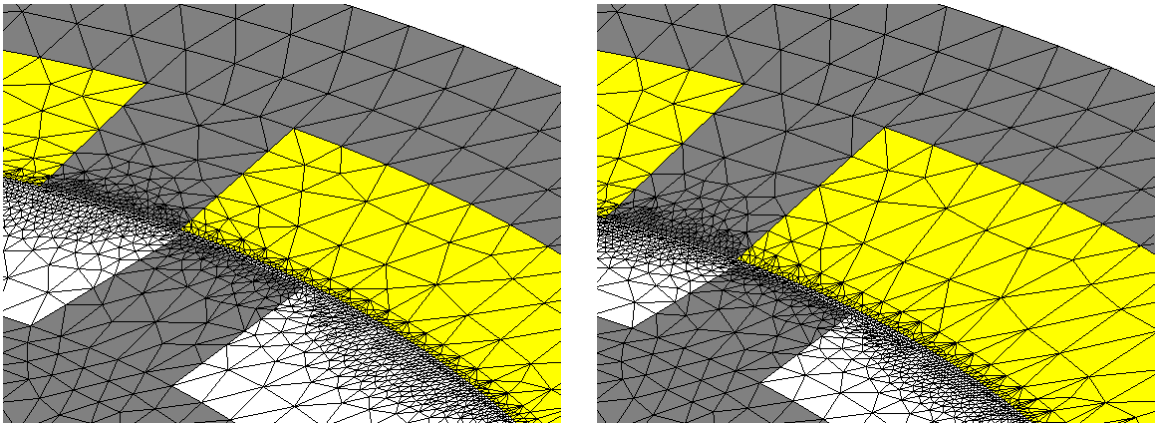

Fig. 5.3. Changing stator and rotor teeth height.

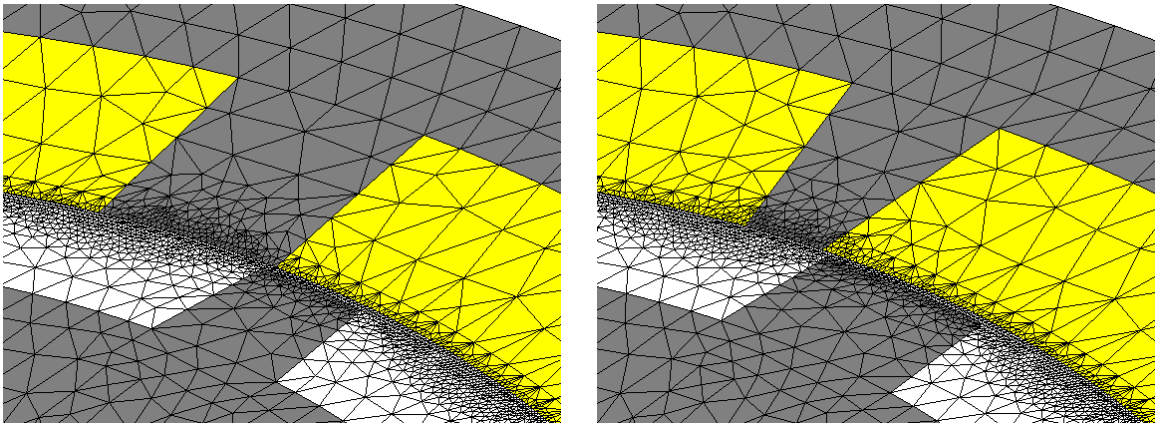

Fig. 5.4. Varying pole arc angles and taper angles of stator and rotor teeth.

5.3 Geometric Optimization (Static Characteristics)

An interior-point method [106] is used to optimize the geometry of the considered SRM to maximize its static torque profile at a certain current without violating the design constraints. This method utilizes the obtained sensitivities of the electromagnetic torque with respect to the design parameters. The motor geometric parameters are controlled through the optimization process by using structural mapping and by changing the material properties of mesh elements. The non-optimizable parameters of the considered motor are presented in Table 5.1.

Table 5.1
SRM non-optimizable parameters

Parameter	Value
Stack length	74.00 mm
Shaft diameter	12.70 mm
Stator outer diameter	139.21 mm
Airgap length	0.40 mm
Number of turns per phase	230 turn

The optimizable design parameters are $\boldsymbol{p} = [h_r \ y_s \ \ y_r \ \beta_s \ \beta_r \ \theta_s \ \theta_r]^T$. Since the motor's outer diameter and airgap length are kept constant, the stator's teeth height is obtained directly. The optimizer starts from initial design and proceeds to reach an optimized design without violating the given constraints. The target is to minimize the average value of the negative half cycle of the static torque profile T_{avg}.

The optimization problem is given by:

$$
\begin{aligned}
&\min_{\boldsymbol{p}} \ f = T_{avg} \\
&\textit{subject to} \\
&7 \text{ mm} \le h_r \le 9 \text{ mm}, \\
&10 \text{ mm} \le y_s \le 13 \text{ mm}, \\
&31 \text{ mm} \le y_r \le 37 \text{ mm}, \\
&h_r + y_s + y_r \le 56.855 \text{ mm}, \\
&ff_c \le 0.48, \\
&17.143° \le \beta_s + \beta_r \le 25.714°, \\
&5° \le \beta_s \le 12.6°, \\
&5° \le \beta_r \le 12°, \\
&0° \le \theta_s \le 7°, \\
&0° \le \theta_r \le 7°,
\end{aligned}
\tag{5.7}
$$

where ff_c is the bare copper fill factor inside the slot.

Through the optimization process, there are seven design parameters at each rotor angle. The CFD requires 14 extra iterative simulations. On the other hand, AVM does not depend on the number of design parameters. It needs only one extra direct (not-iterative) simulation. The optimization process starts from an initial design $\boldsymbol{p}$ = [7.5mm 11.0mm 32.0mm 8.92° 8.14º 1.0° 2.0°]^T and settles at another design with a higher absolute average value. The process is then reset by using this design as the initial one. The optimization process then terminates at the optimized design $\boldsymbol{p}$ = [7.0mm 10mm 34.92mm 11.24º 11.06° 2.92° 4.26°]^T. The initial and final JMAG models of the designs are shown in Figs. 5.5 and 5.6, respectively. The objective function values versus iteration number are shown in Fig. 5.7. The static torque profiles before and after optimization, including the validation with JMAG results, are shown in Fig. 5.8. A 33.52 % increase in the average value of the torque profile half cycle is achieved.

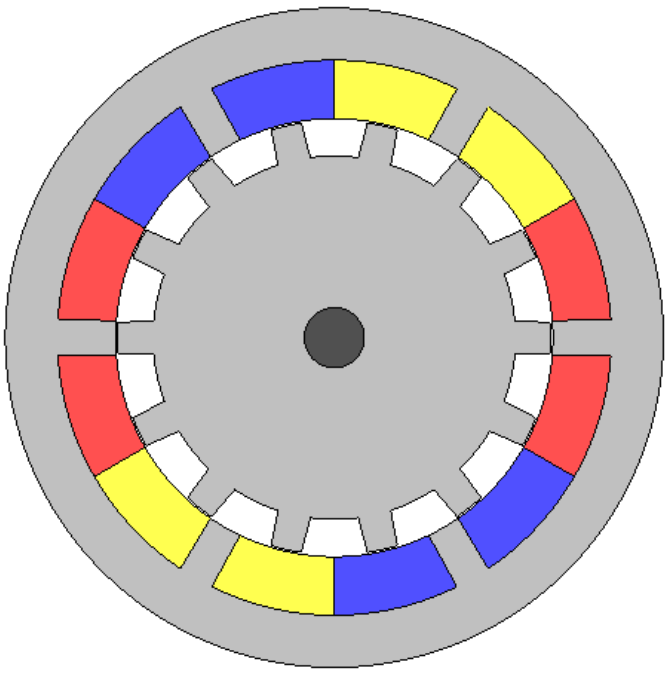

Fig. 5.5. The initial design of the optimization problem.

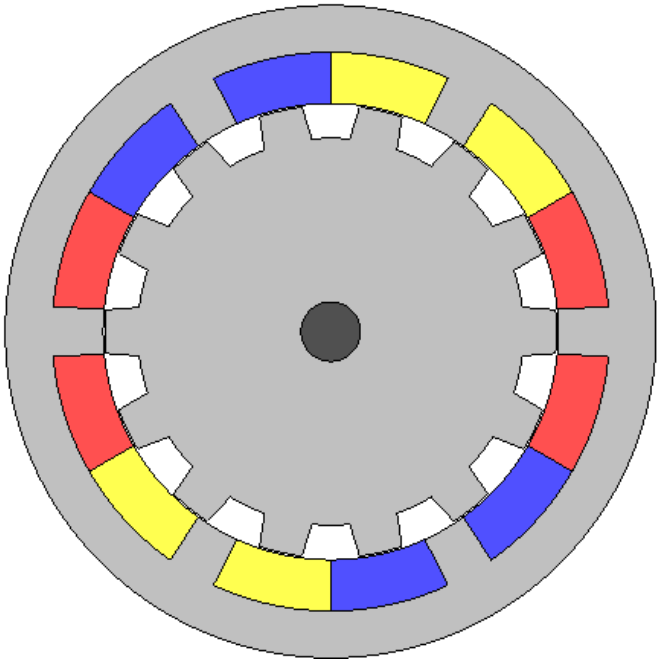

Fig. 5.6. The final design of the optimization problem.

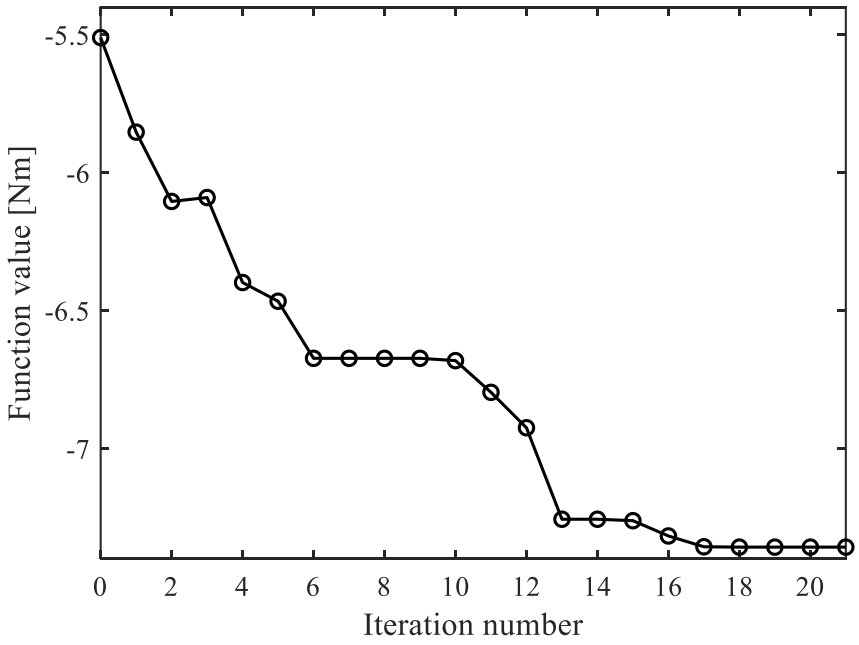

Fig. 5.7. The objective function value versus iteration number characteristic.

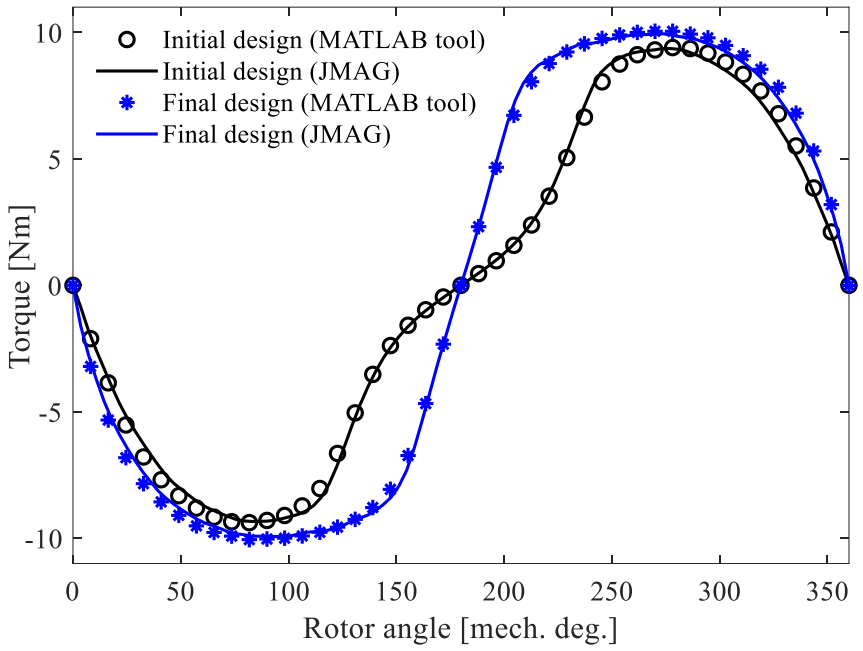

Fig. 5.8. A comparison of the considered SRM static torque profile before and after optimization.

5.4 Simultaneous Optimization (Dynamic Characteristics)

The interior-point method is used to simultaneously optimize the geometry and electric-circuit parameters of an SRM to maximize the motor dynamic torque at a speed of 1103 rpm. There are seven geometric design parameters in addition to four electric-circuit parameters. The geometric design parameters are those of the previous optimization problem. The electric-circuit parameters are the number of turns per coil, reference current, and turn on and turn off angles. The sensitivities of the electromagnetic torque with respect to the geometric design parameters and number of turns are calculated using the AVM. The sensitivities with respect to the reference current, turn-on angle, and turn-off angle are estimated using the CFD since simulations are carried out using MATLAB/SIMULINK which is much faster compared to FEA.

The optimizable design parameters are $\boldsymbol{p} = [h_r \;\; y_s \;\; y_r \;\; \beta_s \;\; \beta_r \;\; \theta_s \;\; \theta_r \;\; N \;\; I_{ref} \;\; \theta_{on} \;\; \theta_{off}]^T$. The objective is to maximize the average value of the dynamic torque $T_{dyn,avg}$. This is achieved by minimizing the negative of $T_{dyn,avg}$. The optimization problem is given by:

$$
\begin{aligned}
&\min_{\boldsymbol{p}} \; f = -T_{dyn,avg} \\
&\textit{subject to} \\
&7 \text{ mm} \le h_r \le 9 \text{ mm}, \\
&10 \text{ mm} \le y_s \le 13 \text{ mm}, \\
&31 \text{ mm} \le y_r \le 37 \text{ mm}, \\
&h_r + y_s + y_r \le 56.855 \text{ mm}, \\
&17.143° \le \beta_s + \beta_r \le 25.714°, \\
&7° \le \beta_s \le 11.5°, \\
&7° \le \beta_r \le 11.5°, \\
&0° \le \theta_s \le 7°, \\
&0° \le \theta_r \le 7°, \\
&95 \le N \le 135, \\
&5A \le I_{ref} \le 6.75A, \\
&-70° \le \theta_{on} \le 60°, \\
&70° \le \theta_{off} \le 200°,
\end{aligned}
\tag{5.8}
$$

The optimization process starts from an initial design $\boldsymbol{p}$ = [7.4mm 10.8mm 32.5mm 10.67° 10.47º 1° 2° 100turn 6.25A -35º 135º]^T and terminates at the optimized design $\boldsymbol{p}$ = [7.1276mm 10.1268mm 33.693mm 10.080º 9.886° 2.0117° 2.583° 135turn 6.6612A -41.865° 134.074°]^T. The objective function values versus iteration number are shown in Fig. 5.9. It should be noted that the objective function in the figure represents the negative of the average value of the dynamic torque in case of un-laminated stator and rotor cores. The static characteristics of the optimized design with 90% stacking factor are obtained by JMAG software as shown in Figs. 5.10 to 5.17. Fig. 5.10 shows the static torque versus

rotor electrical angle characteristics at various excitation currents. The torque increases as the current increases. The same applies to the flux-linkage characteristics shown in Fig. 5.11 where the flux linkage increases with current. However, it can be noticed that at the same rotor position, the increase in the flux linkage with current decreases at higher currents due to saturation. Fig. 5.12 shows the induced phase voltage characteristics. The induced voltage increases with the current at low current levels. However, at high currents and due to saturation the induced voltage may decrease with the current increase. The airgap flux density characteristics are shown in Fig. 5.13. At low currents, the flux density is maximum at the aligned position where the reluctance of the flux path is minimum. This is not the case at high currents due to the saturation which increases the magnetic flux path reluctance. The flux density characteristics of the stator tooth, stator yoke, rotor tooth, and rotor yoke, shown in Figs. 5.14 to 5.17, have the same pattern where the flux density increases as the current increases but the increase rate decreases at high currents.

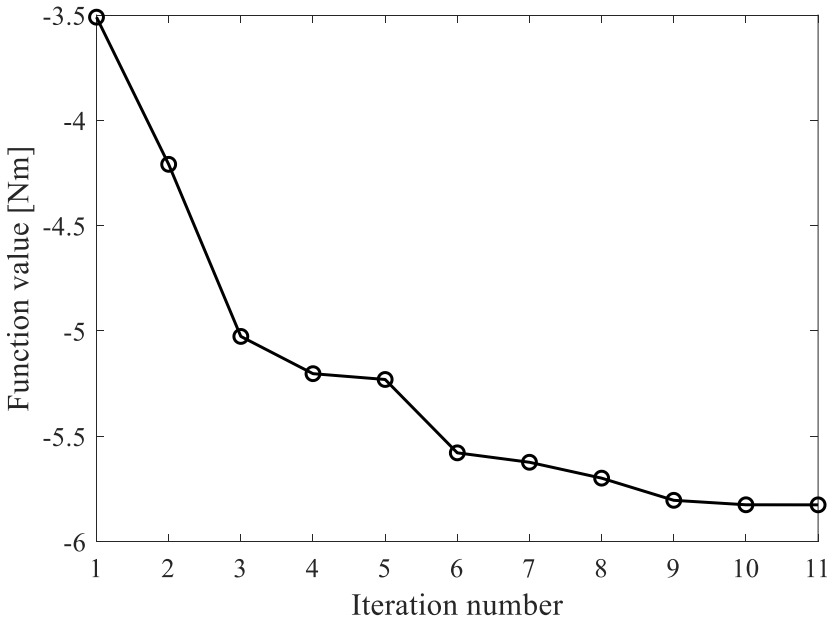

Fig. 5.9. The objective function value versus iteration number characteristic.

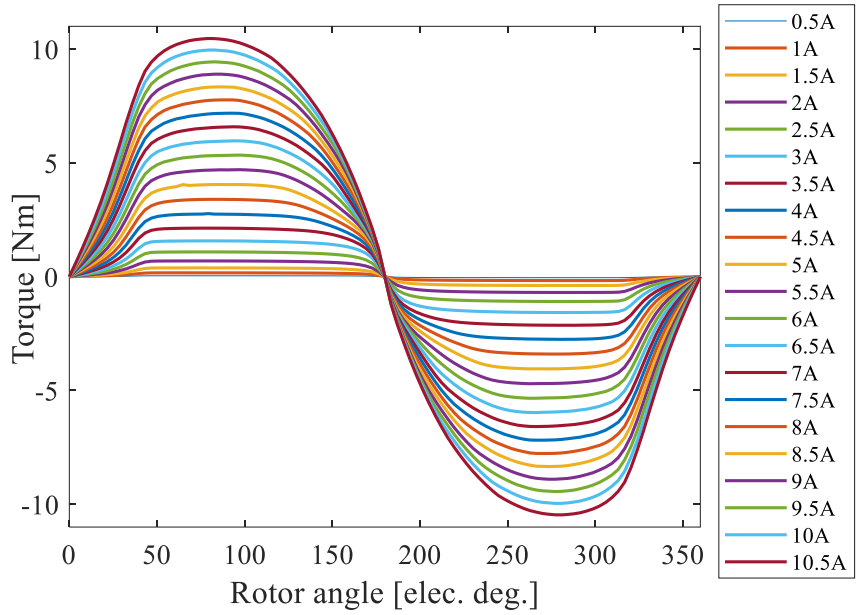

Fig. 5.10. The electromagnetic torque versus electrical angle characteristics at different currents.

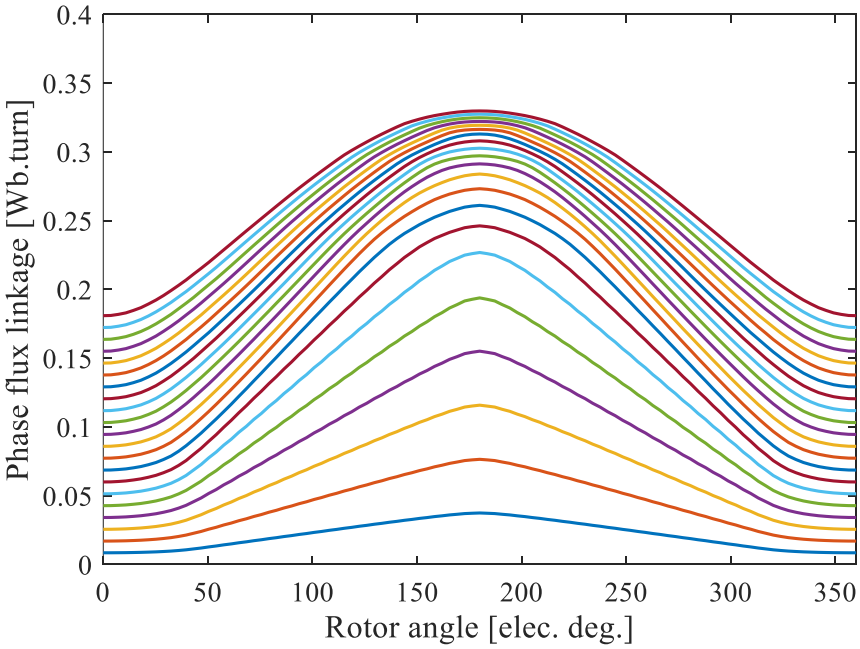

Fig. 5.11. The phase flux linkage versus electrical angle characteristics at different currents.

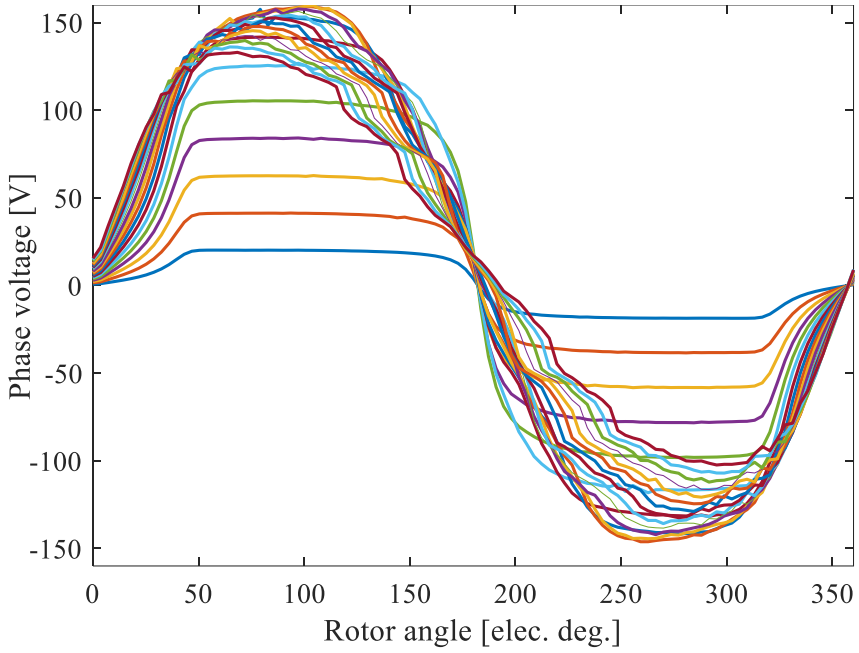

Fig. 5.12. The phase voltage versus electrical angle characteristics at different currents.

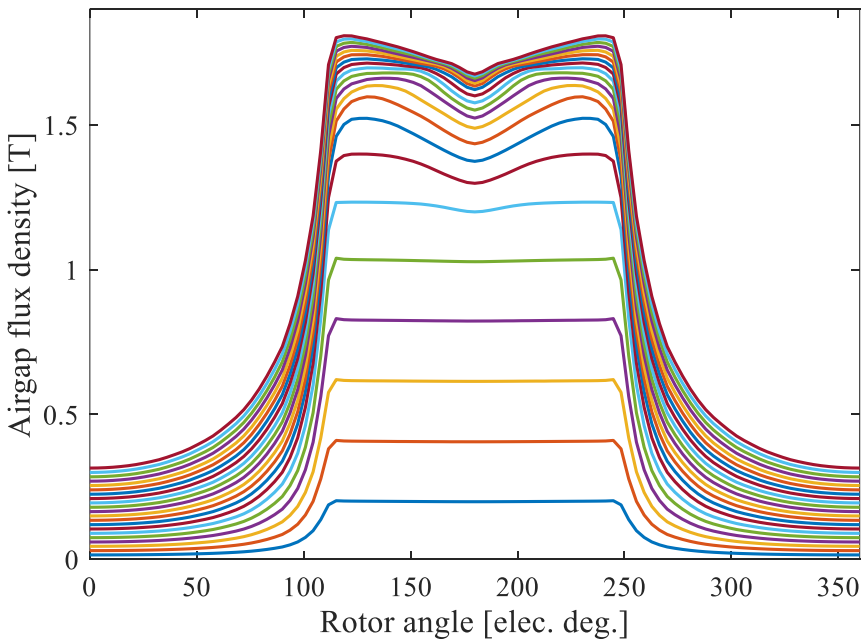

Fig. 5.13. The airgap flux density versus electrical angle characteristics at different currents.

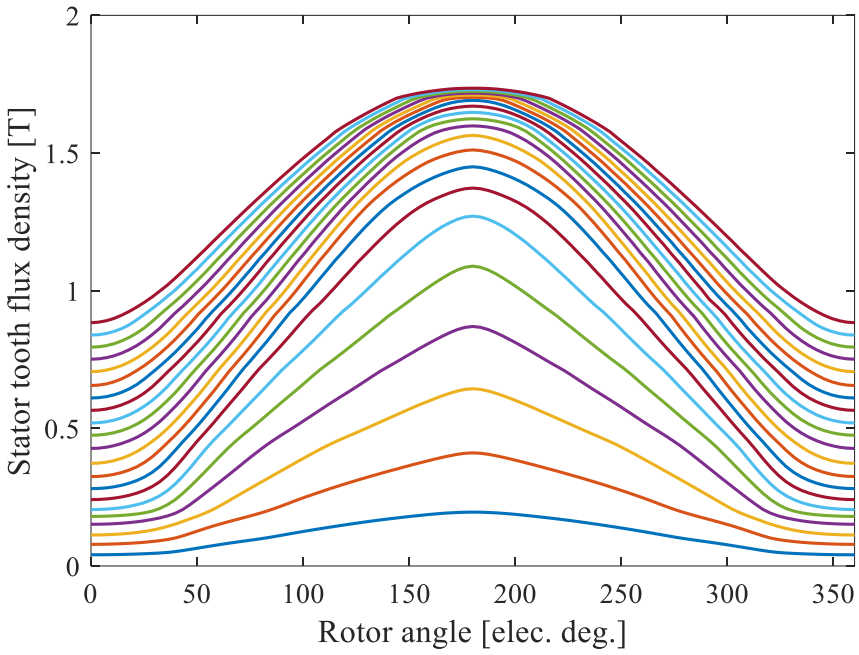

Fig. 5.14. The stator tooth flux density versus electrical angle characteristics at different currents.

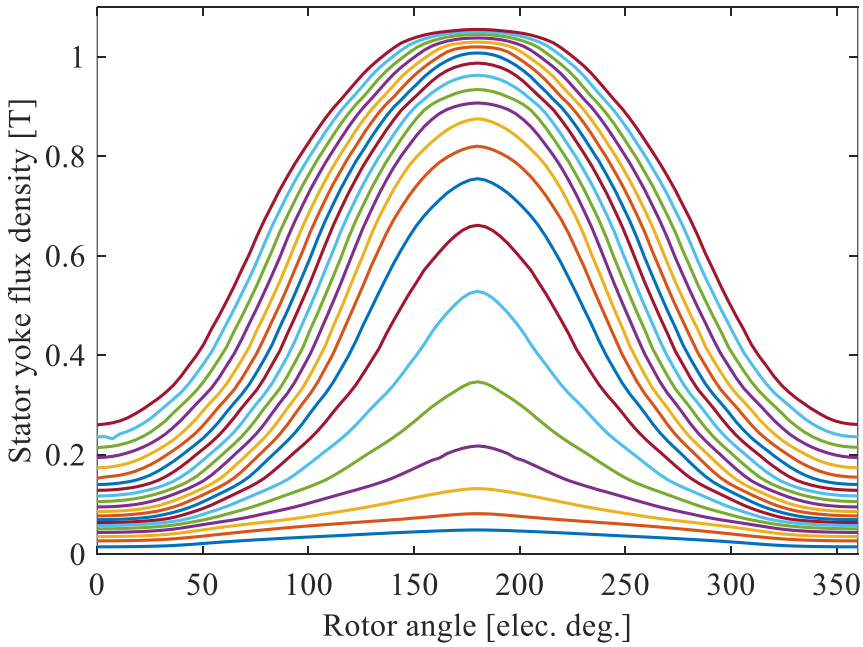

Fig. 5.15. The stator yoke flux density versus electrical angle characteristics at different currents.

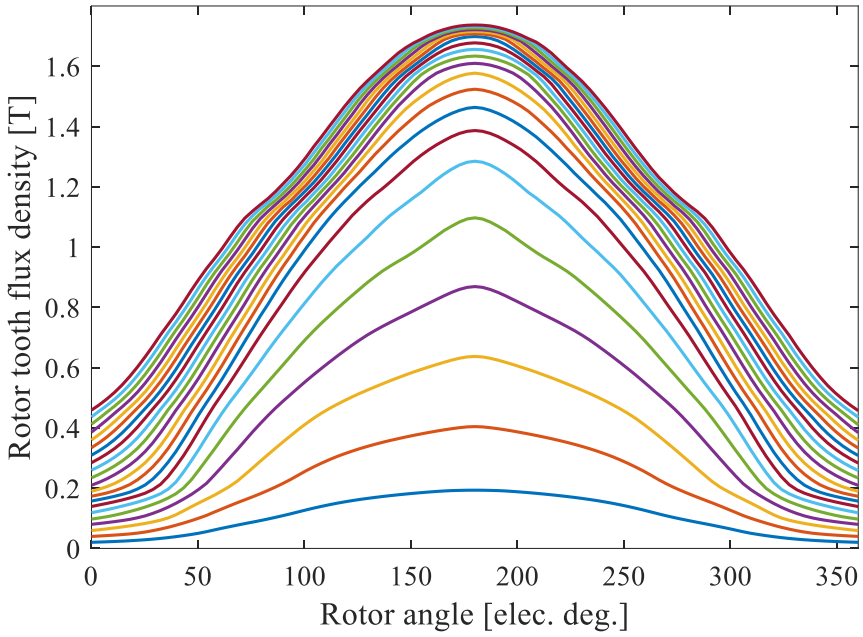

Fig. 5.16. The rotor tooth flux density versus electrical angle characteristics at different currents.

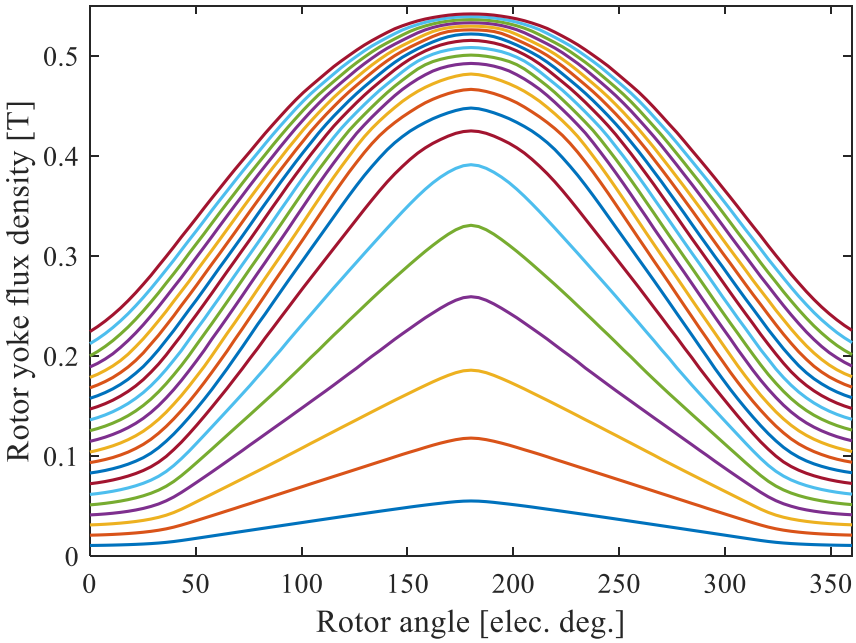

Fig. 5.17. The rotor yoke flux density versus electrical angle characteristics at different currents.

The static torque, flux linkage, and voltage characteristics of the considered motor are utilized by the nonlinear dynamic model to calculate the dynamic performance. The phase

torques versus time characteristics at the speed of 1103 rpm are shown in Fig. 5.18. The total output torque waveform, obtained by summing the phase torques, at that speed is shown in Fig. 5.19. The average torque is 5.57 Nm. The RMS value of the torque ripple at this speed is 0.5 Nm whereas the percentage torque ripple is 38.46%. The high RMS torque ripple will be reduced using a topology optimization technique, as will be presented in the next chapter. The dynamic phase currents of the motor at 1103 rpm are shown in Fig. 5.20. The currents can reach the reference current which is 6.6612A since the motor induced voltage, shown in Fig. 5.21, is lower than the DC link voltage of 163V. The currents are controlled within upper and lower hysteresis bounds. The RMS value of the current is 4.3A. The flux linkage versus current characteristic and the flux linkage versus time characteristics at the same operating speed are shown in Figs. 5.22 and 5.23, respectively.

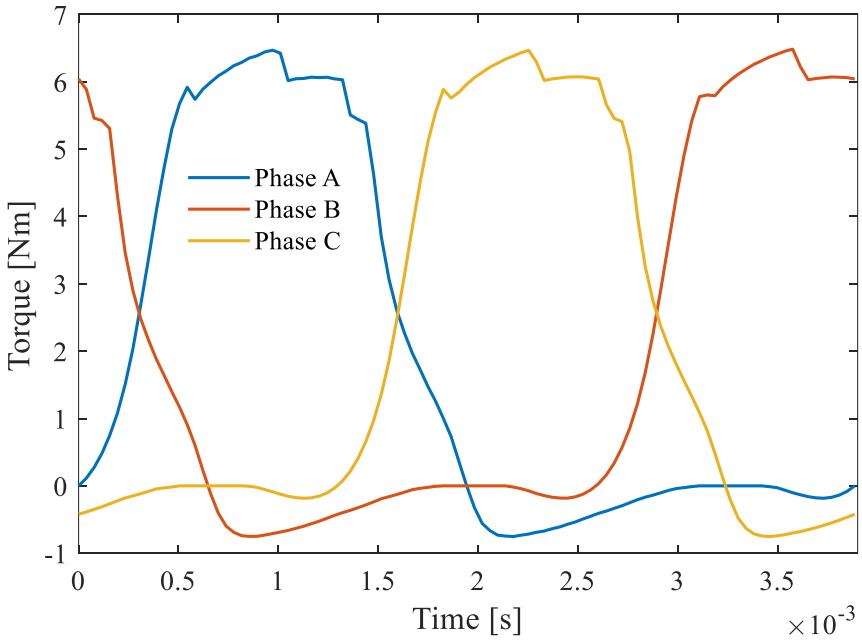

Fig. 5.18. The phase torques versus time characteristic at 1103 rpm.

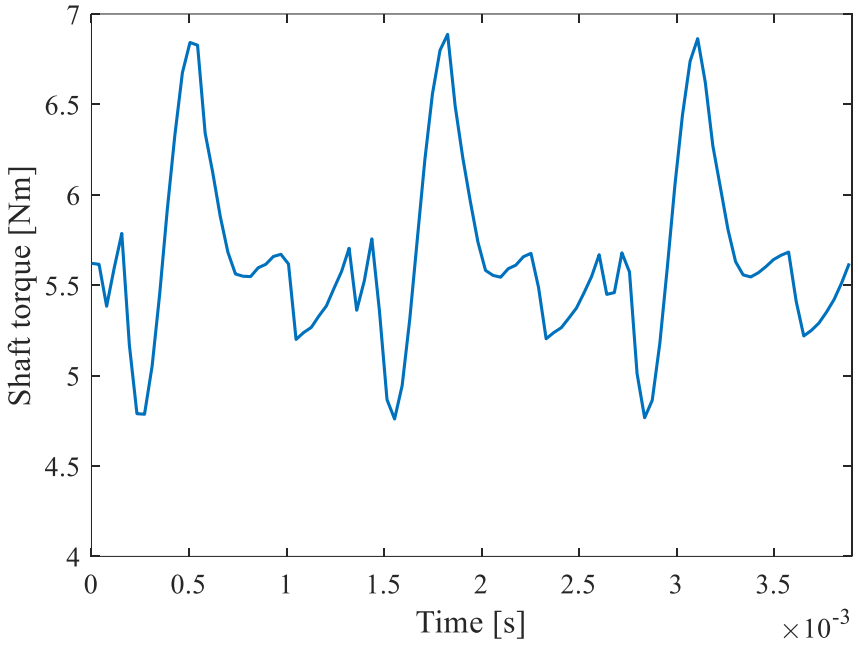

Fig. 5.19. The shaft torque versus time characteristic at 1103 rpm.

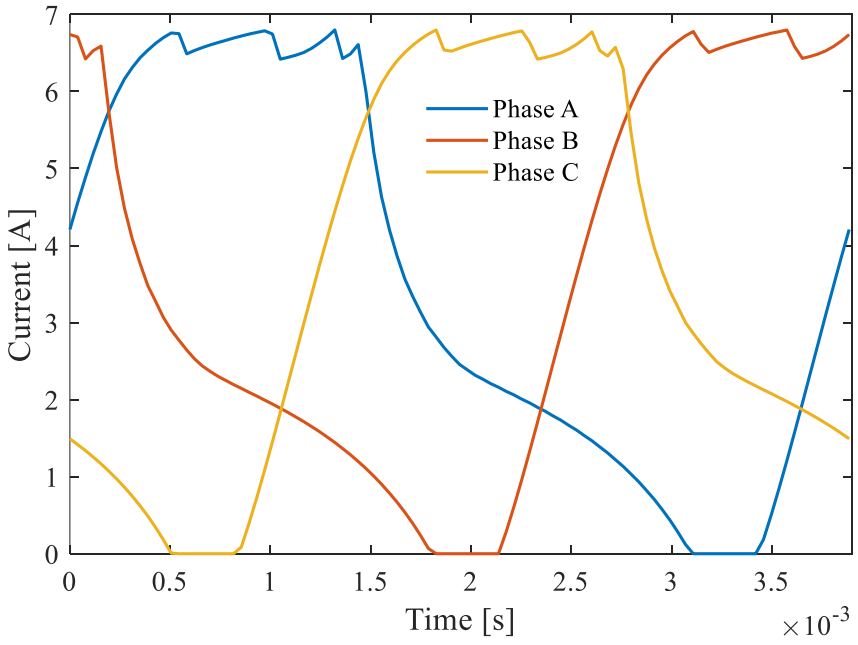

Fig. 5.20. The dynamic phase currents versus time characteristic at 1103 rpm.

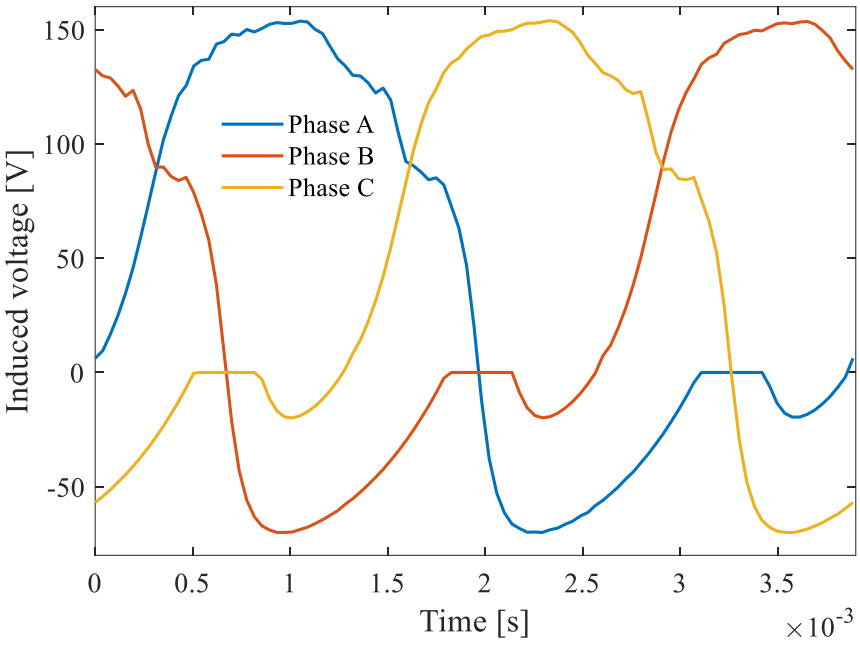

Fig. 5.21. The induced phase voltages versus time characteristic at 1103 rpm.

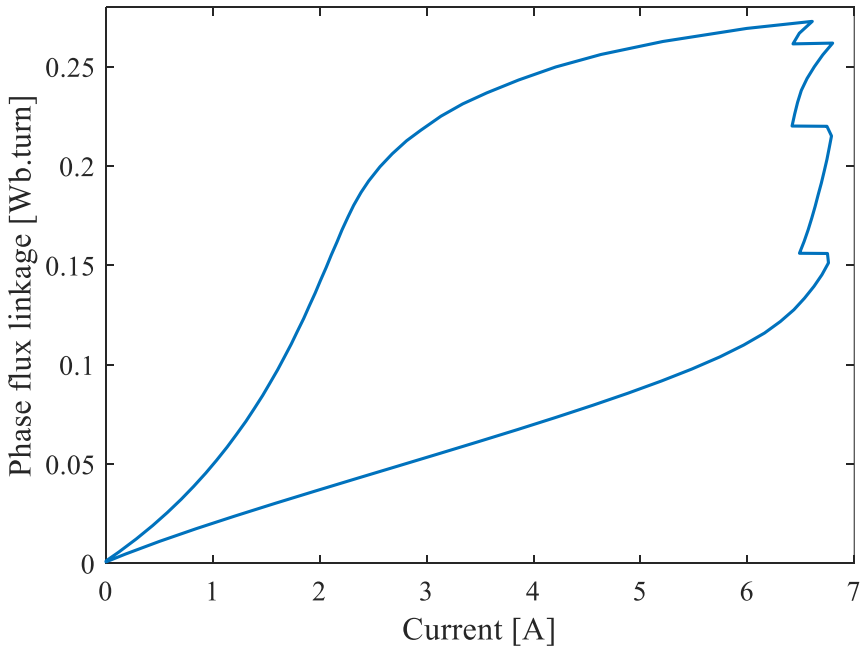

Fig. 5.22. The phase flux linkage versus current characteristic at 1103 rpm.

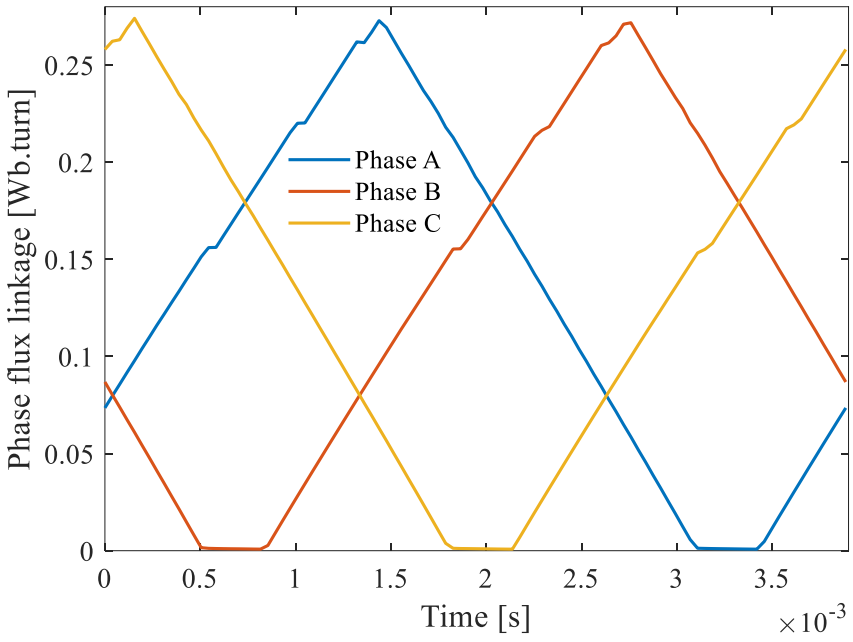

Fig. 5.23. The phase flux linkage versus time characteristics at 1103 rpm.

This page is intentionally left blank

Chapter 6

Adjoint-based Topology Optimization of Nonlinear SRMs

6.1 Introduction

Geometric optimization of electric motors starts with a basic design of the considered motor. The optimizer seeks the optimal values of the design variables without any effect on the motor topology. Topology optimization, however, may provide an unpredicted shape, and hence a new magnetic circuit, which may be beyond the designer expertise [107].

Here, the ON/OFF topology optimization approach is utilized to design an electric motor. The approach requires the sensitivities of the objective function with respect to the reluctivity/permeability of the elements within a chosen design domain. These sensitivities are obtained using the Adjoint Variable Method (AVM) which requires only one additional not-iterative simulation regardless of the number of design domain elements [49].

The target is to minimize the RMS torque ripple of the optimized model which has resulted from the simultaneous optimization presented in Chapter 5. The ON/OFF procedure optimizes the distribution of the magnetic material within the motor stator teeth.

6.2 ON/OFF Topology Optimization

The flowchart of the ON/OFF optimization method is shown in Fig. 6.1. The procedure is as follows [108]; The optimization starts with an initial topology. The following steps are then performed to minimize the objective function:

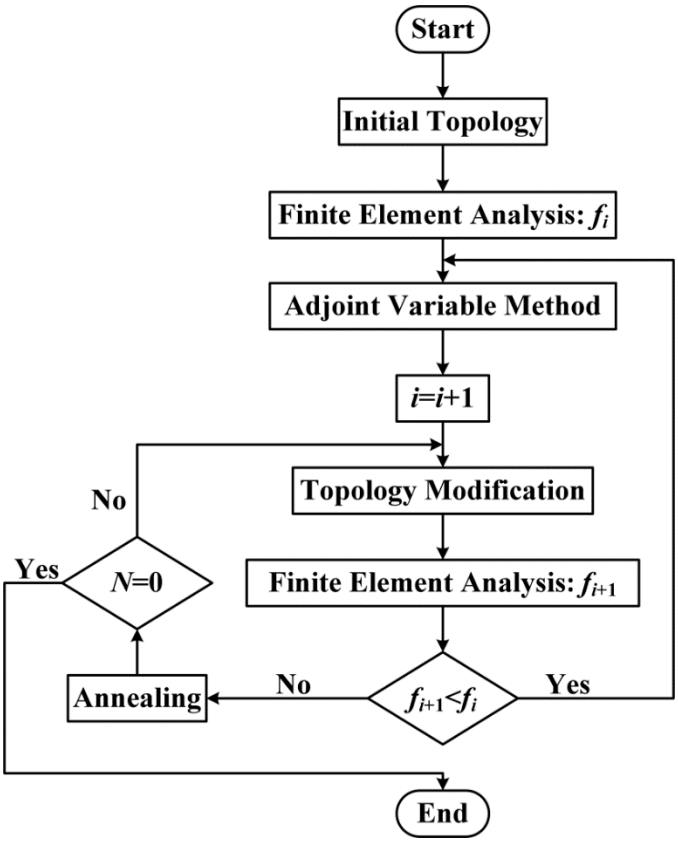

Fig. 6.1. Flowchart of the ON/OFF topology optimization method.

1) The objective function value is calculated using the finite element method.

2) The adjoint variable method is used to obtain the sensitivities of the objective function with respect to the reluctivities of the design domain elements.

   Based on eqn. (4.5), the sensitivity of any objective function with respect to the e^{th} element reluctivity is obtained from

$$\frac{\partial f}{\partial \nu^{(e)}} = -\hat{\boldsymbol{A}}_z^{\,T}\left[\left.\frac{\partial \boldsymbol{K}}{\partial \nu^{(e)}}\right|_{\boldsymbol{A}_z=\bar{\boldsymbol{A}}_z}\bar{\boldsymbol{A}}_z\right],\ \forall e. \tag{6.1}$$

   Comparing eqns. (4.5) and (6.1), it can be concluded that there is no explicit dependence of the objective function on the element reluctivity. The same applies to the forcing vector.

The adjoint magnetic vector potential is obtained from eqn. (4.8).

3) If the calculated sensitivity with respect to an element reluctivity is positive, a magnetic material is assigned to the element. If the sensitivity is negative, the air is assigned instead. This process continues for the elements with the highest sensitivities, either positive or negative, in descending order until the maximum number of designable elements is reached. The designable elements are the elements in which the material changes from air to iron or from iron to air.
4) Finite element analysis is then conducted, and the objective function is recalculated.
5) If the value of the objective function has decreased, then return to step 2. If not, then the maximum number of designable elements is reduced, and return to step 3.

Here, the objective is to minimize the function f in eqn. (6.1) by changing the magnetic material distribution inside the stator teeth. The objective function represents the square of the RMS torque ripple:

$$f = \frac{1}{M}\sum_{k=1}^{M}\left(T_k - 5.8\right)^2, \tag{6.1}$$

where T_k is the torque value at the rotor angle θ_k for k = 1,……., M. M is the total number of simulated rotor positions and the value of 5.8 is the reference average value of the motor dynamic torque in case of unlaminated stator and rotor cores.

The optimization domain is shown in Fig. 6.2 where each pole is divided into two mirrored parts to assure the symmetry of the achieved design. There are 291 elements in the optimization domain. The AVM method requires only one extra not-iterative simulation compared to 582 extra iterative simulations required by the CFD method.

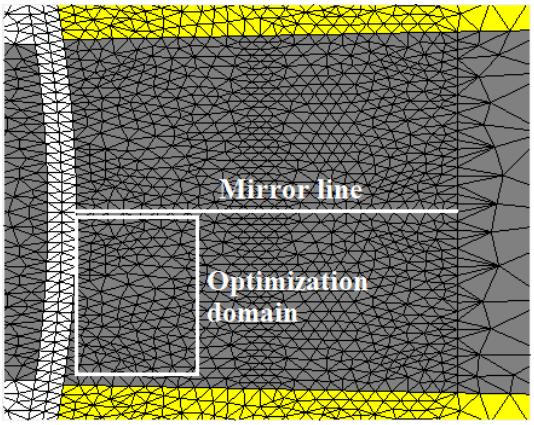

Fig. 6.2. The initial topology of the stator tooth.

The objective function values versus iteration number are shown in Fig. 6.3. The objective function reaches its minimum value at iteration number 4. The change in the distribution of the magnetic material with the iterations is shown in Fig. 6.4.

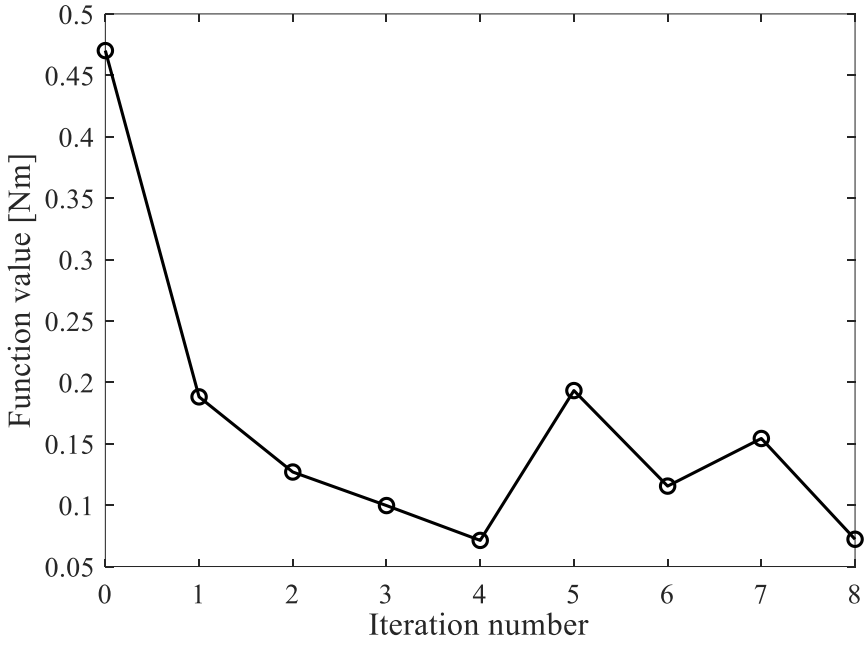

Fig. 6.3. The objective function value versus iteration number characteristic.

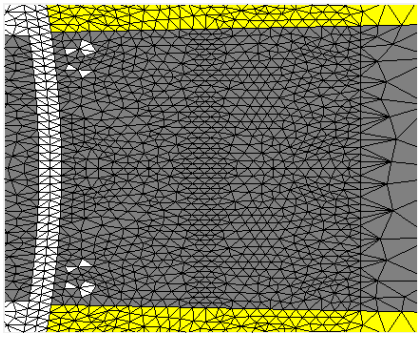

(a) Iteration 1

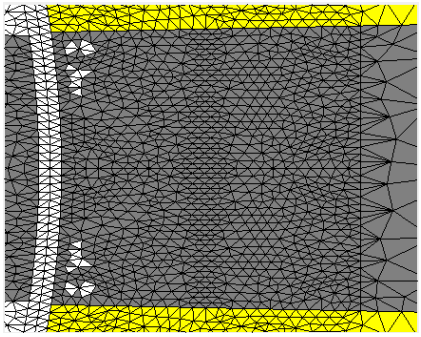

(b) Iteration 2

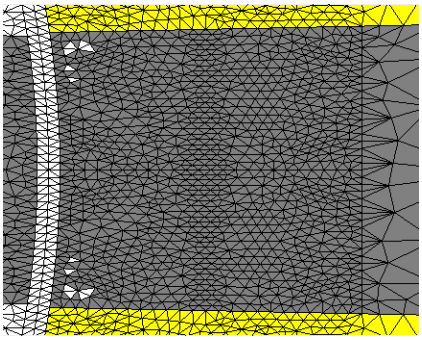

(c) Iteration 3

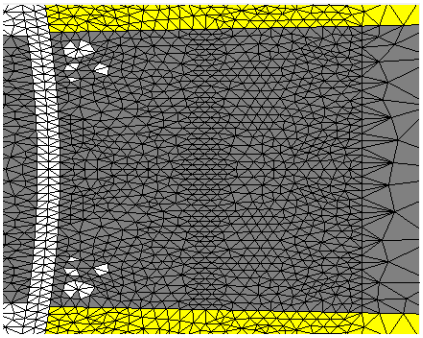

(d) Iteration 4

Fig. 6.4. The evolution of the material distribution in the stator tooth.

The initial and final stator tooth designs are shown in Fig. 6.5.

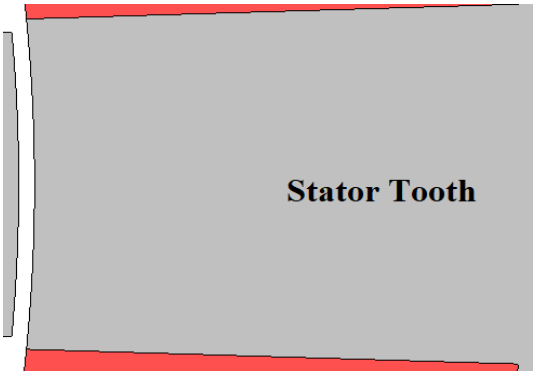

(a) Initial stator tooth.

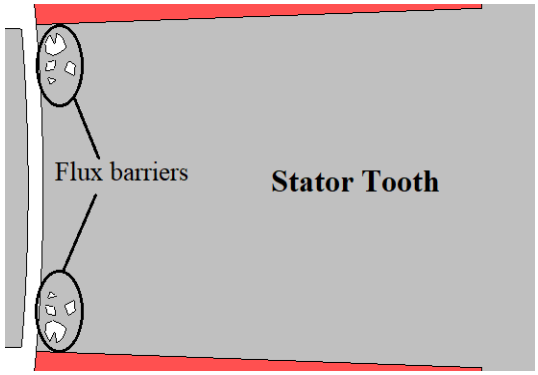

(b) Final stator tooth.

Fig. 6.5. The initial and final stator tooth designs.

The static torque, flux linkage, and voltage characteristics of the optimized design with 90% stacking factor are obtained by JMAG software as shown in Figs. 6.6 to 6.8, respectively.

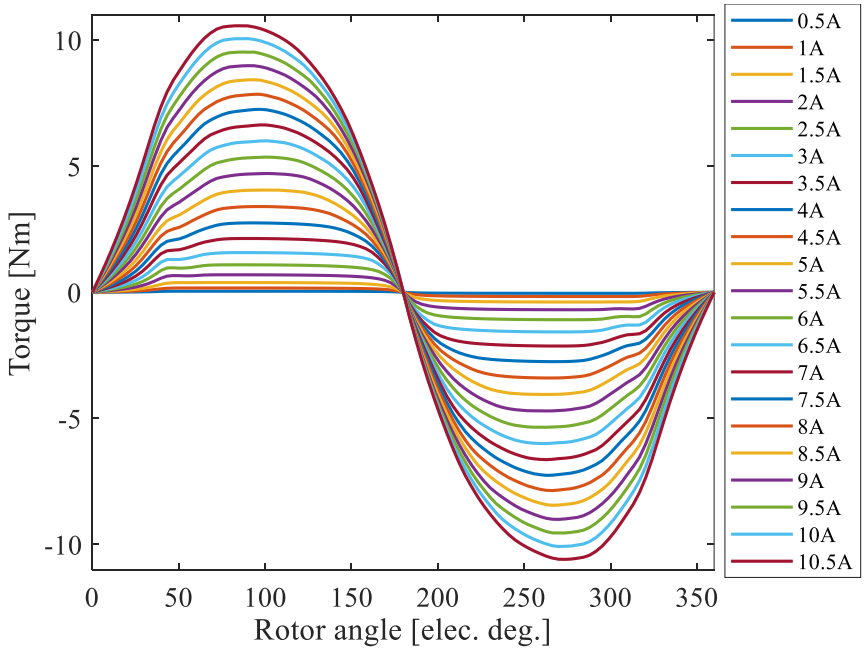

Fig. 6.6. The electromagnetic torque versus electrical angle characteristics at different currents.

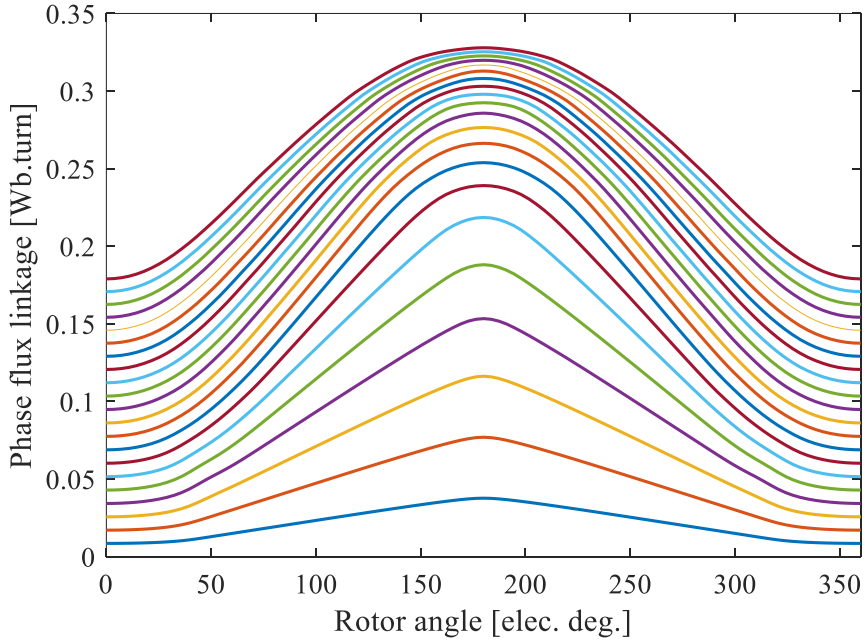

Fig. 6.7. The phase flux linkage versus electrical angle characteristics at different currents.

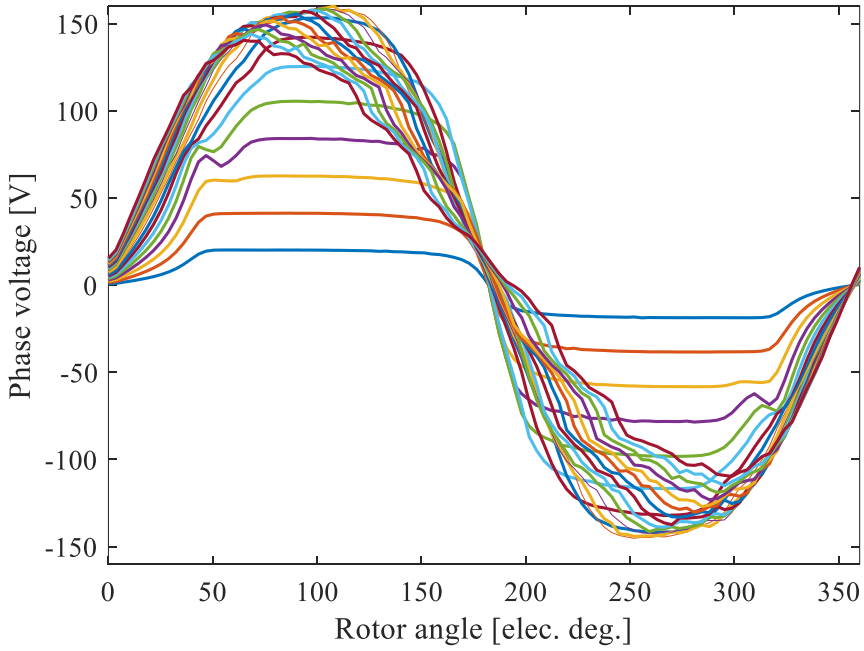

Fig. 6.8. The phase voltage versus electrical angle characteristics at different currents.

The flux density distribution and the flux lines of the designs before and after the topology optimization at a phase-A current of 6.5A at the aligned position are shown in Figs. 6.9 and 6.10, respectively.

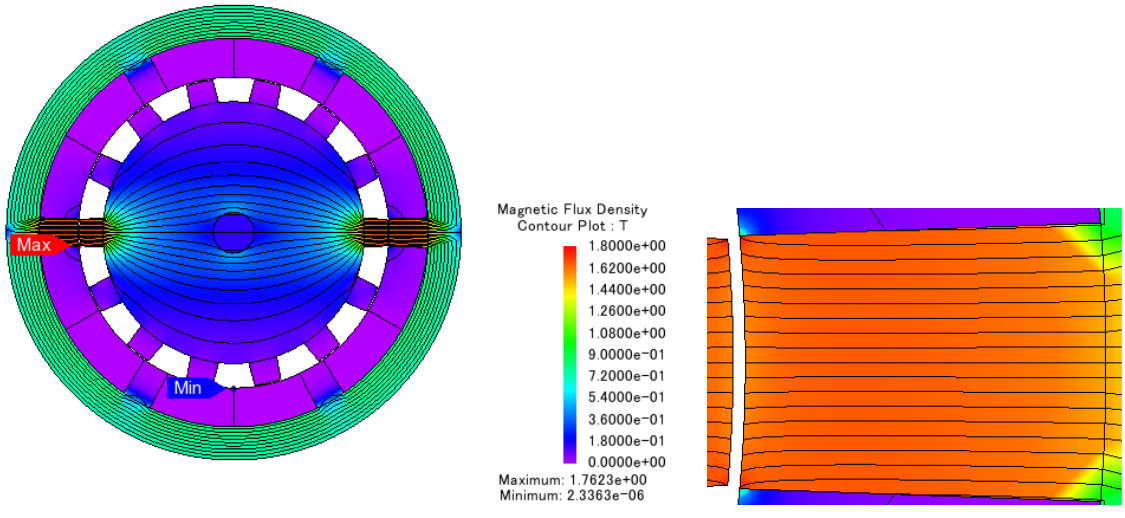

(a) (b)

Fig. 6.9. The flux density distribution of the non-optimized design at a current of 6.5A at the aligned position (a) complete design. (b) Stator tooth.

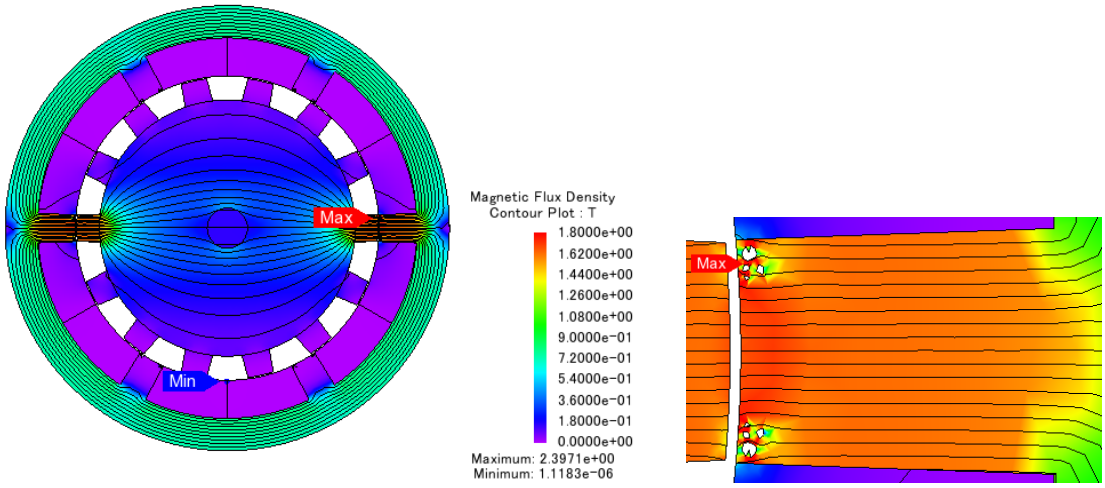

(a) (b)

Fig. 6.10. The flux density distribution of the optimized design at a current of 6.5A at the aligned position (a) complete design. (b) Stator tooth.

Comparing Figs. 6.9 and 6.10, it can be noticed that the flux barriers affect the flux density distribution inside the stator teeth which affects the airgap flux density, and hence the motor performance. The airgap flux density characteristics of the optimized design at different currents are shown in Fig. 6.11.

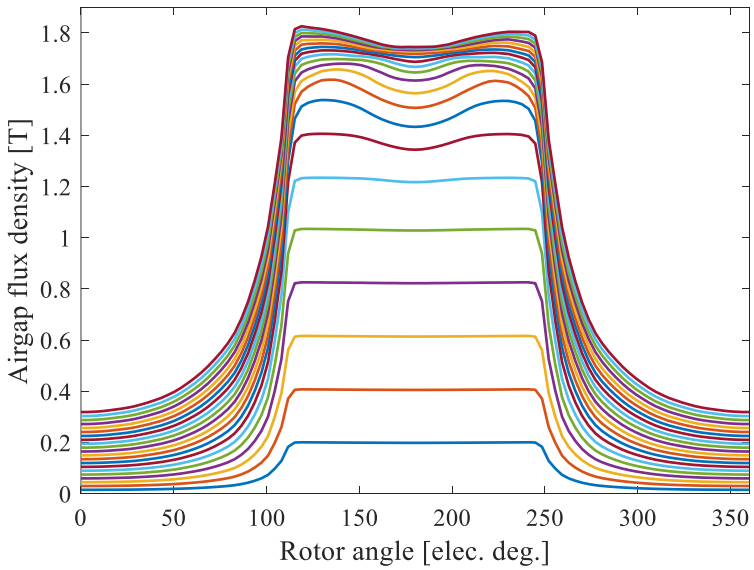

Fig. 6.11. The airgap flux density versus electrical angle characteristics at different currents.

Compared to the airgap flux density characteristics of the non-optimized design, shown in Fig. 5.13, the optimized design characatistics are smoother and have lower flux density dips at the aligned position at higher current levels. This indicates, to some extent, a reduced torque ripple in case of the optimized design.

The static torque, flux linkage, and voltage characteristics of the considered motor are utilized by the nonlinear dynamic model to calculate the dynamic performance. The phase torques versus time characteristics at the speed of 1103 rpm are shown in Fig. 6.12. A comparison between the total output torque waveforms of the designs before and after topology optimization at that speed are shown in Fig. 6.13. The average torque of both designs is 5.57 Nm. The RMS value of the torque ripple has been reduced from 0.5 Nm to 0.268 Nm whereas the percentage torque ripple has been reduced from 38.46% to 22.6%. The dynamic phase currents of the optimized motor at 1103 rpm are shown in Fig. 6.14. The reference current has been raised to 6.83A to achieve the same torque obtained before the topology optimization. The dynamic currents can still reach the reference current since the motor induced voltage, shown in Fig. 6.15, is lower than the DC link voltage. The RMS value of the current has been increased from 4.3A to 4.41A. A comparison between the flux linkage versus current characteristic of both designs is shown in Fig. 6.16. Fig. 6.17 shows that the radial forces on a stator tooth tip circumference has been significantly reduced in the case of the optimized design.

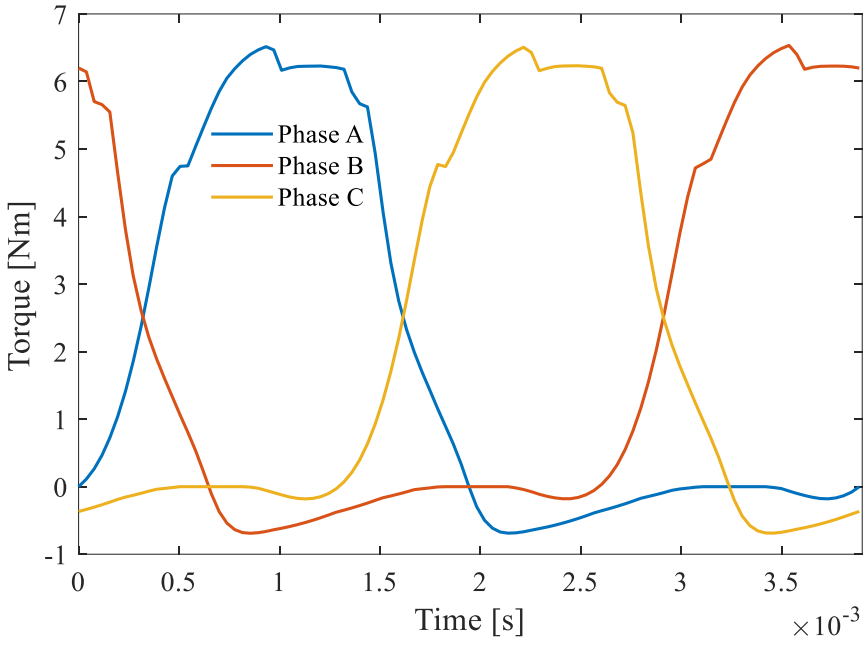

Fig. 6.12. The phase torques versus time characteristic of the optimized design at 1103 rpm.

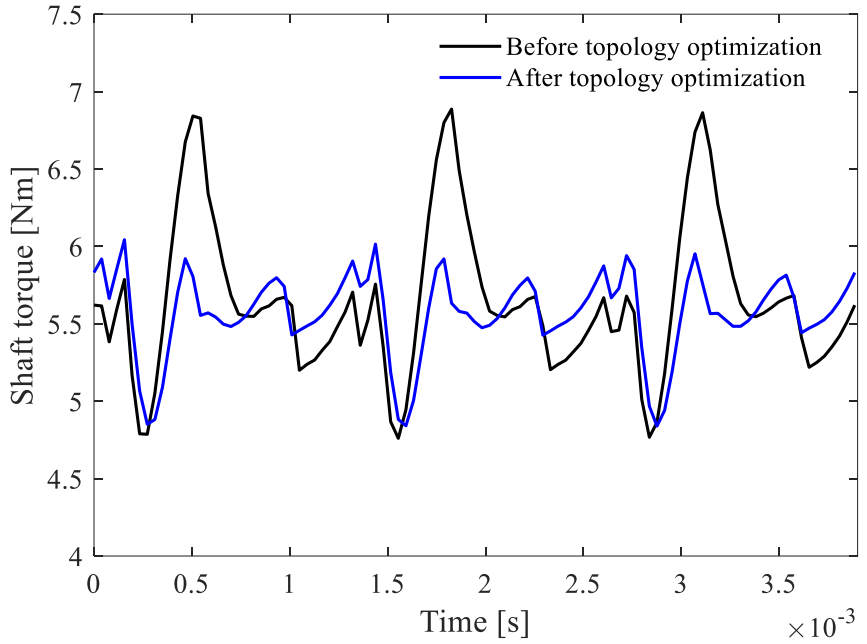

Fig. 6.13. The shaft torque versus time characteristics of the non-optimized and optimized designs.

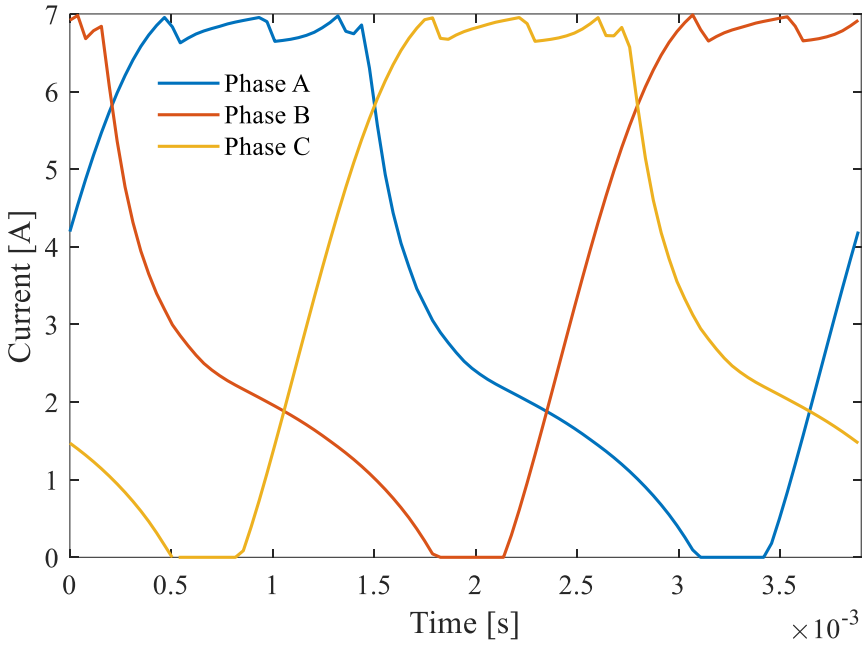

Fig. 6.14. The dynamic phase currents versus time characteristic of the optimized design at 1103 rpm.

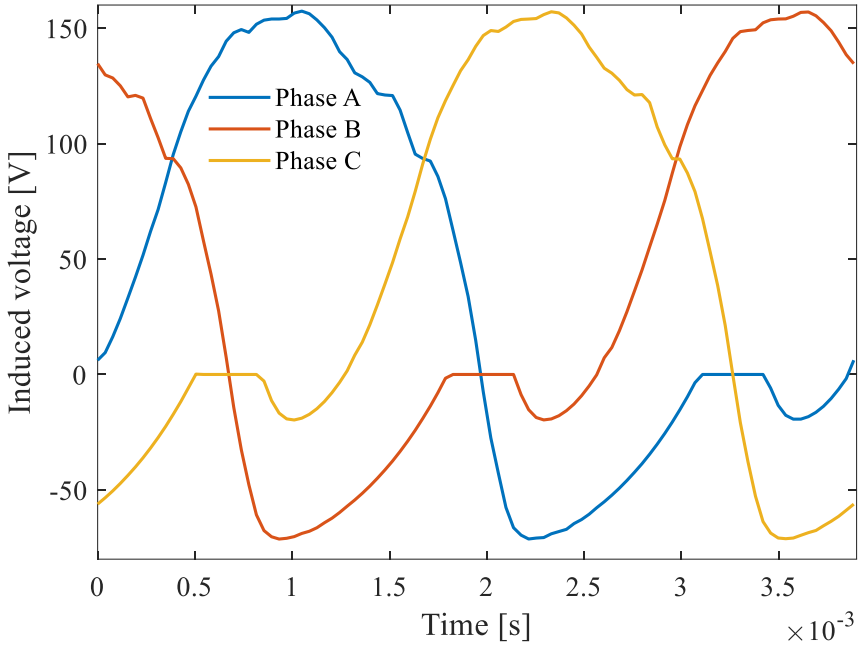

Fig. 6.15. The induced phase voltages versus time characteristic of the optimized design at 1103 rpm.

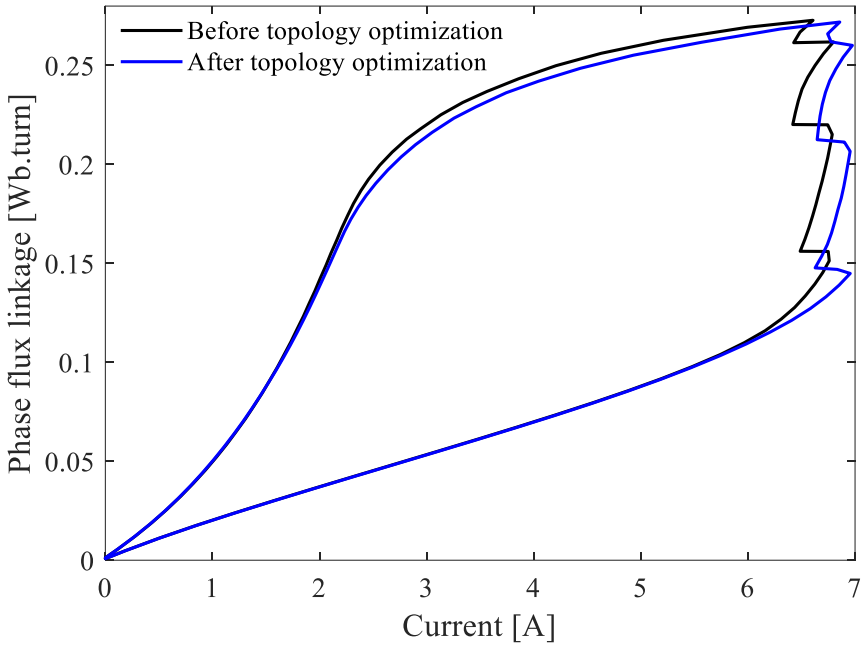

Fig. 6.16. The phase flux linkage versus current characteristics of the non-optimized and optimized designs.

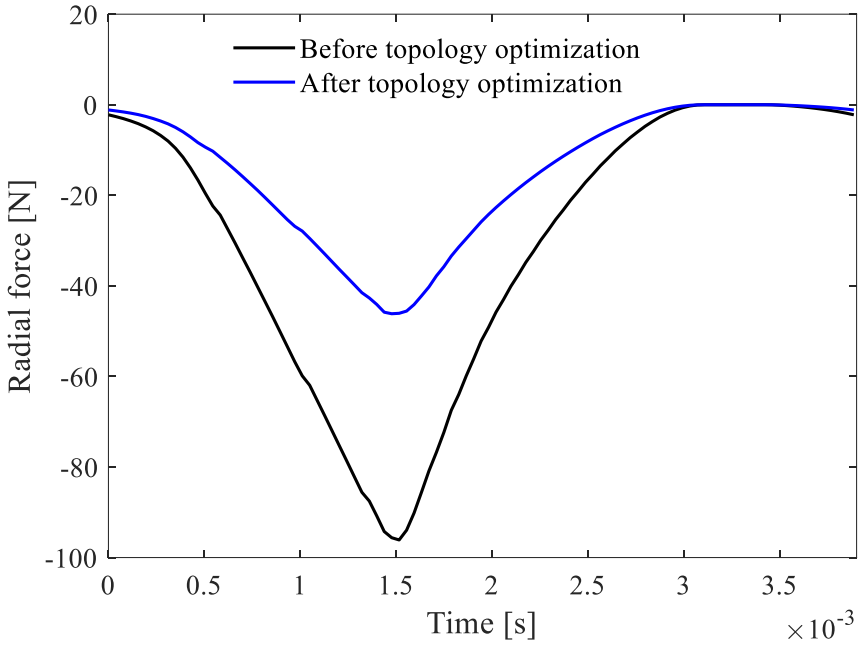

Fig. 6.17. The radial force on a stator tooth tip circumference versus time characteristics of the non-optimized and optimized designs.

This page is intentionally left blank

Chapter 7

Conclusions, Future Work, and Publications

7.1 Conclusions

The thesis includes finite element analysis of switched reluctance motors when utilizing either linear or nonlinear magnetic materials. The adjoint variable method is used for the sensitivity analysis of SRMs in both linear and nonlinear cases. In the thesis, geometry, control, and topology optimization approaches are applied to a 6/14 SRM to achieve the performance specifications of a commercially available surface-mounted PM brushless DC motor of an HVAC system.

Chapter 2 presented the construction, working principle, and modeling of SRMs. The fundamentals of magnetostatic finite element analysis in case of utilizing linear and nonlinear magnetic materials were also investigated. Various electromagnetic responses of SRMs were then calculated using the finite element method.

Chapter 3 introduced the sensitivity analysis using the adjoint variable method in case of linear and nonlinear systems of equations.

Chapter 4 studied the sensitivities of various static and dynamic electromagnetic responses of SRMs with respect to different geometric design parameters. The obtained sensitivities using the adjoint variable method were compared to those estimated using the more-accurate but time-intensive Central Finite Differences (CFD). A good match was shown between the two sets of results.

Chapter 5 investigated geometric optimization of eight geometric design parameters of the considered 6/14 SRM to maximize the motor static torque profile using the interior-point algorithm. The design parameters are teeth height, yoke thickness, pole arc angle, and taper angle of both stator and rotor. A structural mapping technique was utilized to control the geometry of the design parameters. In addition to the motor static torque profile, the steady-state dynamic torque was maximized by simultaneously optimizing the motor geometry and the drive-circuit control parameters. The optimized motor meets the design targets of a surface-mounted PM brushless DC motor. An average torque of 5.57 Nm at 1103 rpm has been achieved. The RMS value of the torque ripple is 0.5 Nm while the percentage torque ripple is 38.46%. The RMS value of the phase current is 4.3 A.

Chapter 6 studied the topology optimization of the considered SRM to minimize the RMS torque ripple at a specific average value of the dynamic torque. The ON/OFF topology optimization technique was utilized to optimize the ferromagnetic material distribution in the stator teeth for that purpose. The average torque has been kept at 5.57 Nm at 1103 rpm. The RMS value of the torque ripple has been reduced from 0.5 Nm to 0.268 Nm whereas the percentage torque ripple has been reduced from 38.46% to 22.6%. Moreover, the radial forces on the stator tooth tip circumference were reduced after applying the topology optimization. However, the RMS value of the current has been increased from 4.3 A to 4.41 A.

7.2 Future Work

The following topics are recommended for future investigation:

1) Apply the adjoint variable method to a 3D analysis of SRMs.

2) Utilize the sensitivity analysis to define the number of stator and rotor teeth of SRMs.
3) Study the sensitivity of other electromagnetic responses of SRMs such as radial forces versus the geometry and ferromagnetic material distribution of the motor. This may serve in reducing the motor acoustic noise which is a main drawback of SRMs.
4) Other objective functions and constraints may be included in the optimization process such as motor efficiency, torque and power densities, temperature distribution, and structural integrity.
5) In this thesis, topology optimization has been utilized to optimize the material distribution inside the stator teeth. The approach could be further extended to shape the stator and rotor teeth by including the teeth boundary elements in the optimization process.
6) Interior-point optimization algorithm is utilized in this thesis. The effect of utilizing different deterministic optimization algorithms on the motor performance may be investigated.
7) Investigate in more details calculating the sensitivity of the objective function with respect to discrete design parameters.

7.3 Publications

7.3.1 Journal Papers

1. **E. Sayed**, M. H. Bakr, B. Bilgin, and A. Emadi, "Adjoint sensitivity analysis of switched reluctance motors," *Electric Power Components and Systems*, vol. 46, no. 18, pp. 1959-1968, December 2018.

2. **E. Sayed**, M. H. Bakr, B. Bilgin, and A. Emadi, "Adjoint-based design optimization of nonlinear switched reluctance motors," Submitted, *Electric Power Components and Systems*.
3. **E. Sayed**, S. M. Castano, J. W. Jiang, J. Liang, B. Bilgin, A. Sathyan, H. Dadkhah, M. H. Bakr, and A. Emadi, "Comparative analysis for multi-layer concentric ferrite magnet traction generator designs," To be submitted to FCA US LLC for review and to be submitted to a Journal.
4. **E. Sayed**, Y. Yang, B. Bilgin, M. H. Bakr, and A. Emadi, "A comprehensive review of flux barriers in interior permanent magnet synchronous machines," To be submitted to IEEE Access Journal.
5. **E. Sayed**, R. Yang, J. Liang, M. H. Bakr, B. Bilgin, and A. Emadi, "Design of unskewed interior permanent magnet traction motor with asymmetric flux barriers and shifted magnets for Nissan Leaf electric vehicle," Submitted, *Electric Power Components and Systems*.

7.3.2 Conference Papers

1. **E. Sayed**, M. H. Bakr, B. Bilgin, and A. Emadi, "Geometric optimization of switched reluctance motors using an invasive weed method," in *Proc. IEEE Electrical Power and Energy Conference* (EPEC), Toronto, Canada, October 2018, pp. 1-3.
2. **E. Sayed**, P. Azer, M. Kordic, J. Reimers, B. Bilgin, M. H. Bakr, and A. Emadi, "Design of switched reluctance motors for a pump jack application," in *Proc. IEEE Electrical Power and Energy Conference* (EPEC), Toronto, Canada, October 2018, pp. 1-6.

3. **E. Sayed**, M. H. Bakr, B. Bilgin, and A. Emadi, "A MATLAB toolbox for adjoint-based sensitivity analysis of switched reluctance motors," in *Proc. IEEE Electrical Power and Energy Conference* (*EPEC*), Toronto, Canada, October 2018, pp. 1-4.
4. S. M. Castano, **E. Sayed**, J. W. Jiang, J. Liang, B. Bilgin, A. Sathyan, H. Dadkhah, Dhafar-Al Ani, Nitin Patel, and A. Emadi, "Design of a spoke-type ferrite magnet generator for a hybrid electric vehicle application," in *Proc. IEEE Transportation Electrification Conference and Expo* (*ITEC*), Novi, MI, June 2019.
5. **E. Sayed**, M. H. Bakr, B. Bilgin, and A. Emadi, "Adjoint-based design optimization of a switched reluctance motor for an HVAC application". To be submitted to a conference.

This page is intentionally left blank

References

1. N. Bianchi, *Electrical Machine Analysis Using Finite Elements*, CRC Press, 2005. ISBN: 978-1315219295.
2. M. Sadiku, *Elements of Electromagnetics*, Oxford University Press, Sixth Edition, 2014. ISBN: 978-0199321384.
3. T. Tusar, P. Korosec, G. Papa, B. Filipic, and J. Silc, "A comparative study of stochastic optimization methods in electric motor design," *Applied Intelligence*, vol. 27, no. 2, pp. 101-111, October 2007.
4. M. Kasprzak, "6/14 switched reluctance machine design for household HVAC system applications (Ph.D. Dissertation)," McMaster University, Hamilton, 2016.
5. J. Rowlatt, "Rare earths: Neither rare, nor earths," BBC World Service, 23 Mar 2014. [Online]. Available: http://www.bbc.com/news/magazine-26687605. [Accessed 28 March 2019].
6. S. I. Cosman, V. I. Boanca, C. Oprea, and C. S. Martis. "Design, building and testing of a low voltage-high current drive for SRMs used for HVAC applications," in *Proc. International Conference and Exposition on Electrical and Power Engineering* (*EPE*), Iasi, Romania, October 2018, pp. 58-62.
7. N. Zabihi and R. Gouws, "A review on switched reluctance machines for electric vehicles," in *Proc. IEEE International Symposium on Industrial Electronics* (*ISIE*), Santa Clara, CA, June 2016, pp. 799-804.

8. A. Y. Anekunu, S. P. Chowdhury, and S. Chowdhury, "A review of research and development on switched reluctance motor for electric vehicles," in *Proc. IEEE Power & Energy Society General Meeting*, BC, Canada, July 2013, pp. 1-5.
9. K. Vijayakumar, R. Karthikeyan, S. Paramasivam, R. Arumugam, and K. N. Srinivas, "Switched reluctance motor modeling, design, simulation, and analysis: a comprehensive review," *IEEE Transactions on Magnetics*, vol. 44, no. 12, pp. 4605-4617, December 2008.
10. V. Petrus, A. C. Pop, C. S. Martis, J. Gyselinck, and V. Iancu, "Design and comparison of different switched reluctance machine topologies for electric vehicle propulsion," in *Proc. International Conference on Electrical Machines* (ICEM), Rome, Italy, September 2010, pp. 1 – 6.
11. V. Rallabandi and B. G. Fernandes, "Design methodology for high-performance segmented rotor switched reluctance motors," *IEEE Transactions on Energy Conversion*, vol. 30, no. 1, pp. 11-21, March 2015.
12. N. N. Fulton and J. M. Stephenson, "A review of switched reluctance machine design," in *Proc. IEE Electric Machines Conference*, 1988, pp. 120–126.
13. L. M. M. Sitsha and M. J. Kamper, "Some design aspects of tapered and straight stator pole 6:4 switched reluctance machine," in *Proc. IEEE Africon Conference in Africa*, Cape Town, South Africa, September 1999, pp. 683–686.
14. M. C. Tsai, C. C. Hang, and Z. Y. Huang, "A new two-phase homopolar switched reluctance motor for electric vehicle applications," *Journal of Magnetism and Magnetic Materials*, vol. 267, no. 2, pp. 173–181, December 2003.

15. Y. Yang, N. Schofield, and A. Emadi, “Double-rotor switched reluctance machine (DRSRM),” *IEEE Transactions on Energy Conversion*, vol. 30, no. 2, pp. 671–680, June 2015.
16. Y. Yang, N. Schofield, and A. Emadi, “Integrated electro-mechanical double-rotor compound hybrid transmissions for hybrid electric vehicles,” *IEEE Transactions on Vehicular Technology*, vol. 65, no. 6, pp. 4687–4699, June 2016.
17. A. Labak and N. C. Kar, “Outer rotor switched reluctance motor design for in-wheel drive of electric bus applications,” in *Proc. International Conference on Electrical Machines*, Marseille, France, September 2012, pp. 418-423.
18. K. Kiyota, T. Kakishima, A. Chiba and M. A. Rahman, “Cylindrical rotor design for acoustic noise and windage loss reduction in switched reluctance motor for HEV applications,” *IEEE Transactions on Industry Applications*, vol. 52, no. 1, pp. 154-162, February 2016.
19. V. Rallabandi and B. G. Fernandes, “Design procedure of segmented rotor switched reluctance motor for direct drive applications,” *IET Electric Power Applications*, vol. 8, no. 3, pp. 77–88, March 2014.
20. G.-Z. Cao, J.-L. Fang, S.-D. Huang, J.-A. Dua, and J. F. Pan, “Optimization design of the planar switched reluctance motor on electromagnetic force ripple minimization,” *IEEE Transactions on Magnetics*, vol. 50, no. 11, November 2014.
21. M. M. Nezamabadi, E. Afjei, and H. Torkaman, “Design, dynamic electromagnetic analysis, fem, and fabrication of a new switched-reluctance motor with hybrid motion,” *IEEE Transactions on Magnetics*, vol. 52, no. 4, April 2016.

22. K. M. Rahman, B. Fahimi, G. Suresh, A. V. Rajarathnam, and M. Fhami, "Advantages of switched reluctance motor applications to EV and HEV: design and control issues," *IEEE Transactions on Industrial Applications*, vol. 36, no. 1, pp. 111–121, February 2000.

23. B. Bilgin, A. Emadi, and M. Krishnamurthy, "Comprehensive evaluation of the dynamic performance of a 6/10 SRM for traction application in PHEVs," *IEEE Transactions on Industrial Electronics*, vol. 60, no. 7, pp. 2564–2575, July 2013.

24. L. Gu, W. Wang, B. Fahimi, A. Clark, and J. Hearron, "Magnetic design of two-phase switched reluctance motor with bidirectional startup capability," *IEEE Transactions on Industry Applications*, vol. 52, no. 3, pp. 2148-2155, January 2016.

25. W. F. Ray, R. M. Davis, P. J. Lawrenson, J. M. Stepenson, N. N. Fulton, and R. J. Blake, "Switched reluctance motor drives for rail traction: a second view," *IEE Proceedings B - Electric Power Applications*, vol. 131, no. 5, pp. 220–225, September 1984.

26. M. R. Harris, J. W. Finch, J. A. Mallick, and T. J. E. Miller, "A review of the integral-horsepower switched reluctance motor drive," *IEEE Transactions on Industry Applications*, vol. IA-22, no. 4, pp. 716–721, August 1986.

27. T. Uematsu and R. S. Wallace, "Design of a 100 kW switched reluctance motor for electric vehicle propulsion," in *Proc. IEEE Applied Power Electronics Conference and Exposition* (*APEC*), Dallas, TX, March 1995, pp. 411–415.

28. K. Kiyota and A. Chiba, “Design of switched reluctance motor competitive to 60-kW IPMSM in third-generation hybrid electric vehicle,” *IEEE Transactions on Industry Applications*, vol. 48, no. 6, pp. 2303-2309, December 2012.
29. J. Ye, B. Bilgin, and A. Emadi, “An extended-speed low-ripple torque control of switched reluctance motor drives,” *IEEE Transactions on Power Electronics*, vol. 30, no. 3, pp. 1457–1470, March 2015.
30. K. M. Rahman and S. E. Schulz, “Design of high-efficiency and high-torque-density switched reluctance motor for vehicle propulsion,” *IEEE Transactions on Industrial Applications*, vol. 38, no. 6, pp. 1500–1507, December 2002.
31. S. Smaka, S.Konjicija, S. Masic, and M. Cosovic, “Multi-objective design optimization of 8/14 switched reluctance motor,” in *Proc. International Electric Machines & Drives Conference*, Chicago, IL, May 2013, pp. 468-475.
32. Z.-L. Gaing , Y.-Y. Hsiah, M.-C. Tsai, M.-F. Hsieh, and M.-H. Tsai, “Hybrid design model for optimal designing of a switched reluctance motor,” in *Proc. International Conference on Electrical Machines and Systems*, Busan, South Korea, October 2013, pp. 505-510.
33. H. Zhang, W. Xu, S. Wang, Y. Huangfu, G. Wang, and J. Zhu, “Optimum design of rotor for high-speed switched reluctance motor using level set method,” *IEEE Transactions on Magnetics*, vol. 50, no. 2, February 2014.
34. C. Ma and L. Qu, “Multiobjective optimization of switched reluctance motors based on design of experiments and particle swarm optimization,” *IEEE Transactions on Energy Conversion*, vol. 30, No. 3, pp. 1144-1153, September 2015.

35. A. M. Omekanda, “A new technique for multidimensional performance optimization of switched reluctance motors for vehicle propulsion,” *IEEE Transactions on Industrial Applications*, vol. 39, no. 3, pp. 672–676, June 2003.

36. D.-H. Kim, J. K. Sykulski, and D. A. Lowther, “Design optimisation of electromagnetic devices using continuum design sensitivity analysis combined with commercial EM software,” *IET Science, Measurement & Technology*, vol. 1, no. 1, pp. 30-36, February 2007.

37. S. H. Heo, M. K. Baek, K. H. Lee, S. G. Hong, and I. H. Park, “Shape and topology optimization of rotor in synchronous reluctance motor using continuum sensitivity and adaptive level set method,” in *Proc. International Conference on Electrical Machines and Systems*(*ICEMS*), Busan, South Korea, Oct. 2013, pp. 129-133.

38. K.-Y. Hwang, S.-B. Rhee, J.-S. Lee, B.-I. Kwon, “Shape optimization of rotor pole in spoke type permanent magnet motor for reducing partial demagnetization effect and cogging torque,” in *Proc. International Conference on Electrical Machines and Systems*, Seoul, Korea, October 2007, pp. 955-960.

39. J. Lee and S. Wang, “Topological shape optimization of permanent magnet in voice coil motor using level set method,” *IEEE Transactions on Magnetics*, vol. 48, no. 2, pp. 931-934, February 2012.

40. Y. Li, S. Ravi, and D. C. Aliprantis, “Tooth shape optimization of switched reluctance motors for improved torque profiles,” in *Proc. IEEE International Electric Machines & Drives Conference* (*IEMDC*), Coeur d'Alene, ID, May 2015, pp. 569-575.

41. M. Li , F. G. Guimarães, and D. A. Lowther, “A multiobjective approach for designing the rotor of brushless motors,” *IEEE Transactions on Magnetics*, vol. 49, no. 5, pp. 2279-2282, May 2013.

42. K. S. Seo, K. H. Lee, and I. H. Park, “Multiple level-set methods for optimal design of nonlinear magnetostatic system,” *IEEE Transactions on Magnetics*, vol. 54, no. 3, March 2018.

43. Y. K. Choi, H. S. Yoon, and C. S. Koh, “Pole-shape optimization of a switched-reluctance motor for torque ripple reduction,” *IEEE Transactions on Magnetics*, vol. 43, no. 4, pp. 1797-1800, April 2007.

44. Y. Li and D. C. Aliprantis, “Optimum stator tooth shapes for torque ripple reduction in switched reluctance motors,” in *Proc. International Electric Machines & Drives Conference*, Chicago, IL, May 2013, pp. 1037-1044.

45. S. I. Nabeta, I. E. Chabu, L. Lebensztajn, D. A. P. Corrêa, W. M. da Silva, and K. Hameyer, “Mitigation of the torque ripple of a switched reluctance motor through a multiobjective optimization,” *IEEE Transactions on Magnetics*, vol. 44, no. 6, pp. 1018-1021, June 2008.

46. Z. Yueying, Y. Chuantian, Y. Yuan, W. Weiyan, and Z. Chengwen, “Design and optimisation of an in-wheel switched reluctance motor for electric vehicles,” *IET Intelligent Transport Systems*, vol. 13, no. 1, pp. 175-182, 2019.

47. H. Zhang and S. Wang, “Topology optimization of rotor pole in switched reluctance motor for minimum torque ripple,” *Electric Power Components and Systems*, vol. 45, no. 8, pp. 905-911, May 2017.

48. J. Lee, J. H. Seo, and N. Kikuchi, "Topology optimization of switched reluctance motors for the desired torque profile," *Structural and Multidisciplinary Optimization*, vol. 42, no. 5, pp 783–796, November 2010.

49. M. H. Bakr, *Nonlinear Optimization in Electrical Engineering with Applications in MATLAB*, Institution of Engineering and Technology, 2013. ISBN: 978-1849195430.

50. Y. Zhang, O. S. Ahmed, and M. H. Bakr, "Adjoint sensitivity analysis of plasmonic structures using the FDTD method," *Optics Letters*, vol. 39, no. 10, pp. 3002-3005, May 2014.

51. M. H. Bakr, O. S. Ahmed, M. H. El Sherif, and T. Nomura, "Time domain adjoint sensitivity analysis of electromagnetic problems with nonlinear media," *Optics Express*, vol. 22, no. 9, pp. 10831-10843, April 2014.

52. S. Abhyankar, V. Rao, and M. Anitescu, "Dynamic security constrained optimal power flow using finite difference sensitivities," in *Proc. IEEE PES General Meeting, Conference and Exposition*, National Harbor, MD, July 2014, pp. 1–5.

53. S.-H. Lee, D.-H. Kim, J.-H. Lee, B.-S. Kim, and I.-H. Park, "Shape design sensitivity for force density distribution of magnetic systems," *IEEE Transactions on Applied Superconductivity*, vol. 12, no. 1, pp. 1471-1474, March 2002.

54. L. S. Kalantari, O. Ahmed, M. H. Bakr, and N. K. Nikolova, "Adjoint sensitivity analysis of 3D problems with anisotropic materials," in *Proc. IEEE MTT-S International Microwave Symposium* (*IMS*), Tampa, FL, June 2014.

55. Y. Zhang, M. H. Negm, and M. H. Bakr, “An adjoint variable method for wideband second-order sensitivity analysis through FDTD,” *IEEE Transactions on Antennas and Propagation*, vol. 64, no. 2, pp. 675-686, February 2016.

56. Y. Zhang and M. H. Bakr, “FDTD-based transient adjoint sensitivity analysis” in *Proc. IEEE MTT-S International Conference on Numerical Electromagnetic and Multiphysics Modeling and Optimization* (*NEMO*), ON, Canada, August 2015.

57. Y. S. Kim and I. H. Park, “Topology optimization of rotor in synchronous reluctance motor using level set method and shape design sensitivity,” *IEEE Transactions on Applied Superconductivity*, vol. 20, no. 3, pp. 1093-1096, June 2010.

58. S. Wang, D. Youn, H. Moon, and J. Kang, “Topology optimization of electromagnetic systems considering magnetization direction,” *IEEE Transactions on Magnetics*, vol. 41, no. 5, pp. 1808-1811, May 2005.

59. D.-H. Kim, I.-H. Park, J.-H. Lee, and C.-E. Kim, “Optimal shape design of iron core to reduce cogging torque of IPM motor,” *IEEE Transactions on Magnetics*, vol. 39, no. 3, pp. 1456-1459, May 2003.

60. E. Kuci, F. Henrotte, P. Duysinx, P. Dular, and C. Geuzaine, “Design sensitivity analysis for shape optimization of nonlinear magnetostatic systems,” *IEEE Transactions on Magnetics*, vol. 52, no. 3, March 2016.

61. D.-H. Kim, K. S. Ship, and J. K. Sykulski, “Applying continuum design sensitivity analysis combined with standard EM software to shape optimization in magnetostatic problems,” *IEEE Transactions on Magnetics*, vol. 40, no. 2, pp. 1156-1159, March 2004.

62. M. H. Bakr, A. Elsherbeni, and V. Demir, *Adjoint Sensitivity Analysis of High Frequency Structures with MATLAB*, Institution of Engineering and Technology, 2017. ISBN: 978-1613532317.

63. J. Dong, K. K. Choi, and N. H. Kim, "Design optimization for structural-acoustic problems using FEA-BEA with adjoint variable method," *Journal of Mechanical Design*, vol. 126, no. 3, pp. 527-533, May 2003.

64. H. Weber, "Time-independent stochastic design sensitivity analysis of structural systems with second-order accuracy," *Journal of Theoretical and Applied Mechanics*, vol. 54, no. 3, pp. 783-794, 2016.

65. R. Lewandowski and M. Łasecka-Plura, "Design sensitivity analysis of structures with viscoelastic dampers," *Elsevier Computers & Structures*, vol. 164, pp. 95-107, February 2016.

66. W. Zhang, Z. Du, G. Sun, and X. Guo, "A level set approach for damage identification of continuum structures based on dynamic responses," *Journal of Sound and Vibration*, vol. 386, pp. 100–115, January 2017.

67. N. Zabihi and R. Gouws, "A review on switched reluctance machines for electric vehicles," in *Proc. IEEE International Symposium on Industrial Electronics (ISIE)*, Santa Clara, CA, November 2016, pp. 799-804.

68. B. Bilgin, A. Emadi, and M. Krishnamurthy, "Comprehensive evaluation of the dynamic performance of a 6/10 SRM for traction application in PHEVs," *IEEE Transactions on Industrial Electronics*, vol. 60, no. 7, pp. 2564-2575, July 2013.

69. R. Vandana and B. G. Fernandes, “Design methodology for high performance segmented rotor switched reluctance motors,” *IEEE Transactions on Energy Conversion*, vol. 30, no. 1, pp. 11-21, March 2015.

70. A. Y. Anekunu, S. P. Chowdhury, and S. Chowdhury, “A review of research and development on switched reluctance motor for electric vehicles,” in *Proc. IEEE Power & Energy Society General Meeting*, Vancouver, BC, Canada, Nov. 2013, pp. 1-5.

71. H. Zhang, W. Xu, S. Wang, Y. Huangfu, G. Wang, and J. Zhu, “Optimum design of rotor for high-speed switched reluctance motor using level set method,” *IEEE Transactions on Magnetics*, vol. 50, no. 2, February 2014.

72. S. J. Salon, *Finite Element Analysis of Electric Machines*, Springer, 1995. ISBN: 9781461523499.

73. B. Bilgin, P. Magne, P. Malysz, Y. Yang, V. Pantelic, M. Preindl, A. Korobkine, W. Jiang, M. Lawford, and A. Emadi, “Making the case for electrified transportation,” *IEEE Transactions on Transportation Electrification*, vol. 1, no. 1, pp. 4–17, June 2015.

74. A. Emadi, *Advanced Electric Drive Vehicles,* CRC Press, 2014. ISBN: 9781138072855.

75. K. Krishnan, *Switched Reluctance Motor drives: Modeling, Simulation, Analysis, Design, and Applications*, CRC Press, 2001. ISBN: 9780849308383.

76. W. Jiang, “Three-Phase 24/16 switched reluctance machine for hybrid electric powertrains: design and optimization (Ph.D. Dissertation),” McMaster University, Hamilton, 2016.

77. P. Chancharoensook and M. F. Rahman, “Dynamic modeling of a four-phase 8/6 switched reluctance motor using current and torque look-up tables”, *IEEE Annual Conference of the Industrial Electronics Society* (*IECON*), Sevilla, Spain, Novomber 2002, pp. 491-496.

78. R. D. Doncker, D. W. J. Pulle, and A. Veltman, *Advanced Electrical Drives: Analysis, Modeling, Control*, Springer, 2011. ISBN: 9789400701816.

79. S. Wang, B. Burton, and R. G. Harley, “Switched reluctance motor measurements and simulation models,” *IEEE Africon Conference in Africa*, Gaborone, Botswana, September 2004, pp. 1161-1167.

80. Š. Mašić, J. Čorda, and S. Smaka, “Computation of static, steady-state and dynamic characteristics of the switched reluctance motor,” *Automatika : journal for control, measurement, electronics, computing and communications*, vol. 43 no. 3-4, pp. 109-117, December 2002.

81. E. Sayed, M. H. Bakr, B. Bilgin, and A. Emadi, “Adjoint-based geometric optimization of nonlinear switched reluctance motors,” *Submitted to Electric Power Components and Systems*.

82. E. Sayed, M. H. Bakr, B. Bilgin, and A. Emadi, “Adjoint sensitivity analysis of switched reluctance motors,” *Electric Power Components and Systems*, vol. 46, no. 18, pp. 1959-1968, Dec. 2018.

83. E. Sayed, M. H. Bakr, B. Bilgin, and A. Emadi, “A MATLAB toolbox for adjoint-based sensitivity analysis of switched reluctance motors,” in *Proc. IEEE Electrical Power and Energy Conference* (*EPEC*), Toronto, Canada, October 2018, pp. 1-4.

84. J. L. Coulomb and G. Meunier, “Finite element implementation of virtual work principle for magnetic or electric force and torque computation,” *IEEE Transactions on Magnetics*, vol. Mag-20, no. 5, pp. 1894-1896, September 1984.

85. J. F. Gieras, Rong-Jie Wang, and M. J. Kamper, *Axial Flux Permanent Magnet Brushless Machines*, Springer, 2005. ISBN: 978-1-4020-8227-6.

86. Y. Zhang, O. S. Ahmed and M. H. Bakr, “Adjoint sensitivity analysis of plasmonic structures using the FDTD method,” *Optics Letters*, vol. 39, no. 10, pp. 3002-3005, May 2014.

87. M. H. Bakr, O. S. Ahmed, M. H. El Sherif, and T. Nomura, “Time domain adjoint sensitivity analysis of electromagnetic problems with nonlinear media,” *Optics Express*, vol. 22, no. 9, pp. 10831-10843, April 2014.

88. L. S. Kalantari, O. Ahmed, M. H. Bakr, and N. K. Nikolova, “Adjoint sensitivity analysis of 3D problems with anisotropic materials,” in *Proc. IEEE MTT-S International Microwave Symposium (IMS)*, Tampa, FL, June 2014.

89. L. S. Kalantari, O. S. Ahmed, M. H. Bakr, and N. K. Nikolova, “A TLM-based wideband adjoint variable method for sensitivity analysis of non-dispersive anisotropic structures,” *IEEE Transactions on Antennas and Propagation*, vol. 65, no. 10, pp. 5267-5277, October 2017.

90. Y. Zhang, O. S. Ahmed and M. H. Bakr, “Adjoint sensitivity analysis of plasmonic structures using the FDTD method,” *Optics Letters*, vol. 39, no. 10, pp. 3002-3005, May 2014.

91. S. Abhyankar, V. Rao, and M. Anitescu, “Dynamic security constrained optimal power flow using finite difference sensitivities,” in *Proc. IEEE PES General Meeting*, *Conf. Expo*., July 2014, pp. 1–5.

92. S.-H. Lee, D.-H. Kim, J.-H. Lee, B.-S. Kim, and I.-H. Park, “Shape design sensitivity for force density distribution of magnetic systems,” *IEEE Transactions on Applied Superconductivity*, vol. 12, no. 1, pp. 1471-1474, March 2002.

93. J. S. Ryu, Y. Yao, C. S. Koh, S. Yun, and D. S. Kim, “Optimal Shape Design of 3-D Nonlinear Electromagnetic Devices Using Parameterized Design Sensitivity Analysis”, *IEEE Transactions on Magnetics*, Vol. 41, No. 5, pp. 1792-1795, 2005.

94. N. Takahashi, T. Yamada, and D. Miyagi, “Examination of Optimal Design of IPM Motor Using ON/OFF Method,” *IEEE Transactions On Magnetics*, Vol. 46, No. 8, pp. 3149-3152, 2010.

95. B. Polajzer, G. Stumberger, D. Dolinar, and K. Hameyer, “Determination of Force and Flux Linkage Characteristics of Radial Active Magnetic Bearings,” *IEEE Region 8 EUROCON*, pp. 1-3, 2003.

96. S. R. H. Hoole, Finite Elements, Electromagnetics and Design, *Elsevier Science*, 1995.

97. J. S. Ryu, Y. Yao, C. S. Koh, S. Yun, and D. S. Kim, “Optimal shape design of 3-D nonlinear electromagnetic devices using parameterized design sensitivity analysis,” *IEEE Transactions on Magnetics*, vol. 41, no. 5, pp. 1792-1795, May 2005.

98. N. Takahashi, T. Yamada, and D. Miyagi, “Examination of optimal design of IPM motor using on/off method,” *IEEE Transactions on Magnetics*, vol. 46, no. 8, pp. 3149-3152, July 2010.

99. I.-H. Park, B.-T. Lee, and S.-Y. Hahn, “Design sensitivity analysis for nonlinear magnetostatic problems using finite element method,” *IEEE Transactions on Magnetics*, vol. 28, no. 2, pp. 1533-1536, March 1992.

100. Y. Li, S. Ravi, and D. C. Aliprantis, “Tooth shape optimization of switched reluctance motors for improved torque profiles,” in *Proc. IEEE International Electric Machines & Drives Conference* (*IEMDC*), Coeur d'Alene, ID, May 2015, pp. 569-575.

101. JMAG-Designer FEA simulation tool, version 15.1, JSOL Corporation, https://www.jmag-international.com.

102. K. Weeber and S. R. H. Hoole, “A structural mapping technique for geometric parametrization in the optimization of magnetic devices,” *International Journal for Numerical Methods in Engineering*, vol. 33, no. 10, pp. 2145-2179, July 1992.

103. K. Weeber and S. R. H. Hoole, “Geometric parametrization and constrained optimization techniques in the design of salient pole synchronous machines,” *IEEE Transactions on Magnetics*, vol. 28, no. 4, pp. 1948-1960, July 1992.

104. Y. Yao, J. S. Ryu, C. S. Koh, and D. Xie, “A novel mesh regeneration using structural deformation analysis for 3-D shape optimization of electromagnetic devices,” *IEEE Transactions on Magnetics*, vol. 40, no. 2, pp. 1009-1012, March 2004.

105. D. L. Logan, A First Course in the Finite Element Method, *Cengage Learning*, 2012. ISBN 9781133169055.

106. R. A.Waltz, J. L. Morales, J. Nocedal, and D. Orban, “An interior algorithm for nonlinear optimization that combines line search and trust region steps,” *Mathematical Programming*, vol. 107, no. 1, pp. 391-408, July 2006.

107. N. Takahashi, T. Yamada, and D. Miyagi, “Examination of optimal design of IPM motor using on/off method,” *IEEE Transactions on Magnetics*, vol. 46, no. 8, pp. 3149-3152, August 2010.

108. Y. Okamoto, K. Akiyama, and N. Takahashi, “3-D topology optimization of single-pole-type head by using design sensitivity analysis,” *IEEE Transactions on Magnetics*, vol. 42, no. 4, pp. 1087-1090, April 2006.